Univerzita Karlova v Praze

Matematicko-fyzikální fakulta

DIPLOMOVÁ PRÁCE

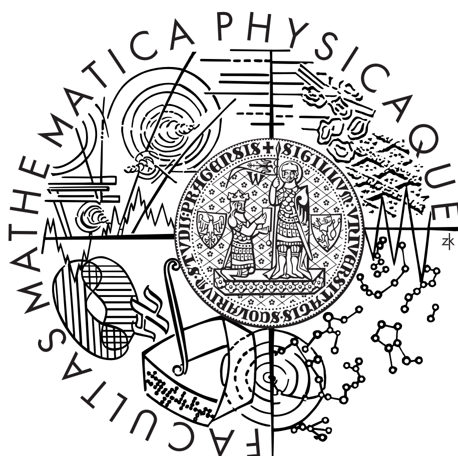

Petr Hruška

Studium tenkých kovových vrstev

Katedra fyziky nízkých teplot

Vedoucí diplomové práce:	doc. Mgr. Jakub Čížek, Ph.D.
Studijní program:	Fyzika
Studijní obor:	Fyzika kondenzovaných soustav a materiálů

Praha 2014

First and foremost I would like to thank my supervisor doc. Mgr. Jakub Čížek, Ph.D. for his kind guidance, priceless advices and for his patience during long discussions about the experimental results. Without his support this work could not have been finished. My gratitude also goes to Dr. Ing. Jiří Bulíř for his guidance during the deposition of magnesium films. Finally many thanks belong to all my colleagues who provided me an assistance in a certain stage of my work: Wolfgang Anwand, Jan Drahokoupil, František Lukáč, Michal Novotný, Jitka Stráská and Marián Vlček.

I declare that I carried out this master thesis independently, and only with the cited sources, literature and other professional sources.

I understand that my work relates to the rights and obligations under the Act No. 121/2000 Coll., the Copyright Act, as amended, in particular the fact that the Charles University in Prague has the right to conclude a license agreement on the use of this work as a school work pursuant to Section 60 paragraph 1 of the Copyright Act.

In Prague April 11, 2014 Petr Hruška

Název práce: Studium defektů v tenkých kovových vrstvách

Autor: Petr Hruška

Katedra: Katedra fyziky nízkých teplot

Vedoucí diplomové práce: doc. Mgr. Jakub Čížek, Ph.D., Katedra fyziky nízkých teplot, Univerzita Karlova v Praze, Matematicko-fyzikální fakulta

Abstrakt: V předkládané práci byly studovány tenké Mg vrstvy připravené pomocí RF magnetronového naprašování. Pozitronová anihilační spektroskopie s laditelnou energií (VEPAS) byla použita při studiu defektů v Mg vrstvách. VEPAS byla doplněna skenovací elektronovou mikroskopií a difrakcí rentgenového záření za účelem určení velikosti zrn, fázového složení a textury. Byl zkoumán vliv různé rychlosti depozice, teploty depozice, žíhání, odlišných substrátů a tloušťky vrstev na množství defektů v Mg vrstvách. Studium defektů pomocí VEPAS ukázalo, že ve zkoumaných Mg vrstvách jsou pozitrony zachytávány v misfit dislokacích a vakanci podobných defektech v okolí hranic zrn a že jejich množství může být sníženo depozicí za zvýšené teploty.

Klíčová slova: Mg vrstvy, magnetronové naprašování, pozitronová anihilační spektroskopie s laditelnou energií, skenovací elektronová mikroskopie, rentgenová difrakce

Title: Investigation of defects in thin metallic films

Author: Petr Hruška

Department: Department of Low-Temperature Physics

Supervisor: doc. Mgr. Jakub Čížek, Ph.D., Department of Low-Temperature Physics, Charles University in Prague, Faculty of Mathematics and Physics

Abstract: In the present work Mg films prepared by RF magnetron sputtering were studied. Variable energy positron annihilation spectroscopy (VEPAS) was employed for investigation of defects in the Mg films. VEPAS characterization was combined with scanning electron microscopy and X-ray diffraction in order to determine grain size, phase composition and texture. The effect of different deposition rate and deposition temperature, annealing, various substrates and film thickness on the structure and amount of defects present in the Mg films was examined. Defect studies by VEPAS showed that positrons in studied Mg films are trapped at misfit dislocations and at vacancy-like defects in grain boundaries and their density can be reduced by the deposition at elevated temperature.

Keywords: Mg films, magnetron sputtering, variable energy positron annihilation spectroscopy, scanning electron microscopy, X-ray diffraction

Contents

Introduction **3**

1 Current knowledge of Mg films **4**
1.1 Hydrogen loading of Mg 4
1.2 Structure of Mg films and lattice defects 5

2 Thin films and magnetron sputtering **6**
2.1 Basic facts about films 6
2.2 Physical sputtering 7
2.3 Magnetron sputter deposition 9
2.3.1 DC sputtering 9
2.3.2 AC sputtering 10
2.3.3 RF sputtering 10
2.3.4 Magnetron sputtering 11

3 Positron annihilation in thin films **13**
3.1 Positron source 13
3.2 Positron beams 15
3.3 Doppler broadening of positron annihilation radiation 16
3.4 Coincidence Doppler Broadening 18
3.5 Shape parameters 19

4 Experimental techniques **23**
4.1 Profilometry 23
4.2 Scanning electron microscopy 24
4.3 X-Ray diffraction 25
4.4 Variable energy positron annihilation spectroscopy 29

5 Results and discussion **31**
5.1 Deposition of Mg films 31
5.2 SEM observations 37
5.2.1 Thin Mg films 40
5.2.2 Thick Mg films 40
5.2.3 Mg films deposited on Mg 44
5.3 XRD results 45
5.3.1 Texture studies 46
5.3.2 Cohen-Wagner analysis 54
5.3.3 Williamson-Hall analysis 56
5.4 VEPAS results 58

5.4.1 S(E) curves and S-W plots 61
5.4.2 Results of VEPFIT analysis 71

Conclusions **76**

Bibliography **78**

List of Tables **83**

List of Abbreviations **84**

Introduction

Magnesium hydride (MgH_2) is an attractive material suitable for on-board hydrogen storage in mobile applications due to its safety and high hydrogen absorption capacity. Unfortunately slow sorption rate in the MgH_2 is the major obstacle for its use in practical applications. Structure refinement down to nanoscale could remarkably speed up the hydrogen sorption kinetics since a high volume fraction of grain boundaries provides a network for easier hydrogen distribution into grains. The effect of microstructure on the hydrogen sorption kinetics can be investigated on thin films since samples with nanocrystalline to epitaxial structure can be relatively easily prepared by varying the deposition conditions. Obviously structure characterization of Mg thin films is necessary as a first step of this investigation.

In his work Mg films prepared by RF magnetron sputtering were studied using variable energy positron annihilation spectroscopy, scanning electron microscopy and X-ray diffraction. Variable energy positron annihilation spectroscopy provides information about defect structure in various depths in the studied material, hence it is a very useful tool for studies of the microstructure of Mg thin films. Scanning electron microscopy and X-ray diffraction provide information about the surface morphology and the crystalline structure respectively.

Chapter 1

Current knowledge of Mg films

1.1 Hydrogen loading of Mg

Hydrogen storage attracts attention of researchers as a renewable and environmentally safe energy source. Light metal hydrides are promising candidates for on-board applications due to the safety and the high absorption capacity [1, 2].

Magnesium is considered to be a promising storage material for its lightweight, low cost and in particular because the magnesium hydride MgH_2 presents a high gravimetric efficiency (7.6 wt.% of hydrogen), a good volumetric efficiency (150 kg H_2/m^3) and forms a relatively weak Mg-H bonds (126 kJ/mol) [1–5]. Moreover magnesium exhibits a metal-to-insulator transition reflecting interesting electrical and optical properties like a reflective metal to a transparent hydride transition. Gasochromic mirrors could be used as hydrogen sensors, smart windows or variable reflection coatings [6, 7].

However the major obstacle for practical application of magnesium is the slow sorption rate. The slow hydrogen absorption and desorption kinetics is caused by the slow diffusion of hydrogen in MgH_2 (so-called "Blocking effect") [2]. Due to the high activation energy ($\sim$ 1 eV) the hydrogen diffusion coefficient in MgH_2 is 10^{-20} m^2 s^{-1} as was reported by Spatz et al. [8]. Furthermore a high operation temperature about 600 K is required to reach a plateau pressure of 1 bar at thermodynamic equilibrium [2, 9]. This especially restricts magnesium use in mobile applications which require operation at moderate temperatures and pressures of few bars.

A lot of effort in the last 15 years was devoted to overcome these barriers. It was suggested that the structure refinement down to nanoscale could remarkably improve the hydrogen sorption kinetics since a high volume fraction of grain boundaries provides a network for easier hydrogen distribution into grains. Besides nanocrystalline bulk magnesium materials prepared by ball milling or equal channel angular pressing nanocrystalline thin magnesium films can be fabricated by magnetron sputtering, pulsed laser deposition or thermal evaporation [3, 4, 7, 9, 10] Moreover samples of a different structure from epitaxial up to nanocrystalline can be relatively easily prepared by varying the deposition conditions. Capping of Mg films by a thin palladium layer reduces the operation temperature since palladium enhances dissociation of hydrogen molecule [9].

It was found by Uchida et al. [5] that the "Blocking effect" can be efficiently bypassed by adjusting the hydrogen loading rate and hydrogen transport takes

place along grain boundaries. The hydrogen desorption temperature decreases rapidly with increasing thickness of Mg layer (< 1 μm) in three layered Pd-Mg-Pd film as was revealed by Higuchi et al. [11]. Ye et al. [12] investigated the structure changes in Mg-Pd multi layer film after thermal activation of the film and subsequent hydrogenation-dehydrogenation cycles. Although the structure changes and Mg-Pd phases are formed the hydrogen storage capacity is unchanged. The dependence of the hydrogen capacity and optical properties of Mg films on the annealing temperature were studied by Qu et al. and Gautam et al. [4, 7] and revealed the optimal annealing temperature of 200°C and 250°C respectively.

Hydrogen sorption properties and the structure of Mg films alloyed with metals (Cu, Nb, Ni, Pd, Si, Ti, V etc.) were investigated as well [13–16].

1.2 Structure of Mg films and lattice defects

Several studies have reported columnar structure of Mg films prepared by magnetron sputtering [9–12, 14].

Variable positron annihilation spectroscopy was employed for characterization of Mg and Mg-based films by two groups: University of Delft group [14–16] and University of Trento group [3, 17, 18].

Doppler broadening provides depth-sensitive information about homogeneity and concentration of defects. Moreover it is capable of monitoring metal-to-insulator transitions during the hydrogenation process. Moreover thanks to the large difference in positron affinity of Mg and Ti a formation of Mg-Ti phase can be monitored [14–16].

Positron lifetime spectroscopy showed a presence of open volume defects in the Mg and Mg-based films, namely vacancies, di-vacancies and even vacancy clusters. Vacancy-based defects play an important role in the hydrogen mobility and sorption capacity since they facilitate diffusion similarly to grain boundaries. It has been reported that the concentration of vacancy clusters is decreased by an increasing number of hydrogen (deuterium) sorption-desorption cycles without restoring the original capacity [3]. However later studies revealed the vacancy clusters assemble at grain boundaries and assist a restoring of Mg from MgH_2, while the concentration of intragranular vacancies decreases by the number of hydrogenation cycles [17, 18].

Chapter 2

Thin films and magnetron sputtering

2.1 Basic facts about films

The concept of a thin film is not strictly defined. The film thickness usually falls into the range from 10 nm to 10 μm, however in general the main feature of thin films consists in their physical properties which differ considerably from a bulk material, although their composition and structure are the same. This difference is caused by the different role the material surface plays. The fraction of surface atoms in a thin film is not negligible unlike the bulk, hence surface effects modifies or completely change some properties of a film.

An advantage of thin films is that by varying the deposition conditions (deposition method, working gas, pressure, temperature, deposition rate, target quality and composition etc.) we can relatively easily prepare samples of different properties or with different type of doping. Thin films can be divided according to their structure into four groups:

1. Amorphous films with lack of any long range order.
2. Nanocrystalline films which are characterized by the mean grain size below 100 nm.
3. Polycrystalline films which have larger grains with a typical size in the range from ~ 0.1 to 10 μm.
4. Epitaxial films which are formed by a single crystalline layer.

In principle the thin film deposition includes a target material evaporation, transport of the evaporated material to a substrate and a film growth on the substrate. The material can be evaporated thermally (vacuum evaporation), physically (magnetron sputtering) or it can be ablated by a laser (pulsed laser deposition). The whole process of deposition must generally take place in a vacuum chamber. A good vacuum is required to attain a good film purity and to fulfill the necessary deposition conditions. The most of deposition techniques requires a high vacuum (from 10^{-3} to 10^{-7} Pa) or an ultra-high vacuum (less than 10^{-7} Pa) [19], some techniques after reaching a proper vacuum level uses a working gas (pressure in order of few Pa).

In the laboratory at the Department of Analysis of Functional Materials, Institute of Physics, Academy of Sciences of the Czech Republic, where the Mg films studied in this work were prepared, there are four basic deposition methods: magnetron sputtering, pulsed laser deposition, electron beam evaporation and ion beam assisted deposition. In the following text a brief description of the magnetron sputtering is given. Informations about other deposition techniques, thin films growth and properties are provided in many literature, e.g. [19–22].

2.2 Physical sputtering

The physical sputtering is the process when surface atoms are physically (not thermally) vaporized by momentum transfer from bombarding particles, usually energetic ions accelerated in an electric field (see section 2.3). Sputtered particles can be then deposited onto a substrate to create a thin film. This is called sputter deposition or just simply sputtering.

To describe the sputtering effectivity we define the sputtering yield as a number of sputtered atoms per one incident particle. It depends on the target material, the size and the direction of the momentum of a bombarding particle, the crystal orientation and the surface quality of a target, but it is not affected by the target temperature. More detailed description of the effects of sputtering and differences of sputtering from the thermal evaporation are included in [19].

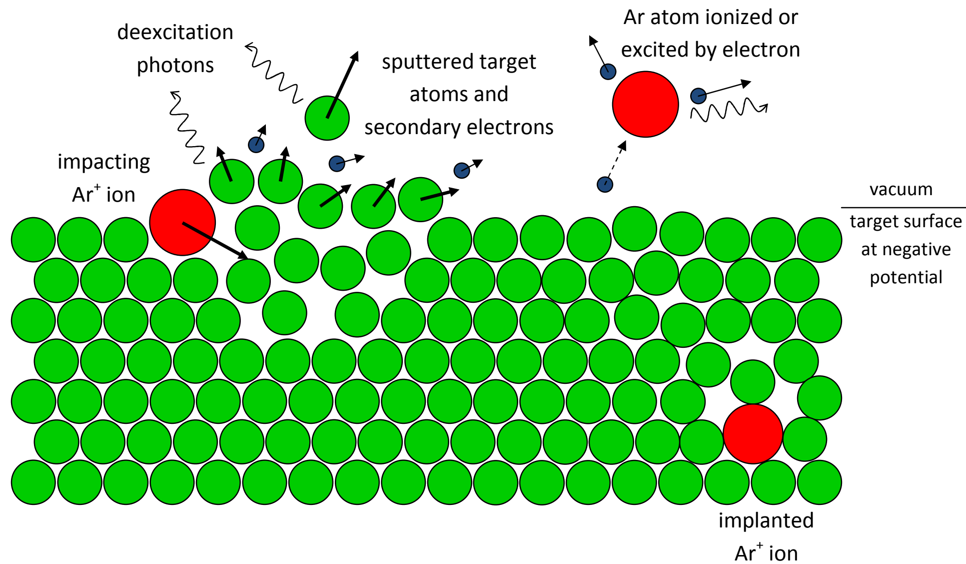

Figure 2.1: Simplified scheme of physical sputtering. Energetic argon ions can either kick out target atoms and secondary electrons or be implanted into near-surface region introducing lattice defects in a target. Particles in plasma cloud above a target can be ionized or excited by collisions with energetic particles. Deexcitation photons are characteristic for working gas (argon) and target atoms respectively.

Scheme in fig. 2.1 shows some of the effects that may occur during the bombarding of a target surface by energetic ions. The particle of a working gas (here argon) is ionized, accelerated in an electric field and directed to a target surface

which is at a negative potential. The incident ion penetrates to the surface, creates a collision cascade and transfer a part of its momentum to the target atoms which allows them to escape from the surface. However the most of the ion energy ($\sim 95\%$) is transformed to heat (hence a target has to be actively cooled). A part of the bombarding ions can be neutralized and reflected from the surface or implanted into a near-surface region introducing lattice defects. Ionized sputtered atoms are driven by electric field back to the target and contribute to sputtering as well.

Between the target and the substrate serving as electrodes is ignited a plasma discharge. The plasma "cloud" above the target contains predominantly ionized working gas and sputtered target atoms, secondary electrons ejected from the target and neutral working gas and sputtered atoms, see fig. 2.1. The spectrum of plasma radiation is determined by electron transitions in electron shells of working gas and sputtered atoms. Hence the radiation is characteristic for used target material and the working gas. Fig. 2.2 shows a photo of the plasma in a magnetron sputtering chamber with palladium target bombarded by argon ions. While positive ions bombard the target at a negative potential, neutral sputtered atoms of rather high momentum move towards the substrate holder on a ground level, "fall" onto the substrate and create a thin film.

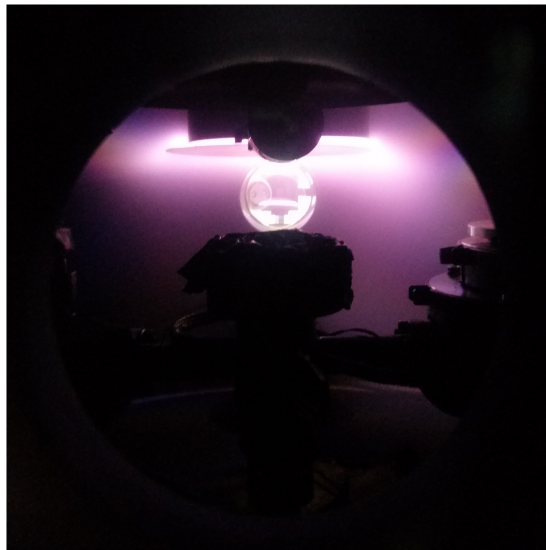

Figure 2.2: Photo a of plasma cloud created in a magnetron sputtering chamber during a deposition of a palladium. Argon was used as the working gas. The substrate was closed by a shutter during a pre-sputtering process to prevent a deposition of impurities adsorbed on the target surface.

In the first approximation we can consider the interaction of an energetic ion with a surface atom as a collision of two hard spheres. The transferred energy is highest for very close masses of the bombarding particle and the target atom. However since the cost, the safety and the chemical properties must be considered in choosing of a suitable working gas, inert gases (neon, argon, krypton) are most widely used. A mixture of inert (e.g. argon) and a reactive gas (e.g. oxygen) is used for a reactive magnetron sputtering [1].

[1] The reactive magnetron sputtering is a very popular method of deposition of e.g. oxides.

The sputtering yields of various materials can be calculated from the first principles using Monte Carlo simulations for various working gases, ion energies and angles of incidence (defined with respect to the surface normal). Fig. 2.3 shows an energy and angular dependence of sputtering yield for magnesium in argon [23]. One can see in fig. 2.3 that the sputtering yield increases with the angle to maximum value (70°for Mg-Ar combination) and then rapidly decreases as the bombarding particles are reflected from the surface. Another common feature is the presence of the threshold energy, i.e. the lowest energy of incident particle which causes sputtering.

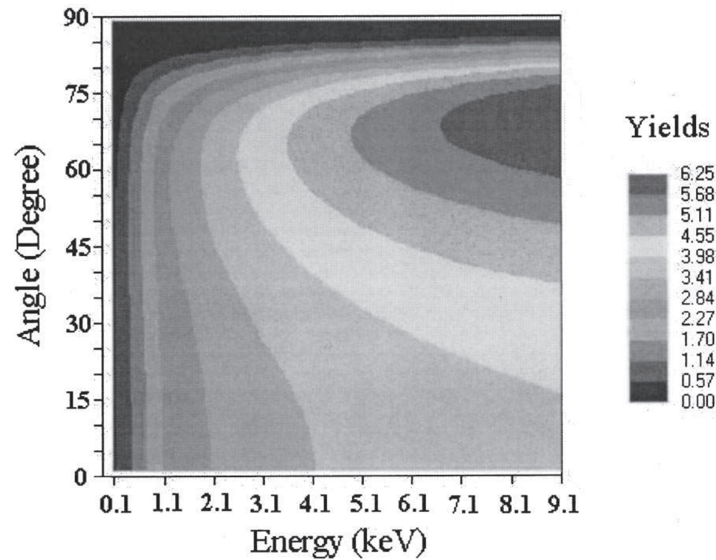

Figure 2.3: Energy and angular dependence of sputtering yield for Mg in Ar calculated by Bordes et al. [23]

2.3 Magnetron sputter deposition

To establish a plasma discharge [19, 20] in a vacuum chamber, equilibrium conditions must be fulfilled. The discharge must be self-sustainable, i.e. enough secondary electrons must be ejected from cathode to ionize enough working gas atoms, which bombard the cathode surface producing secondary electrons etc. Essential conditions for a plasma discharge ignition are described by so-called Paschen curves, the dependence of the breakdown voltage on the pressure (multiplied by the electrode distance) in a vacuum chamber, see fig 2.4.

2.3.1 DC sputtering

In a DC (direct current) discharge configuration the sputtering target serves as a cathode while the substrate is placed on an anode at the ground potential. Thus positive ions bombard the target and cause a physical sputtering. Secondary

The inert gas (argon) serves as a sputtering medium, while the reactive component (oxygen) chemically react with sputtered atoms and create an oxide.

electrons ejected from the cathode and negative ions, which can be present in the plasma cloud formed during a reactive sputtering, may bombard the substrate with the growing film as well. To prevent re-sputtering of the film, substrates can be placed in an off-axis position, however for an appropriate gas pressure the effect of re-sputtering is overweighted by the film growth. In a DC sputtering the sputtering target must be an electrical conductor since an insulating surface (insulating target or a non-conductive surface layer) develops a surface charge, which prevent ion bombardment.

2.3.2 AC sputtering

In an AC (alternating current) low frequency discharge configuration the target potential is periodically reversed. As the counterelectrode is used the substrate or chamber walls. For frequencies of tens kHz the ion mobility is high enough to form a DC-like discharge alternately on each electrode. In asymmetrical AC sputtering back-sputtering of the growing film occurs making it more uniform and enhancing its quality.

2.3.3 RF sputtering

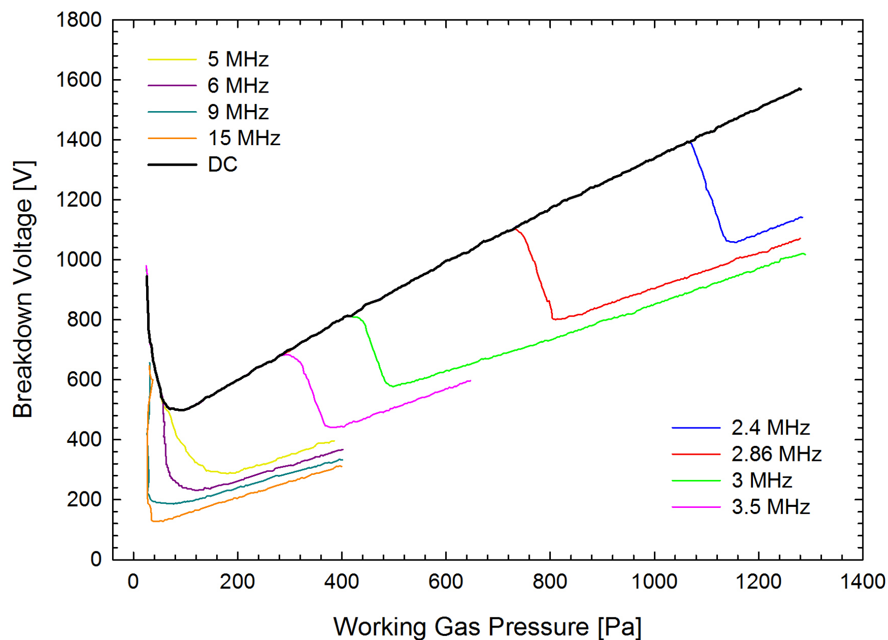

Figure 2.4: Paschen curves in argon for a fixed electrode distance by Venugopalan [24,25]. The black curve responds to a DC voltage, colored curves respond to various RF frequencies.

For an RF (radio frequency) sputtering high frequencies in the range 0.5 - 30 MHz are used. The frequency of 13,6 MHz used commonly in commercial devices was used for deposition of Mg films which are studied in this work. Fig. 2.4 shows the argon Paschen curves for various RF frequencies. One can see that the higher is the frequency the lower must be the pressure for the minimal breakdown voltage.

At RF frequencies the mobility of ions is too low, they are not able to follow potential changes anymore. Since the electron mobility is still high enough, they are able to ionize working gas to sustain a discharge. Moreover the target and chamber walls (serving as a counterelectrode) are alternately negatively charged. Since the area of chamber walls is higher than the target area, larger negative charge density is on the target and a negative DC bias appears on it. Thus positive ions are attracted by and bombard the target and cause sputtering of the target material. A great advantage of RF sputtering is that the target surface can be an electric insulator, since a creation of DC bias does not depend on the electric properties of the target.

2.3.4 Magnetron sputtering

In a sputtering configuration using only an electric field (DC, AC or RF), the secondary electrons are accelerated away from the cathode and ionize working gas atoms quite inefficiently. Introducing a magnetic field as shown in fig. 2.5a the path of the electrons becomes curved by the Lorentz force and the secondary electrons circulate in the vicinity of the target.

Due to the high flux of electrons near the target surface a plasma of higher density can be created making the sputtering more effective. Thus the magnetron sputtering enables a formation of a dense plasma in the near-target area at pressures lower than those needed for the discharge ignition. At lower pressures the mean free path of an energetic ion is large enough to reach the target without energy loss due to collisions and the sputtering rate is higher.

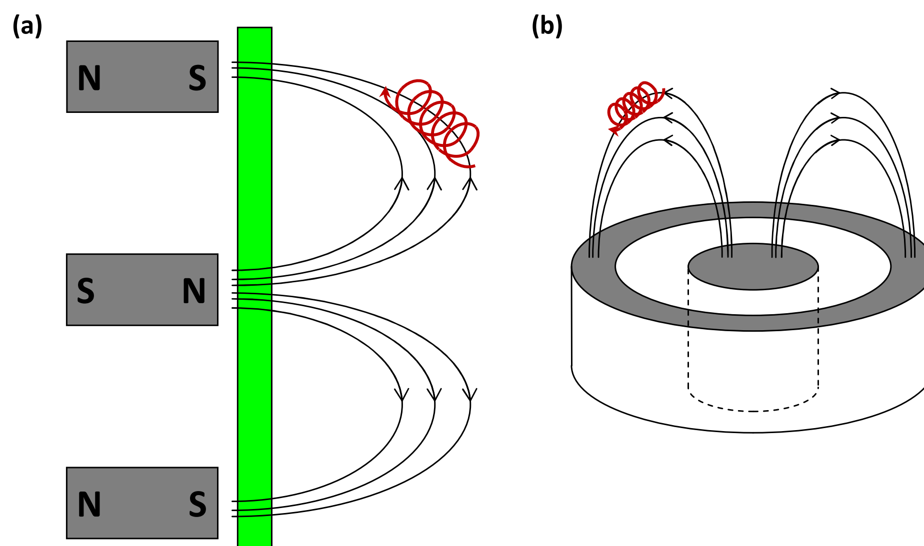

Figure 2.5: (a) Schematic picture of the magnetic field curving the electron path and keeping it in the vicinity of cathode. (b) Geometry of circular planar magnetron. The central part and the outer ring are permanent neodymium magnets with opposite magnetic orientation.

There exist several magnetron configurations (see e.g. [19, 20]). Mg films studied in this work were deposited using circular planar magnetron geometry, illustrated in fig. 2.5b. Magnetic field is created by permanent neodymium

magnets, the central magnet and outer magnetic ring have opposite magnetic orientation. The magnets are backed by a metal plate to shield back magnetic field.

One can see in fig. 2.6 the erosive zone created in an area of highest plasma density, where the sputtering is most effective. The presence of the erosive zone shows that a plasma is not uniform, however this fact does not affect a film uniformity since the substrates are substantially smaller than a target.

Figure 2.6: (a) Mg target used for deposition of Mg films studied in this work. (b) Al target with a very clearly visible erosive zone. Both targets are 100 mm wide in diameter

Chapter 3

Positron annihilation in thin films

Positron annihilation spectroscopy (PAS) is a unique and non-destructive method for investigation of defects and free volumes of the size below the resolution of other experimental techniques. High energy positron implanted into a material rapidly (within a few ps) loses its kinetic energy, thermalizes and diffuses in a material until it annihilates. The fraction of positrons annihilated-in-flight, i.e. during the slowing-down process is usually negligible (less than 1 %) [26]. The thermalized positron experiences an electric potential generated by ion cores and electrons with strong a repulsion close to the ion cores. Thus a defect site with missing atom or atoms (e.g. vacancy, vacancy cluster, dislocation) provides a potential well for positrons.. As a consequence positrons are attracted by this kind of defects and annihilate there in a localized state. Annihilation photons carry information about defect structure of a material. Positron lifetime spectroscopy (LT) enables to identify defects in the material and to determine defect densities [27]. Doppler broadening of annihilation radiation (DB) provides information about the local chemical environment of defects [28].

3.1 Positron source

Two most common positron sources for PAS are based on a pair production and a radioactive decay. The first technique uses high energy electrons in an accelerator. These electrons emit Bremsstrahlung photons when are decelerated in matter or their trajectory is curved. For photon energy higher than twice the electron rest energy ($E_\gamma > 2m_0c^2$) the pair of electron and positron can be produced by interaction of photon in the matter. An advantage of this positron source is that it can be used for pulsed positron beam for depth-resolved positron lifetime measurement.

Radioactive β^+ sources are cheaper and more available.. One of the most common positron sources [1] is ^{22}Na radioisotope which decays with half-life of 2.6 years to ^{22}Ne isotope with simultaneous emission of positron and electron neutrino. Subsequent de-excitation of ^{22}Ne nucleus is realized by emission of a gamma ray with energy of 1274 keV called starting photon. Thanks to a very short lifetime of ^{22}Ne excited state ($t_{1/2}$ = 3.7 ps) the starting photon carries

[1] Radioisotope ^{22}Na is usually the best choice as a positron source thanks to the high positron yield (0.9 positrons per decay) and half-life ($T_{1/2}$ = 2.6 years). Another advantage of ^{22}Na is almost simultaneous emission of 1274 keV photon.

information about the time of positron emission and is used as a start signal in positron lifetime spectroscopy. The decay scheme of ^{22}Na is shown in fig. 3.1.

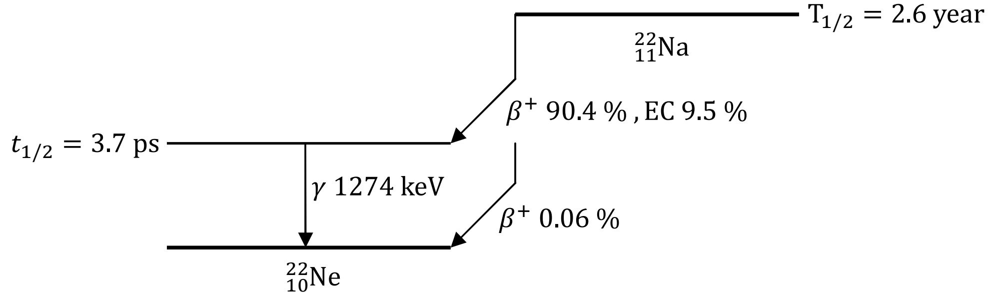

Figure 3.1: The decay scheme of ^{22}Na radioisotope with half-life $T_{1/2} = 2.6$ years.

The energy spectrum of β^+ decay is typically continuous with a characteristic end point energy of hundreds of keV. In fig. 3.2 there is the energy spectrum of ^{22}Na with end point energy of 545 keV. Positron implanted into a material loses rapidly its kinetic energy and reaches thermal equilibrium with energy $\frac{3}{2}k_BT$ (39 meV). This process so-called thermalization is caused at high energies (over 100 eV) by ionization and elastic scattering on nuclei, at lower energies (0.1 to 100 eV) by excitation of core and conductive electrons and at the lowest, epithermal energies (below 0.1 eV), by scattering on phonons. The process of thermalization typically takes only few ps and is in two orders shorter than typical lifetimes of positrons in materials.

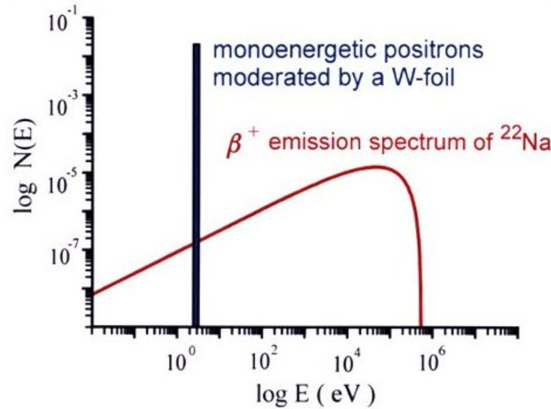

Figure 3.2: The energy spectrum of positrons emitted by ^{22}Na with end point energy 545 keV and mean positron energy 270 keV.

The probability that a positron implanted into material penetrates into depth z is described by the empirical implantation profile.

$$P(z) = \alpha_+ e^{-\alpha_+ z} \tag{3.1}$$

The mean penetration depth $1/\alpha_+$ can be calculated from the empirical formula

$$\frac{1}{\alpha_+}[\text{cm}] = \frac{E_{max}^{1.4}[\text{MeV}]}{16\varrho[\text{g cm}^{-3}]}, \tag{3.2}$$

where E_{max} is the end point energy of β^+ spectrum and ϱ is the density of material. Typical mean penetration depths are $\sim 10 - 100$ μm (e.g. 150 μm for Mg). In thermal equilibrium positron is elastically scattered by phonons and makes an isotropic random diffusion motion. Positron diffusion length L_+ is a mean distance which positron travels by diffusion motion during its lifetime τ_B.

$$L_+ = \sqrt{D_+ \tau_B} \tag{3.3}$$

At the room temperature the positron diffusion coefficient D_+ in solids typically falls into range 0.1 to 2 cm^{2}s^{-1} and the positron diffusion length is $100 - 200$ nm.

Thus the most of positrons emitted by β^+ source annihilate deep in material (in depth $\sim 10 - 100$ μm) and produce annihilation photons carrying information independent on the surface of the sample. In this setup positron annihilation is widely used method to characterize defect structure in bulk materials, but it is insensitive to the surface and therefore not suitable for study of thin films typically of thicknesses < 1 μm.

3.2 Positron beams

The idea of a monoenergetic positron beam exists since 1950 however sufficient intensities for practical applications were achieved after 1980 with advent of high-efficiency moderators [29]. In the last 15 years variable energy positron annihilation spectroscopy (VEPAS) became very popular technique for study of thin films and defect depth profiles.

To produce a monoenergetic positron beam from a broad energy spectrum (see fig. 3.2) positrons are moderated using a very thin ($1-2$ μm) annealed crystalline tungsten foil. The most of the positrons (fast positrons, fraction ~ 0.87) gets through the foil with almost unchanged energy of several keV, a part of the positrons (fraction ~ 0.13) annihilate in the foil and a part of the positrons (fraction $\sim 10^{-4}$) so-called slow positrons leaves the foil with energy of few eV, given by thermal energy $k_B T$ and positron work function (-3 eV for W). Slow positrons are thermalized in the foil, diffuse to the surface and because of the negative positron work function of tungsten they are emitted into the vacuum, where they have lower energy.

The efficiency ϵ of a moderator ($\sim 10^{-4}$ for tungsten foil) depends on [29] the probability density function $P_{therm}(z)$ that a positron becomes thermalized in a depth z; the probability density function $P_{diff}(z)$ that the thermalized positrons diffuse to the surface from a depth z; and the probability density function $P_{em}(z)$ that the positrons are emitted after reaching the surface. Integration of the product of these three probability density functions over all values of z we obtain ϵ which can be approximated by expression

$$\epsilon \approx \frac{1.7 P_{em} \varrho [\text{g cm}^{-3}] L_+ [\text{cm}]}{E_{max}^{1.14} [\text{MeV}]}, \tag{3.4}$$

where ϱ is the density of the foil, L_+ is the diffusion length defined by eq. (3.3) and E_{max} is the end-point energy of β^+ source. From inspection of eq. (3.4) we obtain requirements for a good moderator: large diffusion length, i.e. low

concentration of defects, high density and high probability of positron emission, i.e. high absolute value of a negative work function and a clean perfect surface.

After moderation positrons are guided by magnetic field of solenoidal or Helmholtz coils (magnetic induction is parallel to the positron flow). To prevent fast positrons from reaching the sample, the positron beam can be bend in the magnetic field or one can select slow positrons by suitable combination of electric and magnetic field, so-called E×B filter. The separated slow positrons (energy of a few eV) are subsequently accelerated by electric field to the energies $0 - 35$ keV.

The positron implantation profile for monoenergetic positron beam is the probability density function $P(z, E)$ that a positron penetrating the material with energy E is thermalized in the interval of depth z. $P(z, E)$ can be for incident positron energies $0-35$ keV estimated by means of Monte-Carlo simulations [29–31]. The implantation profile for homogeneous semi-infinite sample is usually approximated by the Makhovian distribution

$$P(z, E) = \frac{m z^{m-1}}{z_0^m} \exp\left[-\left(\frac{z}{z_0}\right)^m\right], \tag{3.5}$$

where m is a shape parameter, in the first approximation $m \approx 2$ and can be supposed to be material and energy independent. For $m = 2$ the Makhovian distribution (3.5) turns into the first derivative of the Gaussian distribution. The parameter z_0 is a function of energy and the mean implantation depth $\bar{z}$:

$$z_0 = \frac{\bar{z}}{\Gamma\left(1 + \frac{1}{m}\right)}. \tag{3.6}$$

Γ is the gamma function and $\bar{z}$ is the positron penetration depth which obeys the power law:

$$\bar{z} = \frac{A}{\varrho[\text{g cm}^{-3}]} E^n[\text{keV}], \tag{3.7}$$

where ϱ is the sample density, n and A are empirical parameters: $n = 1.6$ and $A = 4.0 \times 10^{-6}\text{g cm}^{-2}\text{keV}^{-n}$.

Fig. 3.3 shows the positron implantation profiles into Mg for various energies. The mean implantation depth as well as the full width at half maximum (fwhm) of the implantation profile increases with increasing incident positron energy. Thus by varying the energy we obtain signal from various depths, but the width of the implantation profile and, thereby, also the depth uncertainty increases with higher energies. Monoenergetic positron beams can provide the information about the defect structure at various depths from the surface, therefore VEPAS is an excellent method for characterization of thin films.

3.3 Doppler broadening of positron annihilation radiation

Annihilating pair of electron and positron can decay into n photons in general. The creation of $n = 2$ annihilation photons is the dominant process (over 99% of all annihilation events). The creation of $n > 2$ photons is a rare event since for

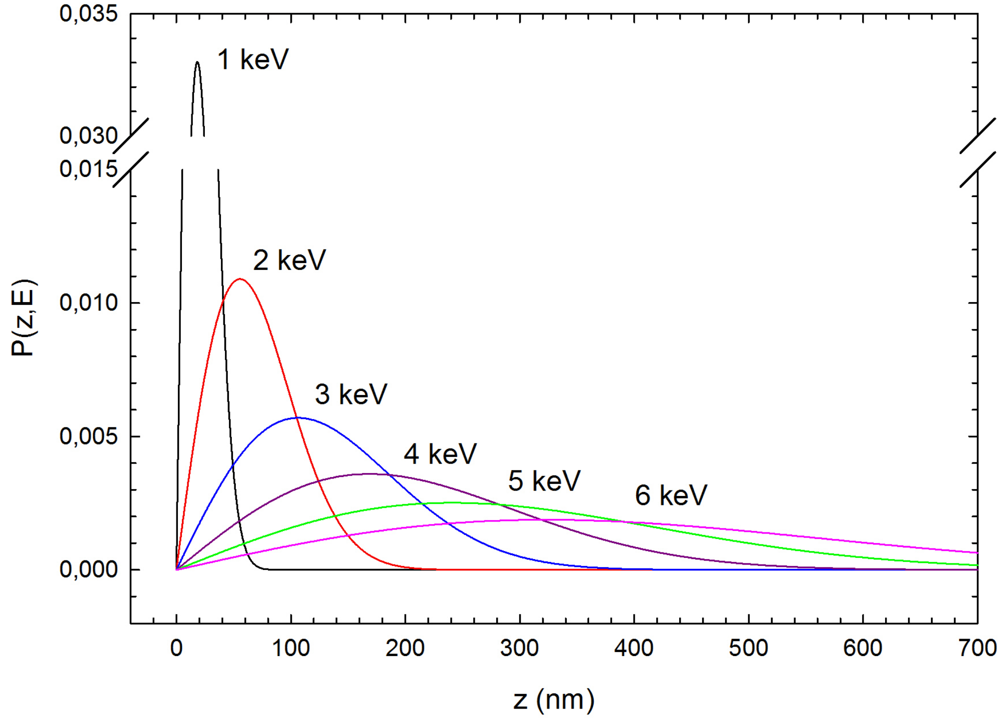

Figure 3.3: Positron implantation profiles $P(z, E)$ in Mg (density 1.738 g cm^{-3}) for various energies.

any additional photon the probability for such decay channel is lowered by the fine-structure constant α [2] increasing positron energies. The creation of $n = 1$ photons is forbidden by momentum conservation law and it is thus possible only by an interaction with an atomic core absorbing the recoil energy (probability depends on the atomic number of a material and is $\sim \alpha^4$).

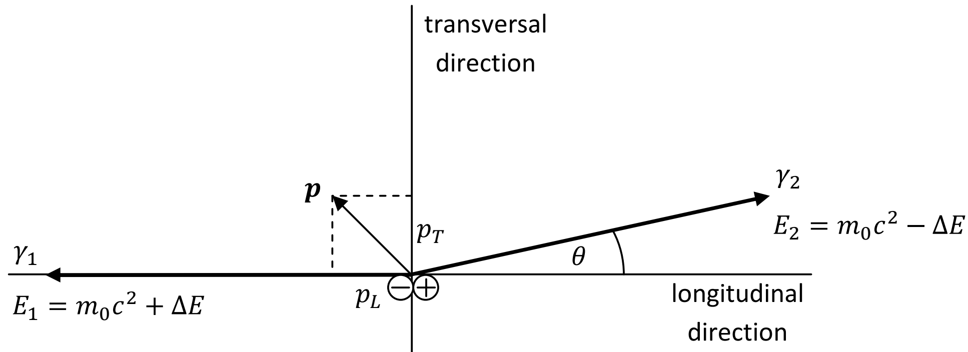

Figure 3.4: Diagram of the energy and the momentum conservation law during the annihilation process in the laboratory frame.

The total momentum of an annihilating electron-positron pair is determined only by the electron momentum since the momentum of thermalized positron is negligible. The non-zero momentum of the pair in the laboratory frame leads to the Doppler shift ΔE and the deviation θ from anticolinearity of the annihilation photons, see fig. 3.4. From the momentum conservation law in the longitudinal

[2]In SI units fine-structure constant is defined by a relation $\alpha = \frac{e^2}{4\pi\varepsilon_0\hbar c} = \frac{1}{137}$.

(p_L) and transversal direction (p_T) respectively we obtain for the Doppler shift and the deviation from anticolinearity:

$$\Delta E = \frac{1}{2} p_L c, \tag{3.8}$$

$$\theta = \frac{p_T}{m_0 c}. \tag{3.9}$$

The Doppler shift causes a broadening of the annihilation peak located at the energy 511 keV (the rest electron energy m_0c^2). One can see in fig. 3.5 the difference between the width of the ^{137}Cs peak given only by the resolution function of the spectrometer and the Doppler broadened of annihilation peak (of course containing also broadening caused by the resolution function) [3].

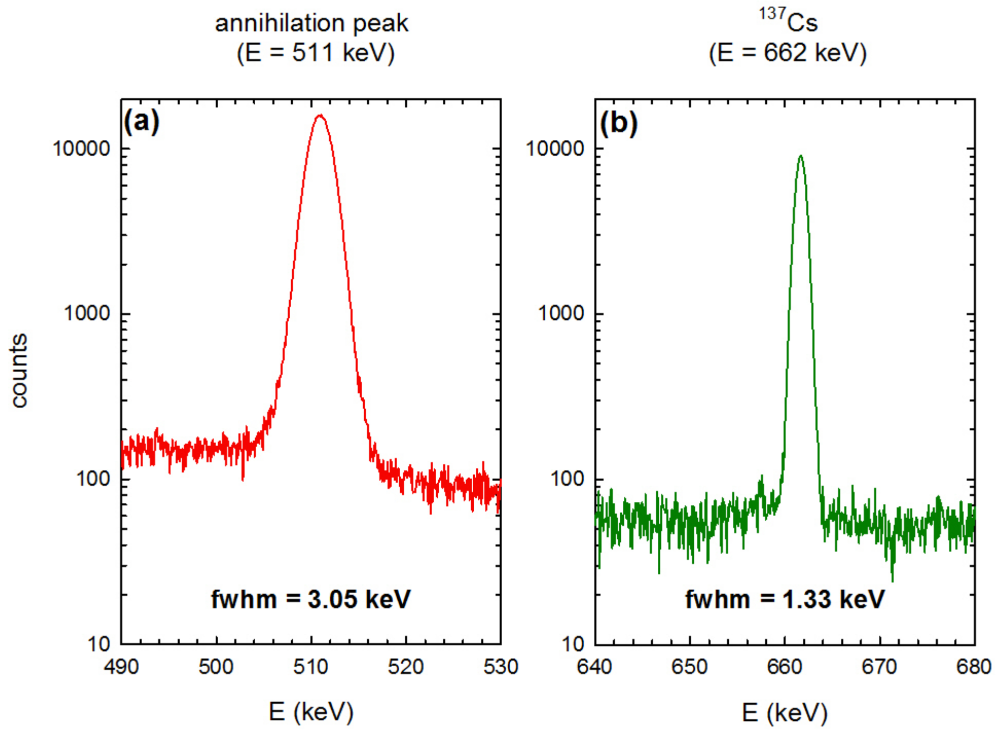

Figure 3.5: (a) the Doppler broadened annihilation peak (511 keV) with fwhm = 3.05 keV; (b) the ^{137}Cs peak (662 keV) with fwhm = 1.33 keV.

3.4 Coincidence Doppler Broadening

By measuring the Doppler shift ΔE we obtain the momentum distribution of electrons which annihilated with positrons given by eq. (3.8). Since each chemical element (or material in general) has a unique electron structure, Doppler broadening (DB) is a convenient method for investigation of the chemical environment of defects, where free positrons are trapped and annihilate. The central part of the annihilation peak is given by low-momentum valence and conductive electrons,

[3] Note that the resolution function is energy dependent, but for relatively close energies of the annihilation and the ^{137}Cs peak, it can be considered to be the same

while tails of the peak corresponds to the contribution of the high-momentum core electrons.

In coincidence Doppler broadening measurement (CDB) the energies of both antiparallel annihilation photons are measured by two detectors. Only the coincidence annihilation events, when a photon was registered simultaneously in both detectors, are recorded. This experimental setup leads to a strong suppression of background (signal to background ratio increases typically from 10^2 to 10^5) and thus enables to resolve a weak contribution of the annihilations with the high-momentum core electrons. The obtained information is carried out by the whole CDB curve, see fig. 3.6a, and can be considered as a signature of each chemical element. CDB data are usually expressed by CDB ratio curves, which highlight the changes in the high momentum range and are constructed by dividing the spectrum of a measured material by a spectrum of well defined reference sample, see fig 3.6b. In general the momentum distribution for a studied sample can be expressed as a superposition of the reference momentum distributions. From the knowledge of this superposition we obtain information about the local chemical environment of the sites, where positrons annihilate.

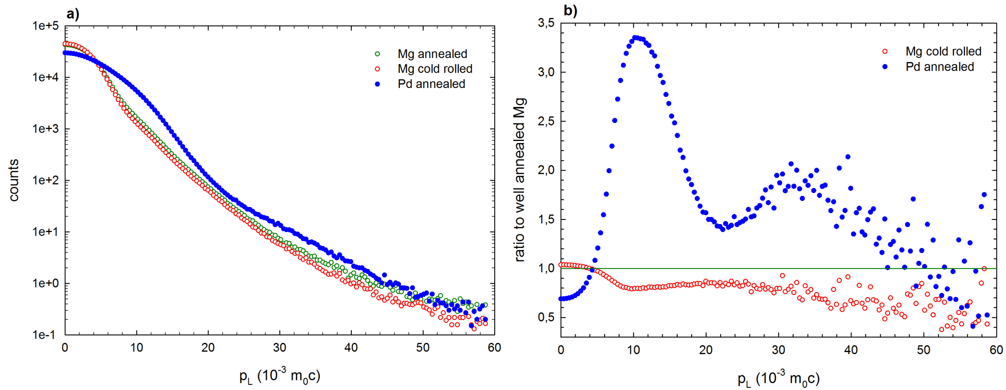

Figure 3.6: (a) CDB spectrum of a well annealed Mg (most of the positrons annihilate in the free state), a cold rolled Mg (most of positrons annihilate in the trapped state in defects) and an annealed Pd. (b) CDB ratio curves of the same samples related to the well annealed Mg. For the annealed Mg the CDB ratio curve is just a straight line at unity.

3.5 Shape parameters

Although CDB provides more information, a non-coincidence single detector DB measurement takes less time ($\sim$ 1 hour) than the measurement in coincidence (which typically takes $\sim$ 2 days) and is therefore more suitable for measurement with monoenergetic positron beams.

To describe the contribution from the conductive and the core electrons to the momentum distribution, S and W shape parameters are employed. The definition of these integral parameters is schematically illustrated in fig. 3.7. The S parameter is defined as the relative area of the central part of the peak and the W parameter is defined as the relative area of the peak wings. The absolute values of both parameters practically don't have a physical relevance, since they

depend on the choice of integration limits, meaningful are only their relative changes. Thus the S and W parameter are usually normalized to a reference value for a defect-free material. Then the information included in the normalized S and W parameter does not depend on different experimental arrangements.

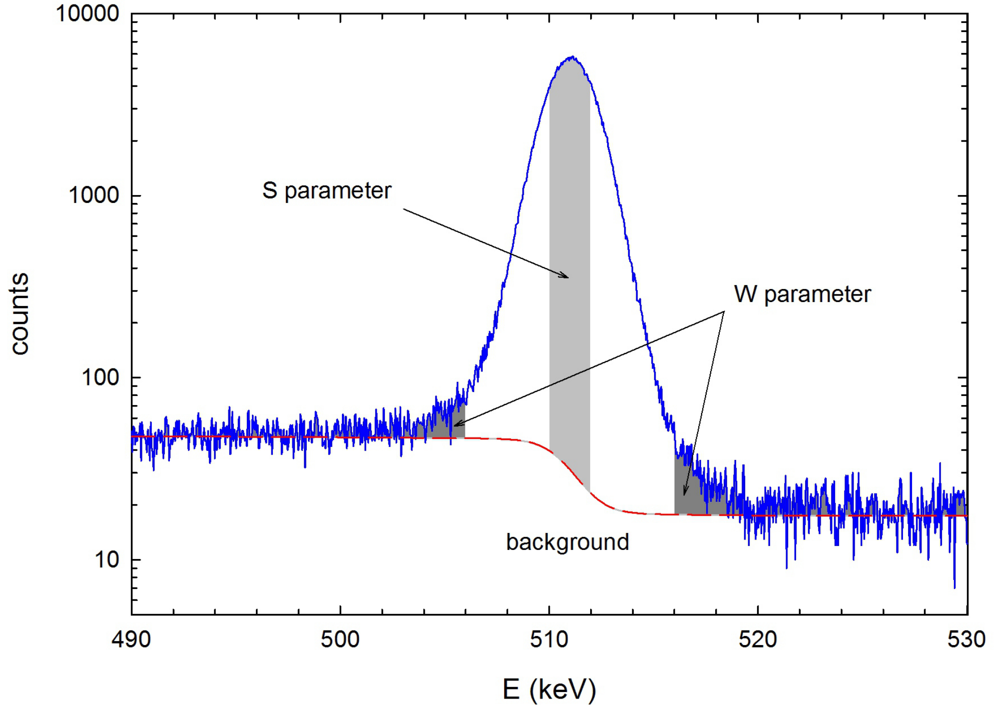

Figure 3.7: Schematic definition of S and W parameter. The background is higher in front of the peak than behind the peak due to incomplete charge collection events.

The relationship of the S and W parameter to the Doppler broadening is quite simple. The S parameter reflects the annihilations with conductive and valence electrons, whereas the W parameter describes the contribution of positrons annihilated by the core electrons. If a positron annihilates in the trapped state in an open volume defect, the probability of annihilation with a high-momentum core electrons decrease. Thus with increasing concentration of defects S increases and W decreases. Both parameters show opposite behaviour and carry out similar information, however the S parameter is more precise due to better signal-to-background ratio in the central area.

Moreover both parameters are additive, that can be expressed by equations:

$$S = \eta_B S_B + \sum_i \eta_{D_i} S_{D_i}, \tag{3.10}$$

$$W = \eta_B W_B + \sum_i \eta_{D_i} W_{D_i}, \tag{3.11}$$

where the index B denotes annihilation in the free state, the index D_i stands for annihilation in the i-type of defect, η_B and η_{D_i} is a fraction of positrons annihilating in the free state and trapped in the i-type defect respectively. Note that for low energies of a few keV positrons annihilate predominantly in the surface state. S_B and S_{D_i} (similarly W_B and W_{D_i}) are the S parameters for

a defect-free material and the i-type of defect [4] respectively. As a consequence of eqs. (3.10), (3.11) for a material containing only 2 positron states (e.g. positrons annihilate either in the free state or trapped in a vacancy) the dependence of W on corresponding S (so-called S-W plot) is linear and defined only by S and W parameters of the corresponding positron states.

The energy dependence of the S parameter so-called $S(E)$ curve provides information about the defect depth profile in a studied material. This can be illustrated by a simple example. The $S(E)$ curves for a well annealed bulk Mg sample (with very low concentration of defects) with and without a thin native oxide layer on the surface and the $S(E)$ curve of a not annealed bulk Mg (with higher concentration of defects than annealed samples) are shown in fig. 3.8. From inspection of fig. 3.8 it is clear that the bulk S parameter is higher for the not annealed Mg than for the defect-free sample due to higher concentration of defects. The positron diffusion length L_+ given by the slope of the $S(E)$ curve and is lower for the not annealed sample. Enhancement at energies around 3 keV is caused by annihilation in an oxide layer.

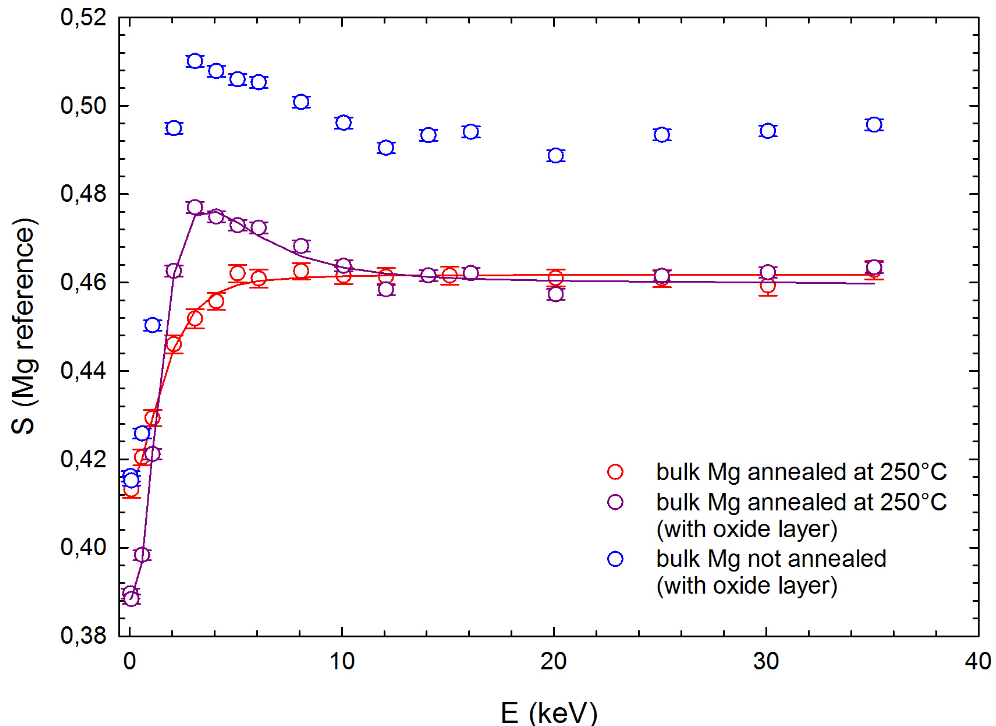

Figure 3.8: $S(E)$ curves for a well annealed bulk Mg (with and without a thin native oxide layer on its surface) and for a not annealed bulk Mg (with oxide layer). The S parameter in eq. (3.10) is determined by the annihilation in the surface state, free state, trapped state in a defect and in an oxide layer.

A quantitative analysis of obtained S curves provides us with values of the positron diffusion lengths and the S parameters. In case of only one type of defects

[4] More correctly S_{D_i} describes S parameter of a material with concentration of defects so high that it causes saturation trapping in the i-type defect (all positrons are trapped and annihilate in there).

present in the material, the concentration of defects c_D can be estimated as:

$$c_D = \frac{1}{\nu_D \tau_B} \left(\frac{L_{+,B}^2}{L_+^2} - 1 \right), \tag{3.12}$$

where ν_D is the specific trapping rate for defects present in the sample, τ_B is the positron lifetime in a defect-free material, $L_{+,B}$ and L_+ is the positron diffusion length in a defect-free material and in the studied sample respectively.

Chapter 4

Experimental techniques

4.1 Profilometry

Profilometry measurement provides an information about the surface profile and quantify its roughness. Contact profilometer uses a diamond stylus moving laterally across the sample for a specified path and measure stylus vertical displacements. In this work KLA Tencor contact profilometer was used. Contact force 0.5 mg was applied in each measurement.

Two most common parameters characterizing roughness are arithmetic average R_a and root mean square R_q defined by:

$$R_a = \frac{1}{n}\sum_{i=1}^{n}|y_i| \tag{4.1}$$

$$R_q = \sqrt{\frac{1}{n}\sum_{i=1}^{n}y_i^2} \tag{4.2}$$

where y_i are vertical deviations from the mean surface line. An example of the surface morphology obtained by profilometry is plotted in fig 4.1. Naturally there are many other possible roughness parameters: e.g. maximal and minimal height or parameters similar to those used for statistical characterization of measured data.

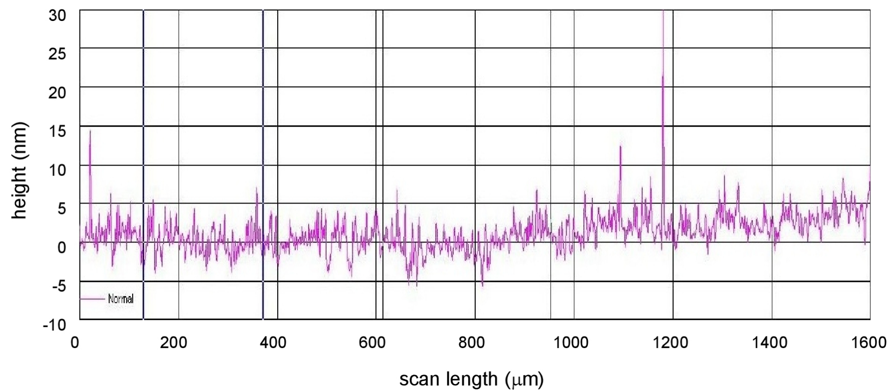

Figure 4.1: Profilometer record of a thick (∼ 1.1μm) Mg film deposited at room temperature. The film roughness was determined from this record.

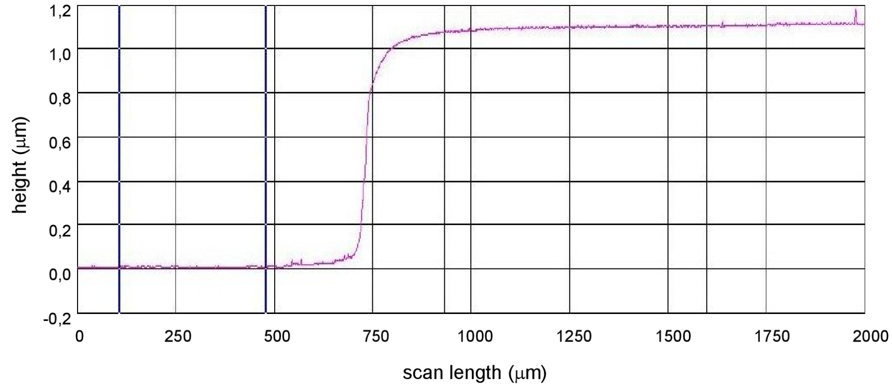

Figure 4.2: Profilometer record of a thick ($\sim 1.1\mu$m) Mg film deposited at room temperature (right) and an uncovered substrate (left). The film thickness was determined from this record.

Profilometry can be used as a direct method for determination of the film thickness, as illustrated in fig. 4.2. A part of a substrate was covered during a deposition. Thus the film thickness is the difference between the mean height in the film region and the mean surface height.

4.2 Scanning electron microscopy

Scanning electron microscopy (SEM) provides a high resolution imaging of surfaces using an electron beam as a probe. The electrons are emitted by a tungsten filament or a LaB_6 crystal and substantially accelerated in an electric field to energies up to 50 keV. The electron beam guided by magnetic lenses scans in a raster pattern over a specimen surface while the emitted electrons and radiation are being detected.

Fig. 4.3 shows a schematic interaction diagram of the electron beam and the specimen surface depicting regions, from which different types of signal come [32–35]. A part of high energy electrons penetrating the material interacts by elastic collisions with specimen atoms and escape the material with relatively high energy (50 eV up to several keV depending on the primary beam energy). These electrons are called back-scattered electrons (BSE). The second part of the electrons loses its energy by inelastic collisions ionizing specimen atoms. The emitted electrons of energies less than 50 eV and are called secondary electrons (SE). "Holes" in electron shells left by secondary electrons are "filled" with electrons from outer shells and the released energy is carried out by Auger electron (dominates for atoms with low atomic number) or by characteristic radiation (dominates for atoms with high atomic number).

The elastic cross section increases with atomic number, thus the number of BSE is higher for heavier elements. SEM micrographs taken using the BSE signal exhibit a so-called Z-contrast, i.e. the regions containing atoms with higher atomic number appears brighter (produce more signal) than regions containing atoms with lower Z number.. Hence Z-contrast provides a composition resolution. However BSE are able to provide a topological contrast as well, since their straight trajectories (because of their high energy) are influenced by topological irregularities.

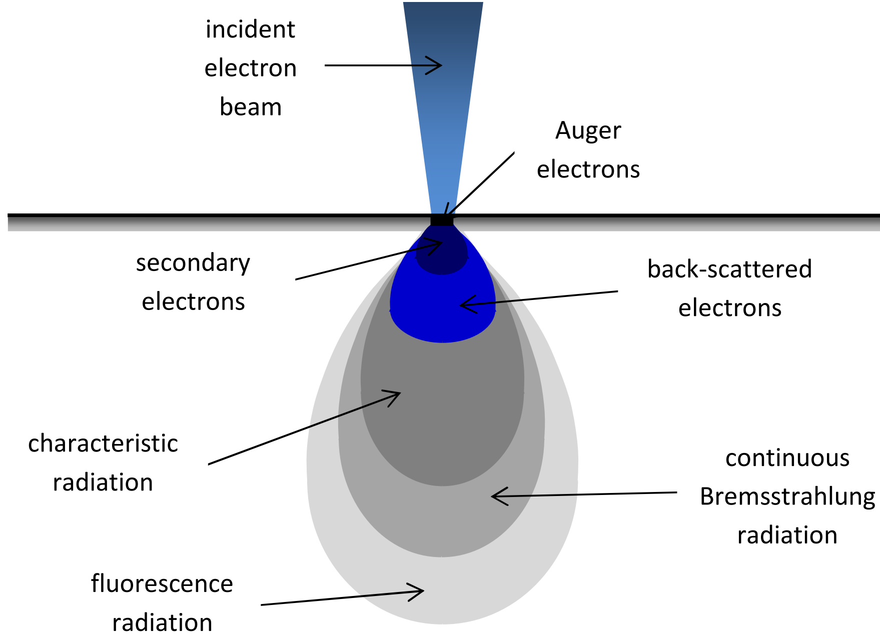

Figure 4.3: Interaction of electron beam with specimen atoms. Each signal has its own characteristic depth from which it is coming.

The number of secondary electrons emitted from the near-surface region is sensitive to the specimen surface morphology. The SE signal provides a so-called topological contrast, i.e. the regions where more electrons reach and escape from the surface appear brighter. Since the information carried by SE comes from a smaller area (see fig. 4.3), the spatial resolution of SE is higher compared to that provided by BSE.

Most of SEM observations were performed on a FEI Quanta 200 SEM (Department of Physics of Materials, Faculty of Mathematics and Physics, Charles University). Some of SEM micrographs were measured by a FEI Phenom microscope (Institute of Physics, Academy of Sciences of the Czech Republic).

4.3 X-Ray diffraction

X-Ray diffraction (XRD) is a powerful tool capable to determine crystal structure (lattice parameters, texture, stresses) and phase composition. Monochromatic X-Ray radiation with wavelength in units of angströms is used as a probe.

Assuming the kinematic and the Fraunhofer approximation [36] the primary plane wave is elastically scattered from a single atom. The secondary spherical wave $E(\mathbf{R})$ is described by:

$$E(\vec{R}) = \tilde{A}\frac{e^{iKR}}{R}\int_V \rho_{at}(\vec{r}) \exp\left[-i(\vec{k}_s - \vec{k}_0)\cdot\vec{r}\right] \mathrm{d}^3\vec{r}, \tag{4.3}$$

where $\tilde{A}$ is a constant, $\rho_{at}(\vec{r})$ is the electron density of a scattering atom and the difference of the wave vector of the scattered and the primary wave $\vec{q} \equiv \vec{k}_s - \vec{k}_0$ is called the scattering vector. Replacing the atomic electron density $\rho_{at}(\vec{r})$ by the crystal electron density $\rho_{cryst}(\vec{r})$, eq. (4.3) will describe a wave diffracted by the whole crystal.

Thanks to the periodicity of the crystal lattice, the crystal electron density can be expressed as:

$$\rho_{cryst}(\vec{r}) = \sum_{\vec{R}\in E^3} \Omega(\vec{R})\rho_{cell}(\vec{r}-\vec{R}), \tag{4.4}$$

where $\vec{R}$ is the lattice vector [1], Ω is the shape function of the crystal (unity in the crystal, zero outside of it) and ρ_{cell} is the electron density in the elementary cell. Using the mathematical identity

$$\sum_{\vec{R}\in E^3} \delta^{(3)}(\vec{r}-\vec{R}) = \frac{1}{V_c}\sum_{\vec{G}\in E^{3*}} \exp\left(i\vec{G}\cdot\vec{r}\right), \tag{4.5}$$

where $\vec{R}$ is a direct lattice vector, $\vec{g}$ is a reciprocal lattice vector [2] and V_c is the unit cell volume, eq. (4.3) turns into the product of two factors:

$$E(\vec{q}) = \frac{A}{V_c}F(\vec{q})G(\vec{q}). \tag{4.6}$$

The function $F(\vec{q})$ in eq. (4.6) is so-called structure factor or form-factor and is representing a Fourier transform of the electron density ρ_{cell} and does not depend on the crystal shape and size. For N atoms in the elementary cell with positions $\vec{r}_i$ and atomic scattering factors $f(\vec{q})$, the structure factor is:

$$F(\vec{q}) = \sum_{i=1}^{N} f(\vec{q})\exp\left[-2\pi i\vec{r}_i\cdot\vec{q}_i\right]. \tag{4.7}$$

The function $G(\vec{q})$ is so-called geometrical factor and depends only on the crystal shape and size and is determined by the crystal shape function:

$$G(\vec{q}) = \sum_{\vec{G}\in E^{3*}} \Omega^{FT}(\vec{q}-\vec{G}). \tag{4.8}$$

From eq. (4.8) the Bragg diffraction condition can be derived. Maximum intensity of the diffracted wave occurs for:

$$\vec{q} = \vec{G}_{hkl}. \tag{4.9}$$

Assuming that the wavelength λ of the diffracted wave is unchanged (elastic scattering) and from $|\vec{G}_{hkl}| = 2\pi/d_{hkl}$ we obtain the Bragg condition in its classical well-known form:

$$2d_{hkl}\sin\theta = \lambda, \tag{4.10}$$

where d_{hkl} is an inter planar distance of a (hkl) plane and θ is an angle between primary wave and (hkl) plane. The broadening of a diffraction peak is given by the geometrical factor, especially by the Fourier transform of the shape function,

[1] Every lattice vector can be expressed as a superposition $\vec{R} = m\vec{a}_1 + n\vec{a}_2 + p\vec{a}_3$, where $\vec{a}_1$, $\vec{a}_2$, $\vec{a}_3$ are the basis vectors and m, n, p are integers.

[2] The reciprocal lattice vector $\vec{G}_{hkl}$ can be expressed as a superposition $\vec{G}_{hkl} = h\vec{b}_1 + k\vec{b}_2 + l\vec{b}_3$, where the reciprocal basis vectors are expressed as $\vec{b}_1 = 2\pi\frac{\vec{a}_2\times\vec{a}_3}{V_c}$ etc. and h, k, l are integers.

i.e. fwhm responds to the mean crystallite size. The peak is apparently broadened by the resolution function and a residual stress as well.

There are 2 geometries schematically shown in fig 4.4, that are mostly used for diffraction studies of thin films and polycrystals. In Bragg-Brentano symmetric geometry (fig. 4.4a) the XRD signal comes from those crystallites whose planes are parallel to the surface. This geometry is suitable for rough texture estimation. Asymmetric grazing incidence or parallel beam geometry (fig. 4.4) provides information about residual films stress, since XRD signal comes from crystallites whose planes have proper orientation with respect to the surface and primary wave respectively.

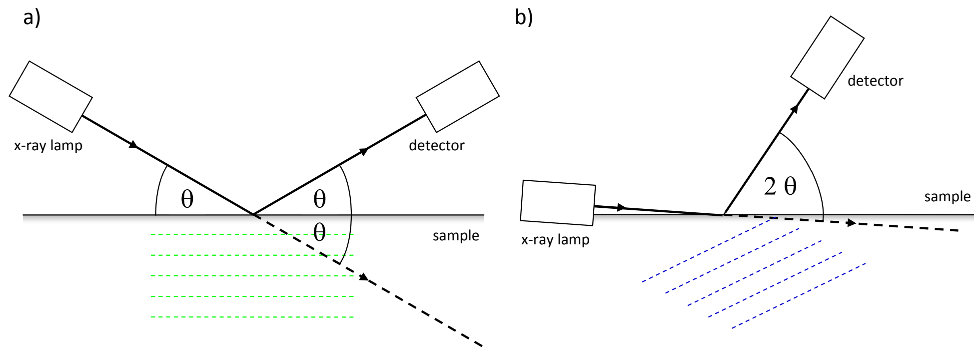

Figure 4.4: XRD geometries mostly used for thin films characterization. (a) In the Bragg-Brentano symmetric geometry the angle between the surface and the X-ray beam and the surface and the detector respectively is θ. The sample is fixed, while the lamp and the detector rotate ($\theta - 2\theta$ setup) or the lamp is fixed, while the detector and the sample rotate ($\theta - \theta$ setup). (b) In the asymmetric grazing incidence (parallel beam) geometry the angle between the lamp and a surface is fixed (typically to the value of 2°) and the detector rotates. For both geometries the angle between the lamp and the detector (i.e. the angle between the primary and the secondary wave) is always 2θ.

Since in Bragg-Brentano symmetric geometry different planes parallel to the surface fulfill Bragg diffraction condition (eq. (4.10)) we are able to determine lattice parameters from measuring the peak positions and calculating the inter planar distances d_{hkl}. However the accuracy of this calculated lattice parameters c_{hkl} could be influenced by a systematic error caused by misalignment of the sample. Reflections at lower diffraction angles θ are influenced by this error more than peaks at high diffraction angles. The error introduced by misalignment can be removed by the $\cos\theta \cot\theta$ extrapolation, which corrects the error from the excentric position of the sample in the focusing circle. Accurate lattice parameter c_0 can be obtained from linear regression of the so-called Cohen-Wagner plot:

$$c_{hkl} = c_0 + s \cos\theta \cot\theta, \tag{4.11}$$

where s a constant factor characterizing the systematic instrumental error.

A diffraction profile can be broadened by instrumental broadening caused by a diffractometer and by physical factors, namely the finite size of crystallites and structure imperfections of the measured sample. The instrumental broadening is given by the resolution function of a diffractometer. Although it can be simulated,

it is more simple and efficient to find it experimentally through the measurement on standards, i.e. high quality stress free crystals (e.g. LaB_6 or CaF_2) which exhibit very narrow diffraction peaks close to the delta-function. Thus one can suppose that the diffraction profiles of such standards are broadened by instrumental resolution function only. The real diffraction profile is then a convolution of the instrumental resolution function and a physically broadened profile.

The physical broadening is given by two factors. Microstrains are introduced into the material due to the presence of defects, i.e. deviations from the ideal crystal lattice, and represent therefore a measure of defect density in studied material. As was discussed before the shape and width of the diffraction profile for an ideal crystallite is given by the geometrical factor Ω, see eq. (4.8), which depends only on the crystallite shape and size.

Values of the mean crystallite size and of the microstrain can be obtained from linear regression of so-called Williamson-Hall plot:

$$\frac{2\pi\cos\theta}{\lambda}\beta = \frac{1}{D} + \eta\frac{4\pi\sin\theta}{\lambda}, \tag{4.12}$$

where β is fwhm of the diffraction profile in radians [3], D is the mean crystallite size and η is dimensionless microstrain [37].

The XRD measurements were performed on a PANalytical X'Pert Pro diffractometer with X'Celarator detector. The X-ray lamp uses a cobalt cathode with $K_{\bar{\alpha}}$ wavelength of 0.179026 nm (weight average) [38].

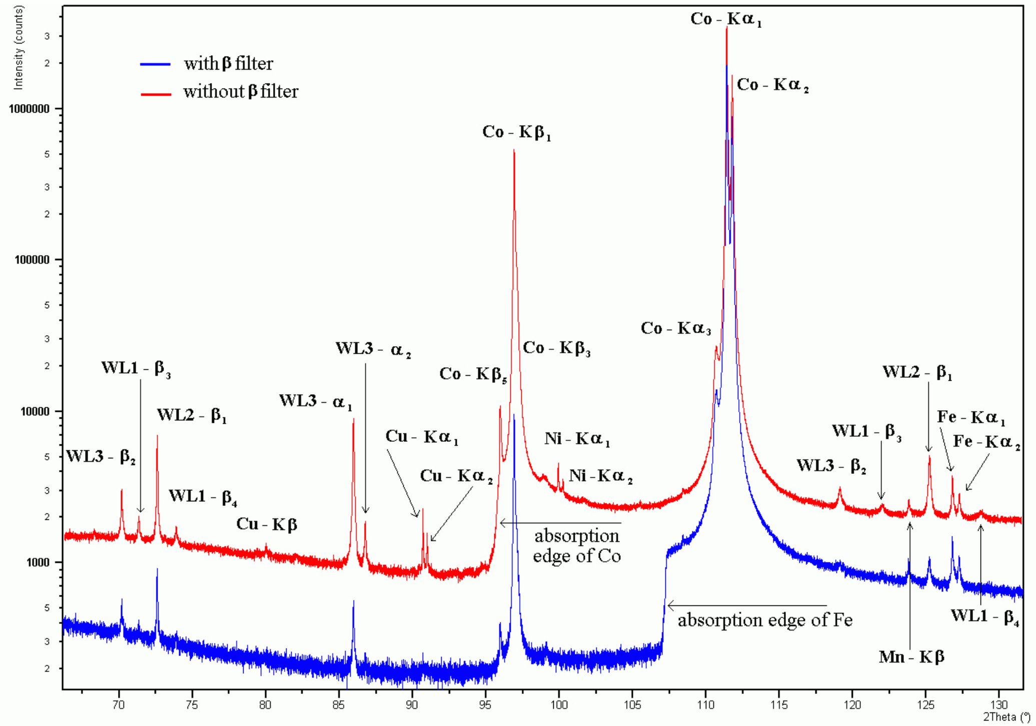

Figure 4.5: X-Ray spectrum of a Co lamp with and without Fe β filter measured using the sapphire (0012) diffraction by Drahokoupil [39].

In tab. 4.1 are shown wavelengths of Co characteristic radiation and their relative intensities. In order to suppress the Co K_β line an iron absorber was

[3] We assume 2θ as x values and intensity as y-values.

employed. A tungsten fiber was used as an electron source. X-Ray spectrum of Co lamp with and without Fe β filter is plotted in fig. 4.5. A contribution of W characteristic radiation to the spectrum is apparent as well.

Co line	λ [nm]	rel. int.
K_{α_1}	0.1788965(7)	1.00
K_{α_2}	0.1792850(7)	0.50
K_β	0.162079(8)	0.15

Table 4.1: X-ray wavelengths of Co according to Bearden [38].

4.4 Variable energy positron annihilation spectroscopy

Variable energy positron annihilation spectroscopy (VEPAS) measurements were performed using magnetically guided variable energy positron beam "SPONSOR" (**S**low **PO**sitro**N** **S**ystem **O**f **R**ossendorf) at the Institute of Radiation Physics, Helmholtz-Zentrum Dresden-Rossendorf (HZDR). The design and construction of the beam is described in the works [40, 41] by Anwand et al. Positron energies can be variated from 27 eV (value at switch-off voltage) to 35 keV. Energy spectra of annihilation gamma rays are measured by a HPGe detector having a relative efficiency of $\sim 30\%$ and an energy resolution of 1.06(1) keV (fwhm at 511 keV).

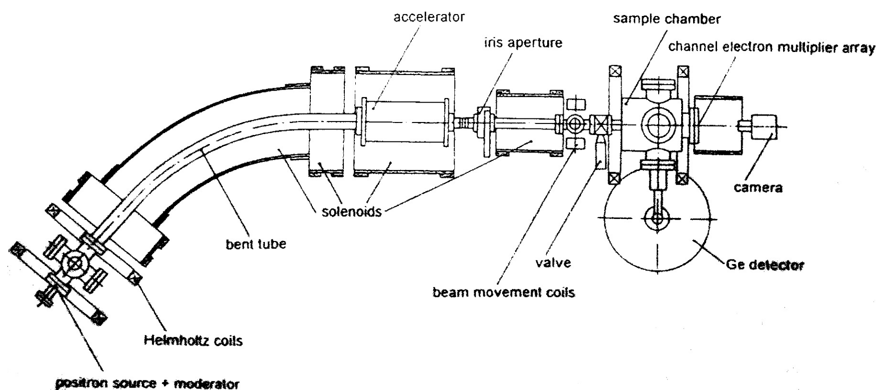

Figure 4.6: View of the SPONSOR beamline and the magnetic coil arrangement.

The single Doppler broadening profiles were evaluated using the S and W shape parameters described in section 3.5. The dependence of the S parameter on the positron energy was analyzed using the VEPFIT code [42]. The parameters of the fitted $S(E)$-curves are sample density and thickness, the positron diffusion length and the bulk S parameter of each layer and the substrate as well.

Figure 4.7: A picture of the laboratory in HZDR and the slow positron beam SPONSOR.

Chapter 5

Results and discussion

A part of the results below were presented in the 13th International Workshop on Slow Positron Beam Techniques and Applications, SLOPOS 13, in Munich. The paper was sent to editors and is accepted for publication in the Journal of Physics: Conference Series (JPCS), IOP Publishing.

5.1 Deposition of Mg films

Mg films studied in this work were deposited at the Department of Analysis of Functional Materials, Institute of Physics, Academy of Sciences of the Czech Republic. The deposition chamber shown in fig. 5.1 carries 4 magnetron targets and thus enables deposition of multi-layered films. Moreover the chamber is equipped by a spectroscopic ellipsometer enabling in-situ monitoring of the film growth. The Mg target (fig. 2.6a) of ACI Alloys, Inc. is 6 mm thick and 100 mm in diameter. The target to substrate distance was fixed at 90 mm. The Mg target composition is shown in tab. 5.1.

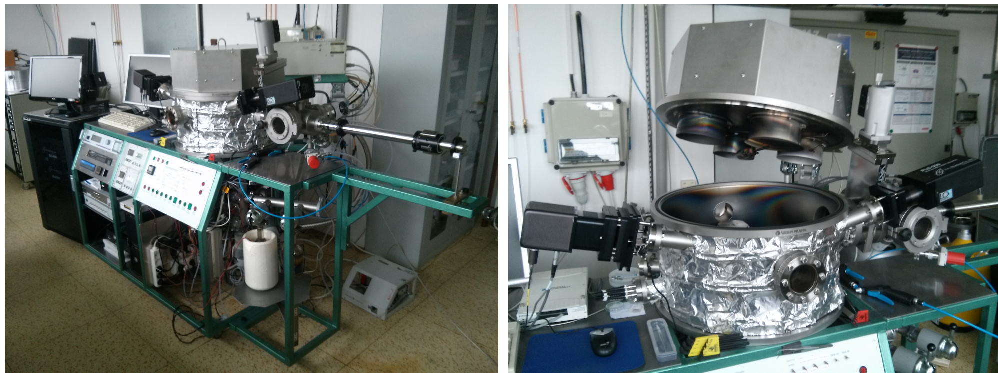

Figure 5.1: The deposition chamber in the Department of Analysis of Functional Materials, Institute of Physics, Academy of Sciences of the Czech Republic.

A set of 8 Mg films was prepared by RF magnetron sputtering using the commercial RF frequency of 13.6 MHz. Before every deposition the chamber evacuated to the high-vacuum $p_0 \sim 10^{-4}$ Pa (measured by Penning gauge). The deposition was performed in an Ar atmosphere at working gas pressure set to $p_{\mathrm{dep}} = 3$ Pa (measured by a capacitance gauge), Ar flow was adjusted to 25 sccm (standard cubic centimeters per minute). The deposition conditions are included

Element		Fraction	Element		Fraction
Magnesium	Mg	99.95 %	Copper	Cu	0.0010 %
Aluminum	Al	0.0037 %	Silicon	Si	0.001 %
Zinc	Zn	0.001 %	Lead	Pb	<0.0002 %
Manganese	Mn	0.0029 %	Calcium	Ca	0.001 %
Iron	Fe	0.0032 %	Tin	Sn	<0.001 %
Nickel	Ni	0.0006 %	Cadmium	Cd	<0.0001 %

Table 5.1: Composition of the Mg magnetron target.

in tab. 5.2. Some of the samples were deposited on a substrate heated at temperature T_{dep} or deposited at room temperature (RT) and subsequently annealed in the chamber at temperature T_{ann}. During the annealing the temperature increased linearly from RT to 300°C within 2.5 min. Then the temperature was kept at 300°C for 1 hour and finally the temperature decreased exponentially to RT within $\sim$ 70 min.

sample	p_0	RF Power	DC bias	T_{dep}	T_{ann}
Mg1	9.7×10^{-5} Pa	200 W	272 V	RT	–
Mg2	1.5×10^{-4} Pa	200 W	250 V	300°C	–
Mg3	1.7×10^{-4} Pa	200 W	250 V	RT	–
Mg4	2.0×10^{-4} Pa	200 W	244 V	RT	300°C (1 hr)
Mg5	2.9×10^{-4} Pa	200 W	267 V	300°C	–
Mg6	2.9×10^{-4} Pa	200 W	267 V	RT	–
Mg7	3.5×10^{-4} Pa	200 W	263 V	RT	300°C (1 hr)
Mg8	1.9×10^{-4} Pa	40 W	114 V	RT	–

Table 5.2: Deposition conditions for Mg films deposition.

Before start of each deposition, the substrate was closed by a shutter and the Mg target was pre-sputtered for $\sim$ 3 min to prevent deposition of magnesium oxide and impurities adsorbed on the target surface. A significant change in the plasma color was observed during pre-sputtering of Mg target. In the first

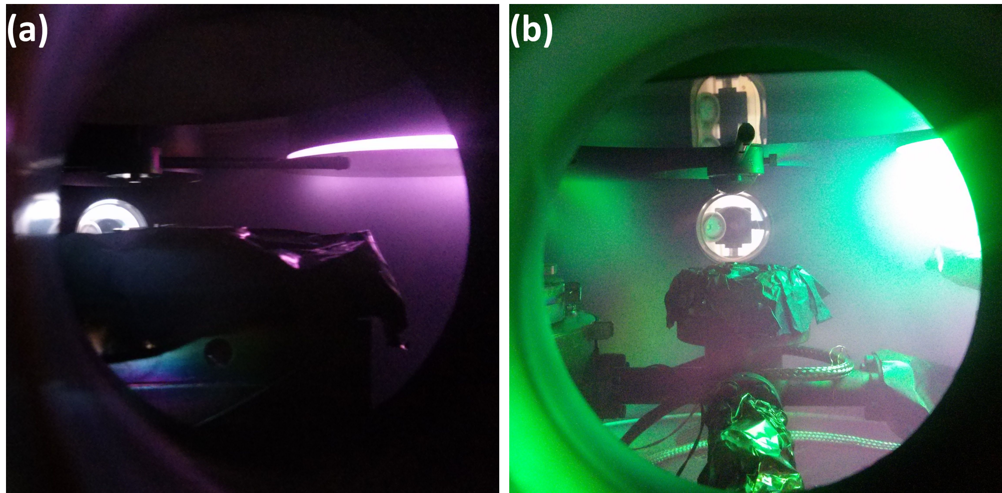

Figure 5.2: Mg/MgO plasma.

stadium of pre-sputtering impurities and magnesium oxide were sputtered out and the main color of plasma was violet, see fig. 5.2a. Then after $\sim$ 1 min within a few seconds the plasma color completely changed and turned into green, fig. 5.2b. We suppose that it indicates that all magnesium oxide was removed and sputtering of pure magnesium started. Although this phenomenon needs further investigation e.g. by optical emission spectroscopy, it can be very useful in indicating whether surface of the Mg target is still covered by oxide and the deposition can be started.

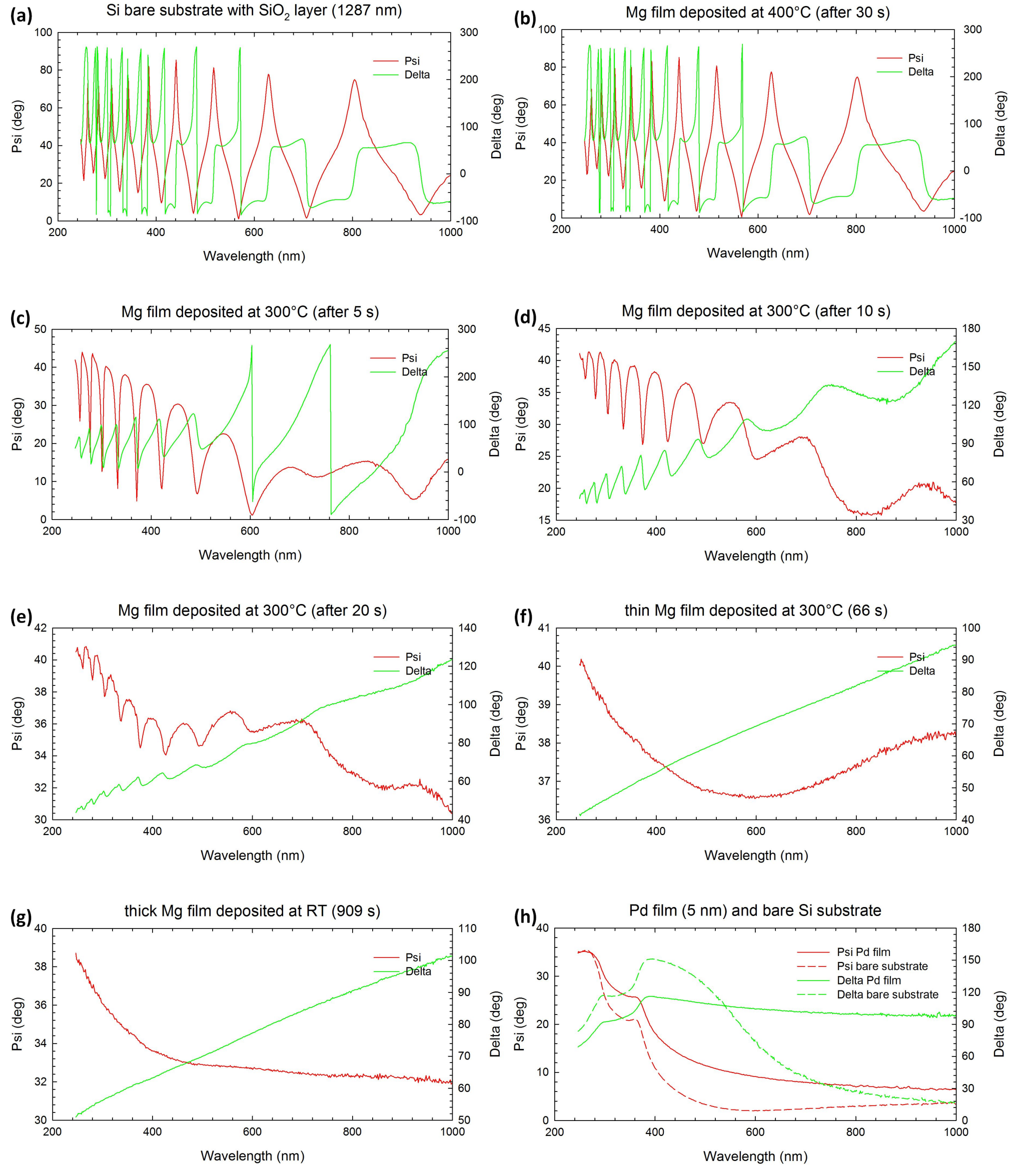

Figure 5.3: Ellipsometric data: (a) bare Si substrate with SiO_2 layer, (b) Mg deposited at 400°C for 30 s, (c), (d) and (e) Mg deposited at 300°C for 5 s, 10 s and 20 s respectively, (f) final thin Mg film deposited at 300°C, (g) final thick Mg film deposited at RT, (h) 5 nm thick Pd film and a bare substrate with a very thin native oxide layer on its surface. All Mg films are deposited on an (a) substrate (1287 nm thick SiO_2 layer on Si).

The elevated deposition and annealing temperature was chosen to 300°C. At

400°C the film growth did not occur since the film evaporation prevailed. This explanation was confirmed by the real time ellipsometric measurement.

Ellipsometric angles ψ and Δ are defined by:

$$\frac{E_p^{out}/E_p^{in}}{E_s^{out}/E_s^{in}} = \frac{|r_p|}{|r_s|} e^{i\delta_p - \delta_s} = \tan\psi \cdot e^{i\Delta}, \tag{5.1}$$

where indexes p and s stand for the p-polarization and s-polarization respectively. The dependence of ellipsometric angles on the wavelength exhibits a strong sensitivity on the film thickness, in particular for thicknesses of few nm. This is clearly visible in fig. 5.3h.

The studied film was deposited on a Si (111) substrate with a thin oxide layer on its surface. The dependence of the angles ψ and Δ on the wavelength for the bare substrate is shown in fig. 5.3a. One can see that ellipsometric data for the film deposited on a substrate heated at 400°C for 30 s, fig. 5.3b, are practically the same as those for the bare substrate. For the comparison, films deposited at the substrate heated at 300°C for 5 s, 10 s and 20 s are shown in figs. 5.3c,d,e. From inspection of fig. 5.3a-e the difference between the bare substrate and the growing film of different thicknesses is clearly visible. This confirms our opinion, that at 400°C the growing film is being immediately evaporated. In addition the data for a thin (Mg2) and a thick (Mg1) film are shown in figs. 5.3f,g. One can see that ellipsometric data are not developing much for thicker films (deposited for more than a minute) independently on the deposition temperature since the film is not transparent for visible light anymore.

Moreover applying an appropriate fitting model we were able to determine the thickness of an ultra thin Mg film. In our model we assumed 3 layers (semi-infinite Si (111) crystal, 1287 nm thick SiO_2 layer and Mg layer), smooth interfaces and homogeneous optical constants in order to simplify the model and to minimize the number of fitted parameters. The ellipsometric measurement of ultra thin Ag films and its analysis is described in more details in works [43, 44].

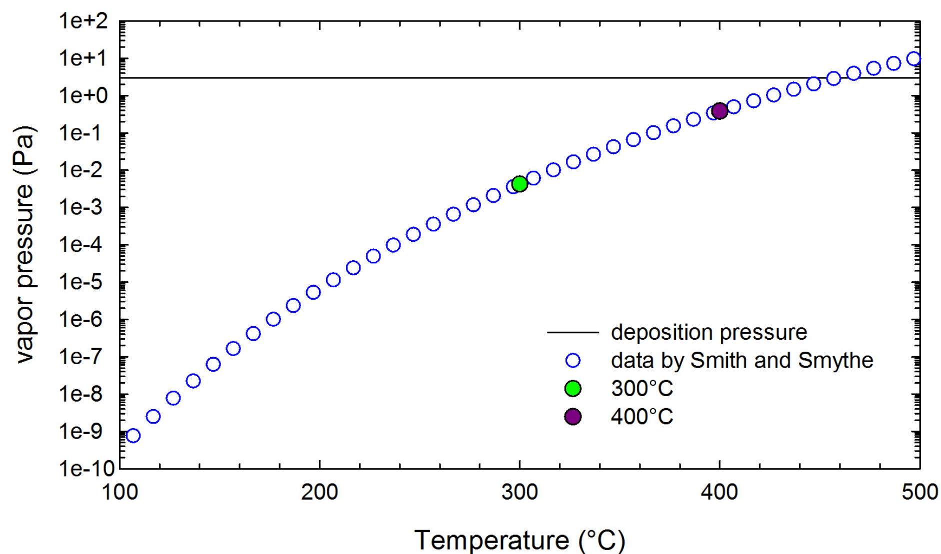

Figure 5.4: Vapor pressure over Mg calculated by eq. (5.2) published by Smith and Smythe [45].

Fig. 5.4 shows a temperature dependence of the vapor pressure over Mg determined according to the empirical formula by [45]:

$$\log p = 15.919 - 7796\,T^{-1} - 0.589 \log T - 0.16 \times 10^{-3}\,T + 0.85 \times 10^{4}\,T^{-2}. \quad (5.2)$$

At 400°C the vapor pressure is close to the deposition pressure, , i.e. the pressure of the working Ar gas, nevertheless at 300°C the pressure is lower by 2 orders of magnitude. This fact also explains why the film cannot be grown at 400°C.

A 20 nm thick Pd cap was subsequently deposited on each Mg film in order to prevent oxidation of Mg film on the air. Moreover the Pd cap facilitates hydrogen absorption during electrochemical charging [46]. The deposition rate and therefore the thickness of the Pd cap was determined using ellipsometry. A single Pd film was deposited on a Si (100) substrate with a very thin native oxide layer on its surface. Ellipsometric data for a 5 nm thick Pd film and a bare substrate are shown in fig. 5.3h. The deposition conditions: RF power 40 W, DC bias 81-84 V and deposition time 125 s were fixed for every Pd cap deposition. Thus we consider the same thickness of the Pd cap for every samples.

sample	thickness	substrate	T_{dep}	T_{ann}	deposition rate
Mg1	1540(20) nm	sapphire (0001) fused silica silicon (100)	RT	–	1.67 nm/s
Mg2	156(8) nm	sapphire (0001) fused silica silicon (100)	300°C	–	2.06 nm/s
Mg3	121(1) nm	sapphire (0001) fused silica silicon (100)	RT	–	1.53 nm/s
Mg4	125(3) nm	sapphire (0001) fused silica silicon (100)	RT	300°C	1.56 nm/s
Mg5	557(7) nm	sapphire (0001) fused silica well annealed Mg	300°C	–	0.62 nm/s
Mg6	1100(20) nm	sapphire (0001) fused silica well annealed Mg	RT	–	1.22 nm/s
Mg7	1500(30) nm	sapphire (0001) fused silica	RT	300°C	1.67 nm/s
Mg8	848(8) nm	sapphire (0001) fused silica	RT	–	0.19 nm/s

Table 5.3: Thicknesses, substrates and deposition rates for Mg films. We assume that the thickness measured by profilometry on film on a glass substrate is the same for films deposited on all substrates. From known deposition times the deposition rates were calculated.

Various substrates were chosen for Mg films deposition: sapphire (0001) and Si (100) monocrystals, amorphous fused silica (FS) (Mateck) and well annealed polycrystalline Mg (99.99%). The list of substrates, on which the Mg films were

deposited, is included in tab. 5.3. Mg substrates were polished prior to Mg film deposition using diamond cloths and 1 μm, 3 μm and 9 μm diamond suspension and subsequently annealed at 300°C under vacuum $\sim$ 1 Pa in order to anneal out all defects introduced into sub-surface region by cutting and polishing. Moreover Mg substrates were subjected to magnetron sputtering [1] for 2 min in order to remove thin oxide layer on the surface. Sapphire, Si and FS substrates were cleaned in isopropylalcohol and methanol using an ultrasound cleaner.

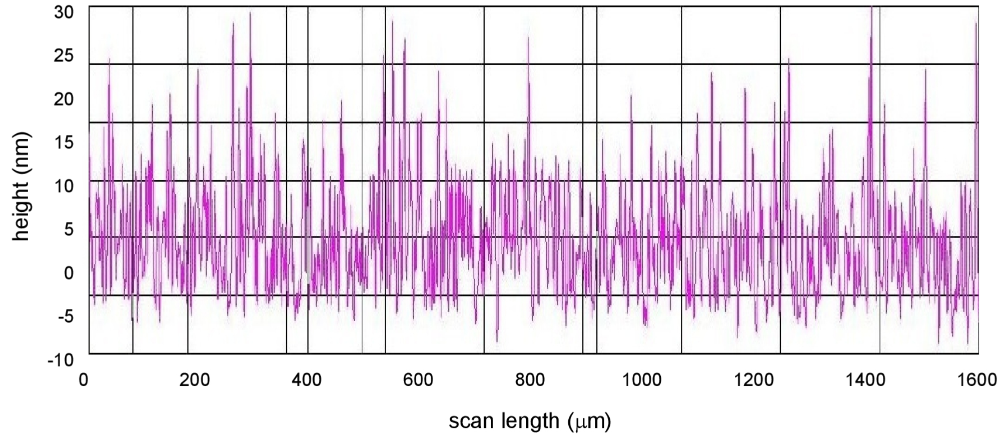

Figure 5.5: Profilometry record of the Mg5 film deposited on the glass substrate. Both roughness parameters R_a and R_q fall into the range 100 - 200 nm.

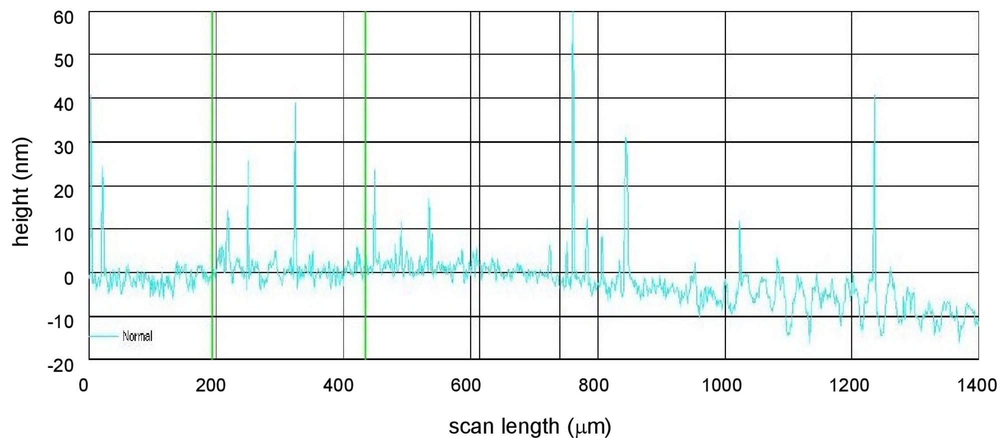

Figure 5.6: Profilometry record of the Mg8 film deposited on the glass substrate. Samples Mg1-4 and Mg6-8 exhibit similar roughness. Both roughness parameters R_a and R_q are fall into the range 1 - 10 nm.

In order to evaluate the thickness of Mg films by profilometry measurement partly covered glass substrates were used. The thicknesses of the films deposited on glass substrates determined by profilometry are listed in tab. 5.3. The thickness of 20 nm of the Pd cap was always subtracted. From the time of deposition the deposition rates were calculated. We assumed that the thickness of the film does not depend on the substrate and is the same for the films deposited on all substrates.. This assumption of course might be invalid, however this work is

[1] Mg substrate was placed on the top of the cathode and were hence bombarded by Ar ions.

focused mainly on structural and defect studies of deposited films discussed in further sections.

Roughness of Mg films was determined by the profilometry measurement as well. The sample Mg5 (see tab. 5.3) exhibits significantly higher roughness than other samples. Both roughness parameters R_a and R_q defined by eq. (4.1) fall into the range 100 - 200 nm, whereas the roughness of the other samples fall into the range 1 - 10 nm. Figs. 5.5 and 5.6 show profilometry records for the Mg5 and the Mg8 sample respectively.

5.2 SEM observations

SEM observations were performed in order to determine the surface structure and the grain size and to qualitatively estimate the roughness. The SEM micrographs for the samples Mg1 to Mg8 deposited on sapphire, FS and Si substrate (see tab. 5.3) are shown in figs. 5.8, 5.9, 5.10 and 5.11. The SEM observations were performed using secondary electrons signal (topological contrast). Electrons in the probe were accelerated by 10 kV voltage.

The mean grain sizes were roughly estimated from the SEM micrographs below and are listed in tab. 5.4 and graphically shown in fig. 5.7.

sample	substrate	grain size	sample	substrate	grain size
Mg1	sapphire	77(2) nm	Mg5	sapphire	400(10) nm
	fused silica	375(6) nm		fused silica	740(30) nm
	silicon	325(8) nm		w.a. magnesium	660(30) nm
Mg2	sapphire	133(4) nm	Mg6	sapphire	210(6) nm
	fused silica	253(6) nm		fused silica	282(7) nm
	silicon	195(7) nm		w.a. magnesium	250(10) nm
Mg3	sapphire	59(2) nm	Mg7	sapphire	259(9) nm
	fused silica	71(2) nm		fused silica	289(7) nm
	silicon	77(3) nm		–	–
Mg4	sapphire	81(3) nm	Mg8	sapphire	n.a.
	fused silica	89(3) nm		fused silica	229(6) nm
	silicon	92(2) nm		–	–

Table 5.4: Mean grain sizes estimated by SEM. n.a. = not analyzed

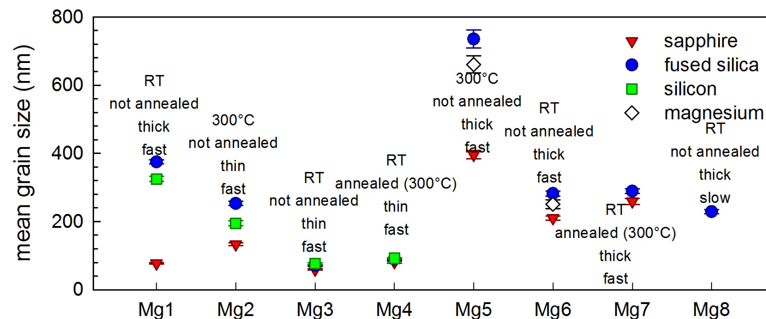

Figure 5.7: Mean grain sizes determined by SEM with listed deposition conditions.

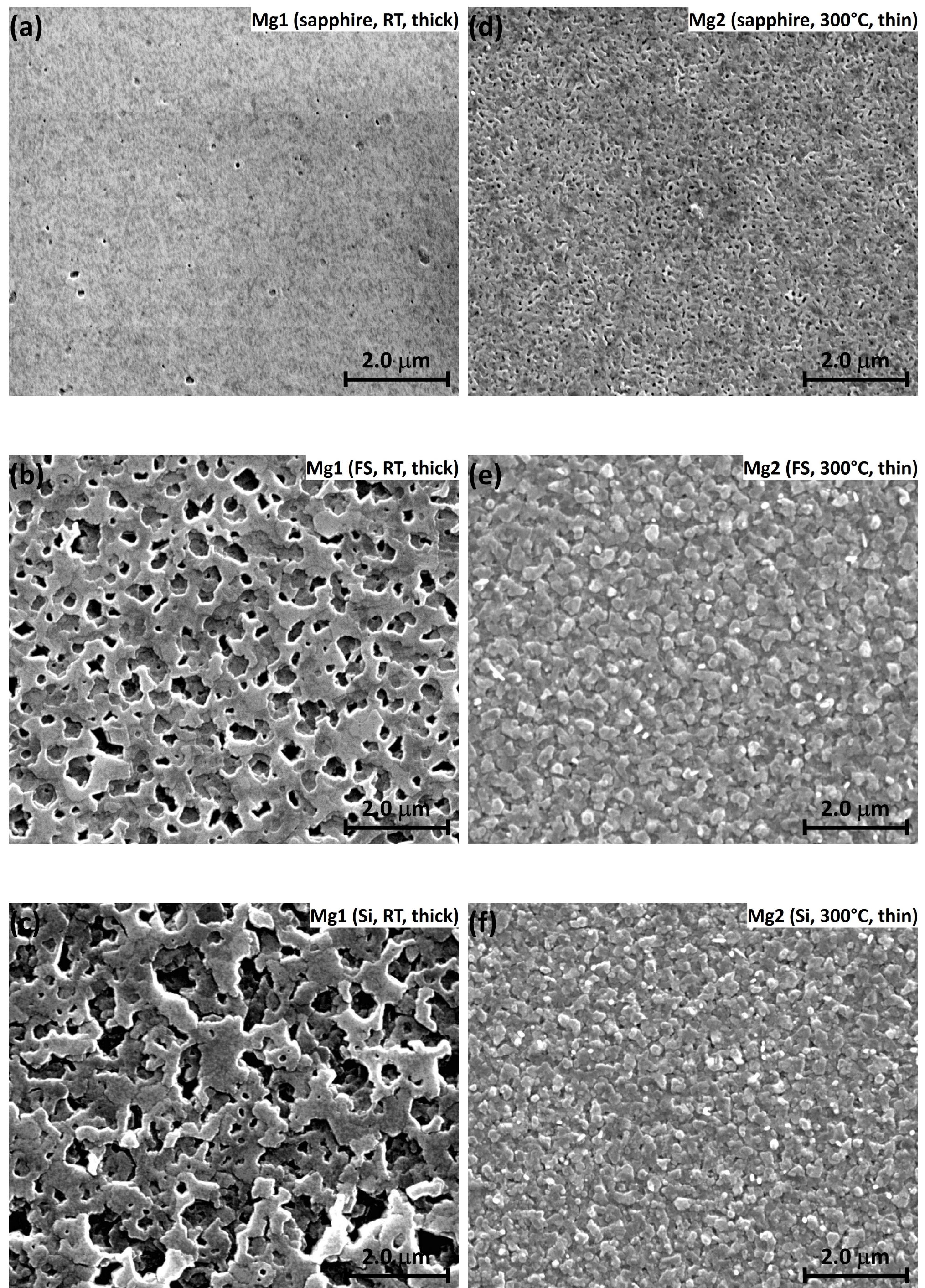

Figure 5.8: SEM micrographs of Mg samples: (a) Mg1 on sapphire, (b) Mg1 on FS, (c) Mg1 on Si, (d) Mg2 on sapphire, (e) Mg2 on FS, (f) Mg2 on Si. All micrographs were obtained using secondary electrons (topological contrast).

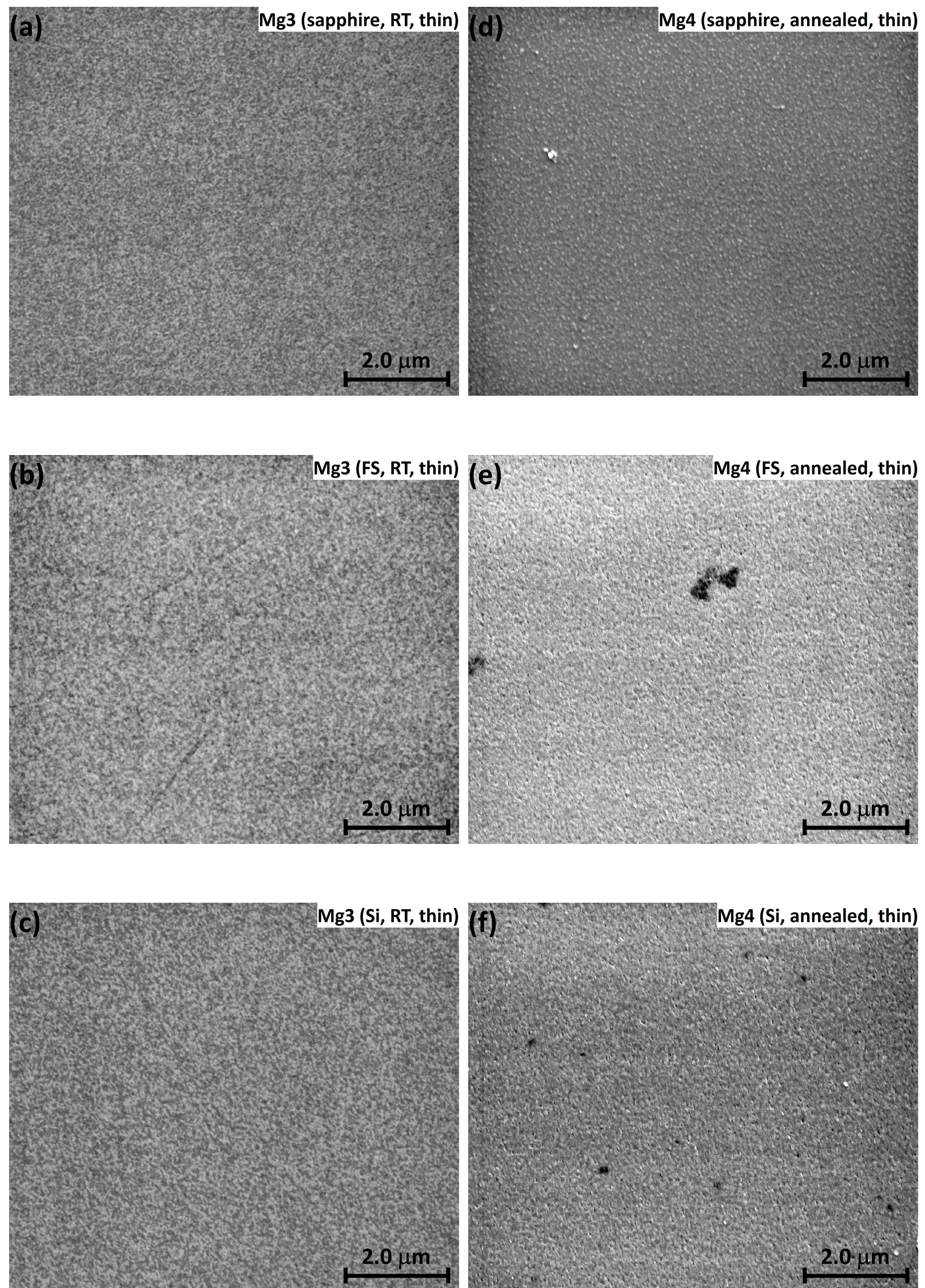

Figure 5.9: SEM micrographs of Mg samples: (a) Mg3 on sapphire, (b) Mg3 on FS, (c) Mg3 on Si, (d) Mg4 on sapphire, (e) Mg4 on FS, (f) Mg4 on Si. All micrographs were obtained using secondary electrons (topological contrast).

5.2.1 Thin Mg films

One can easily see in figs. 5.8 and 5.9 that the structure and the grain size of Mg films deposited on amorphous FS and crystalline Si (100) are very similar and different from the films deposited on sapphire (0001) substrate. This can be explained by a presence of a thin layer of native oxide which appears on every Si substrate. Therefore films deposited on FS as well as on Si were in fact growing on SiO_2 surface. Apparently due to the different crystalline structure of FS and Si, the structure of the SiO_2 top layer might be slightly different, thus there is a slight difference between Mg films on FS and Si. This difference is well visible for the Mg1 film, which exhibits the largest mean grain size.

In case of sapphire substrate the mismatch between the substrate and Mg lattice causes that Mg grains cannot grow in size much. Small grain size leads to a large fraction of grain boundaries releasing the mismatch with substrate. On the other hand the stress caused by the mismatch between the Mg film and the amorphous surface is significantly lower which enables Mg grains to be larger.

Moreover the grain nucleation is enhanced when the deposition rate is high. Since a Mg atom with relatively high kinetic energy landing on a growing film has not enough time to take over an equilibrium lattice site, it is easier to form a new nucleation center.

The effect of different thermal treatments can be well demonstrated on thin ($\sim$ 100 nm) Mg films shown in figs. 5.8d,e,f (deposited at 300°C), 5.9a,b,c (deposited at RT) and 5.9d,e,f (deposited at RT and subsequently annealed at 300°C). Independently on the substrate the deposition at elevated temperature obviously 2-3 times increases the mean grain size. The mismatch stress is thermally released, the grain growth prevails over the grain nucleation. The film roughness is very likely enhanced as well. For the same reason the annealing of a film deposited at RT causes recrystallization and the grain growth. However the effect of annealing is less pronounced than the effect of deposition at elevated temperature. This indicates that the annealing for 1 hour was not long enough for long range diffusion required for formation of coarser grains.

5.2.2 Thick Mg films

In comparison to the thin ($\sim$ 100 nm) films, the thick ($\sim$ 1.5 μm, fig. 5.8a,b,c) films exhibit obviously larger grains. The increase of the mean grain size with the thickness of the film is most likely due to the fact that the first generation crystallites attached directly to the substrate are smaller in size than the next generations growing on the top the previous generation. The mechanism controlling the grain size is the mismatch between the adjacent layers. Apparently the stress between the substrate and the film is lower than layer to layer mismatch which is decreasing with the larger mean grain size in a layer.

For each thick film (fig. 5.10) the increase of the mean grain size is evident comparing to the thin films. This effect can be well demonstrated on the Mg5 sample deposited on FS, which exhibits the biggest grain size and thus SEM micrograph for this this film shown in fig. 5.10a contains more details than the other samples. From inspection of fig. 5.10a one can see that the sub-surface crystallites are significantly smaller than the surface crystallites growing on the top of them. Moreover the structure of the thin Mg2 film (fig. 5.12a) and the

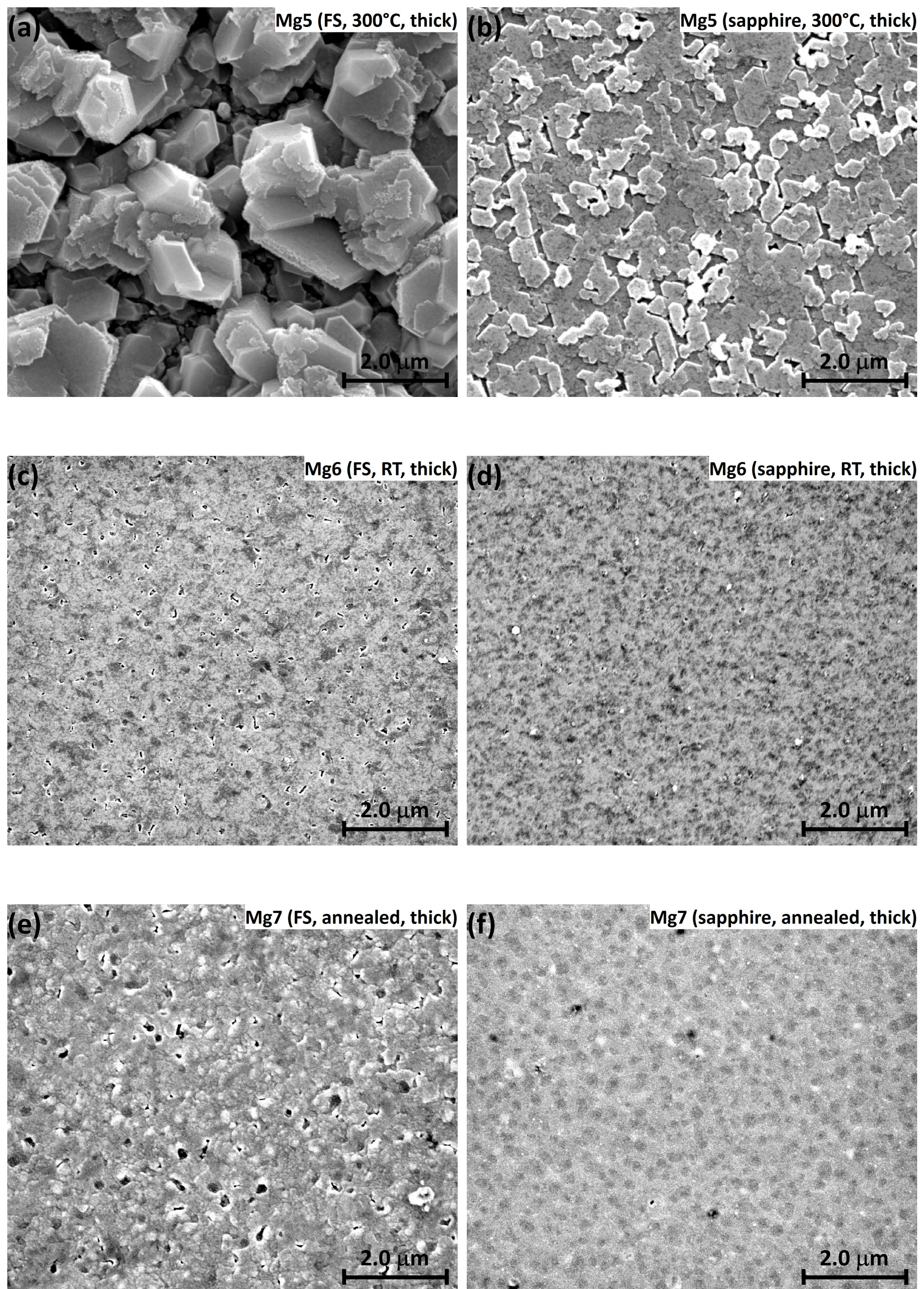

Figure 5.10: SEM micrographs of Mg samples: (a) Mg5 on FS, (b) Mg5 on sapphire, (c) Mg6 on FS, (d) Mg6 on sapphire, (e) Mg7 on FS, (f) Mg7 on sapphire. All micrographs were obtained using secondary electrons (topological contrast).

thick Mg5 film (fig. 5.12b), both deposited on FS at 300°C, is practically the same, the difference is only in the magnification due to the different grain sizes.

Since during the deposition of the thick film the next generation of grains grows on the top of the previous generation and thus does not "sense" the substrate below, one could expect a layer-by-layer growth, especially for deposition at elevated temperature since the mobility of Mg atoms is higher to settle in equilibrium sites. However the structure is completely opposite (see fig. 5.10a), grains in the films deposited at high temperature form columnar structure. This effect is caused by a high deposition rate that sluggish the mobility of Mg atoms. Lets assume that most of Mg atoms landing on the previously formed column will find its equilibrium site there. Similarly the most of the atoms landing into the inter-columnar space (holes) will end there, but there must be a significant part of atoms that will reach the columns and take over its equilibrium site there. Hence the growth of the columns overweights the filling of holes between them resulting in the columnar structure as was observed. Similar effect occurs for the film deposited on sapphire (fig. 5.10b), although because of the crystalline substrate and therefore smaller grains it is less pronounced.

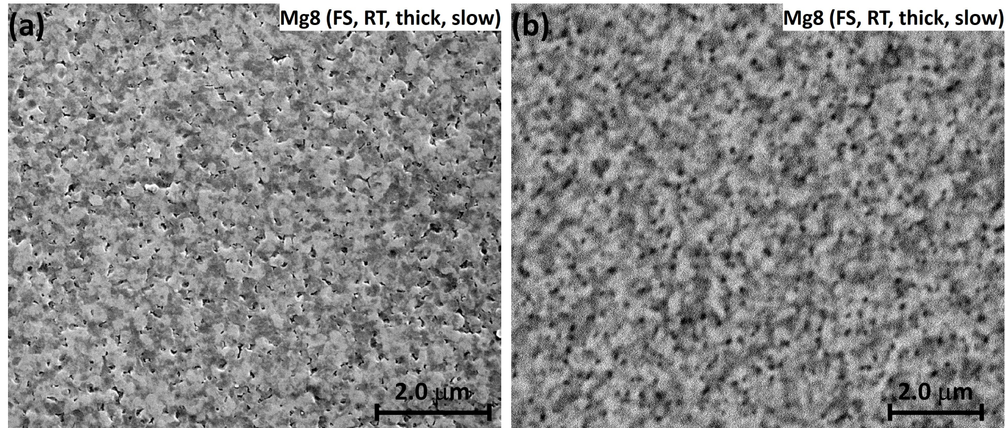

Figure 5.11: SEM micrographs of the Mg8 sample deposited on FS obtained using (a) secondary electrons (topological contrast) on the FEI Quanta 200 SEM and (b) using back-scattered electrons on the FEI Phenom microscope. Observation of the Mg8 sample deposited on sapphire was not performed.

In fig. 5.11 we compare SEM micrographs for the same film obtained by two different microscopes. Obviously the micrograph providing more details provides also more precise estimation of the grain size. In fig. 5.12 we similarly compare SEM micrographs for the films Mg2 and Mg5 which differs only by the level of magnification (thickness of the film respectively). As it was discussed before, the SEM images seems to be virtually the same. Although the magnification for the Mg5 film is 10 times higher than that for the Mg2 sample, the mean grain size, determined from micrographs taken using higher magnification, is only 3 times higher than that for the Mg2 film.. This indicates that due to the lack of more details in SEM micrographs the mean grain sizes in nanocrystalline films could be overestimated.

The effect of different thermal treatment for thick films is virtually the same as described in previous section. Again due to the release of the mismatch stress the deposition at elevated temperature increases 2-3 times the mean grain size

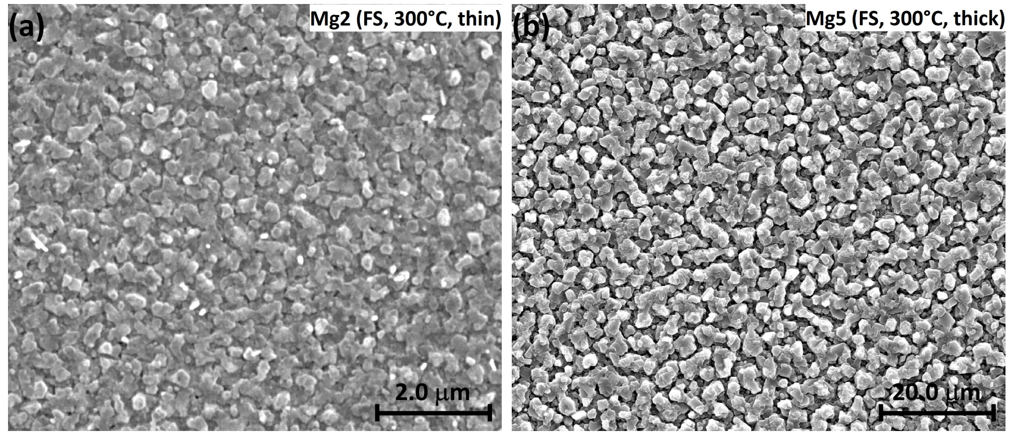

Figure 5.12: SEM micrograph of (a) thin Mg2 sample on FS, (b) thick Mg5 sample on FS (lower magnification). Both samples were deposited at a substrate heated at 300°C and differ only by thickness. Both micrographs were obtained using secondary electrons (topological contrast).

both for the sapphire and the FS substrate. However the annealing procedure for the thick Mg film was modified. Instead of annealing of the Mg films and subsequent deposition of Pd cap at RT like in the case of thin films, the thick Mg films were annealed after capping with Pd. As a consequence a Mg-Pd phase was formed on the surface and the recrystallization and the grain growth due to the annealing was less pronounced than for thin films.

The roughness of thick Mg films in figs. 5.8b,c is obviously enhanced. Mg films seems to be porous, but the roughness and porosity cannot be evaluated by SEM. Moreover SEM mages for the Mg1 and Mg6 samples (see figs. 5.8a,b and 5.10c,d) show different features despite the fact that these films were deposited at very similar conditions and differs only by the thickness and the deposition rate. Due to the lower SEM contrast the surface roughness cannot be easily estimated.

Atomic force microscopy (AFM) uses the same principles as profilometry and provides unlike SEM both the lateral and the vertical resolution. Hence the AFM measurement was performed on the Mg6 film deposited on FS (5.14) and was compared with the SEM result (fig. 5.13). The depth of "holes" in the film is approximately 50 nm. The AFM image for the Mg6 film lies between the rougher SEM image for the Mg1 and the smoother SEM image for the Mg6 film, hence besides the extra vertical resolution AFM provides a different view to the film structure and would be very useful as a complementary method of the films analysis to obtain more precise picture of their structure.

In order to reduce the roughness and the grain size of the thick film deposited at RT (Mg1 and Mg6 samples) the deposition at RT but with lower deposition rate was performed in case of the Mg8 sample. From inspection of fig. 5.11a one can see that the roughness and the grain size were actually lowered compared to the film deposited using faster rate. However this effect is in part very likely caused by the lower thickness of the film (approximately half of the thickness of the film with fast deposition rate) and will require further investigation connected with AFM analysis.

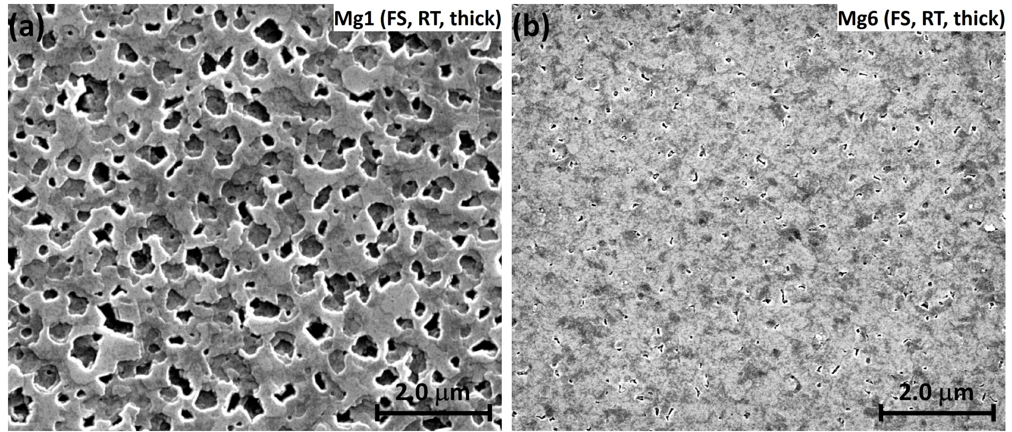

Figure 5.13: SEM micrographs view of Mg1 (a) and Mg6 (b) film deposited on FS.

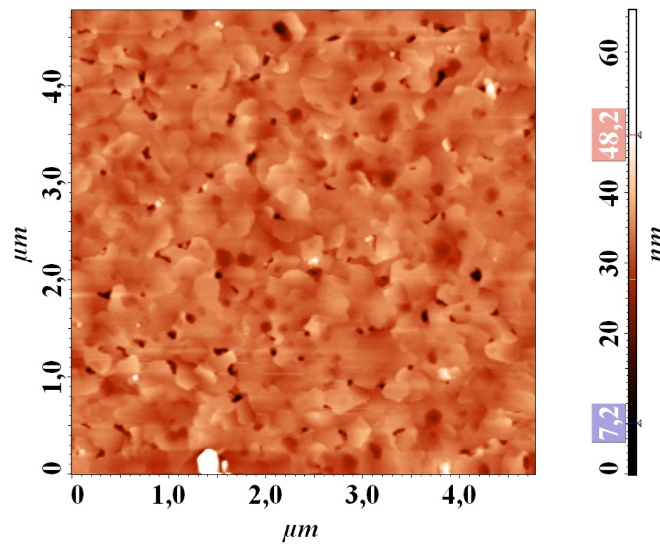

Figure 5.14: AFM image (measured by a tapping mode) of Mg6 film deposited on FS with the extra vertical resolution.

5.2.3 Mg films deposited on Mg

Since the structure and the grain size are controlled by the misfit stress at the interface between the film and the substrate (crystalline or amorphous), a well annealed (w.a.) magnesium substrate with low concentration of defects was used for deposition of Mg films.. Hence the Mg film growing on the Mg substrate was expected to exhibit largest grains or be even epitaxial.

The SEM micrographs of the thick Mg films deposited on the Mg substrate in fig. 5.15 were obtained using BSE signal, which is able to provide topological contrast as well. The film structure is polycrystalline, similarly to the film deposited on sapphire, FS and Si. Moreover the mean grain sizes are practically the same as those for the films deposited on FS considering the lower resolution of SEM images in fig. 5.15.

It seems that the growing film does not feel the Mg atoms in the substrate below and grows similarly as the film on the amorphous FS. This growth mode can have two possible explanations. Although surface layers of the Mg substrates were removed by magnetron sputtering, we cannot exclude a possibility that on

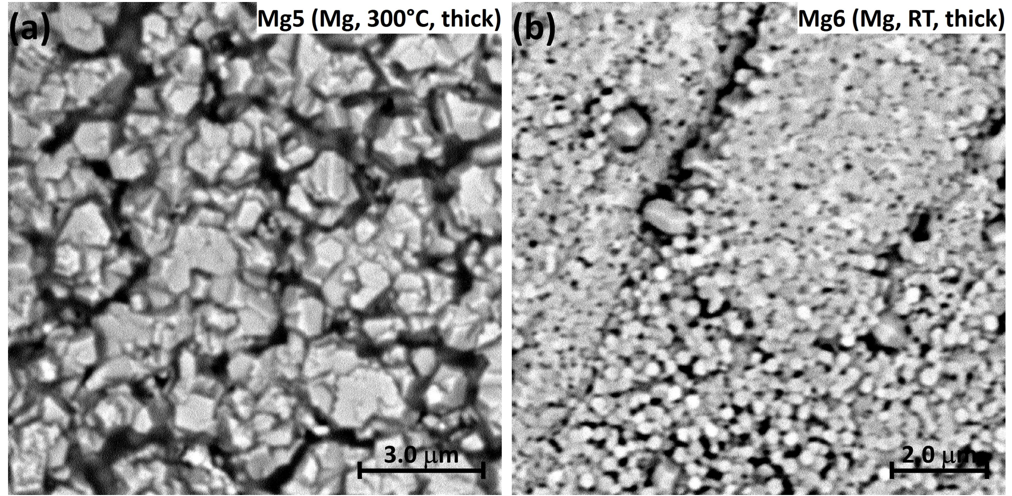

Figure 5.15: SEM micrographs of Mg5 (a) and Mg6 (b) films deposited on the well annealed Mg substrate obtained from back-scattered electrons signal providing topological contrast. The measurement was performed on FEI Phenom microscope

the top of the substrate was still a thin native oxide layer, which either was not completely removed by sputtering or was formed during a transport of the Mg substrate to the magnetron sputtering chamber (within few seconds). Then the film would grow on an amorphous oxide layer similarly as was discussed for films growing on the Si substrate and thus is similar to the films on FS. Another explanation might be a high deposition rate. Since the deposited atoms have not enough time to diffuse to an equilibrium lattice sites, new nucleation centers are formed and the film is growing with the most densely occupied plane parallel to the surface (as was revealed by XRD). This explanation is supported by the columnar structure similar to that for the Mg5 film growing on FS substrate.

Since the structure of films deposited on Mg substrate is similar as for the other substrates, we expect the same behaviour during the thermal treatment. Indeed it was observed that the deposition on a Mg substrate heated at 300°C results in coarser grains compared to the film deposited at RT.

One can see in fig. 5.15b the film growing in a vicinity of a grain boundary in the Mg substrate separating 3 different grains. The film grains are significantly smaller than the substrate grains, which supports the idea of insensitivity of a growing film on the Mg substrate.

5.3 XRD results

XRD studies were performed in order to determine the phase composition and the out-of-plane lattice parameter and to estimate texture. In addition the microstrains and the mean crystallite size was estimated from the line broadening of X-ray diffraction profiles.

5.3.1 Texture studies

Figs. 5.17 - 5.21 and 5.25 show the X-Ray diffractograms obtained from Bragg-Brentano symmetric scan of Mg films deposited on Si (100), FS, sapphire (0001) and well annealed Mg substrates (see tab. 5.3). By comparison of the observed reflections with the databases of powder diffractograms the measured diffraction peaks were indexed and the phases present in the samples were identified.

Studied Mg films crystallize in a hexagonal closed packed (hcp) lattice, i.e. they have the same structure as the bulk Mg. Pd over-layer exhibits face centered cubic (fcc) structure, again the same as for the bulk Pd. The films deposited on Si, FS and sapphire substrate exhibit always a strong fiber texture independently on the thickness and the deposition conditions. The Mg films grew predominantly in such orientation that of the most densely populated basal plane (0001) was parallel with the substrate surface, while the Pd over-layer grew on the top of Mg film with (111) planes (again most densely populated one) parallel with the surface. This is in a good agreement with other studies of Mg films [4, 7, 10, 11].

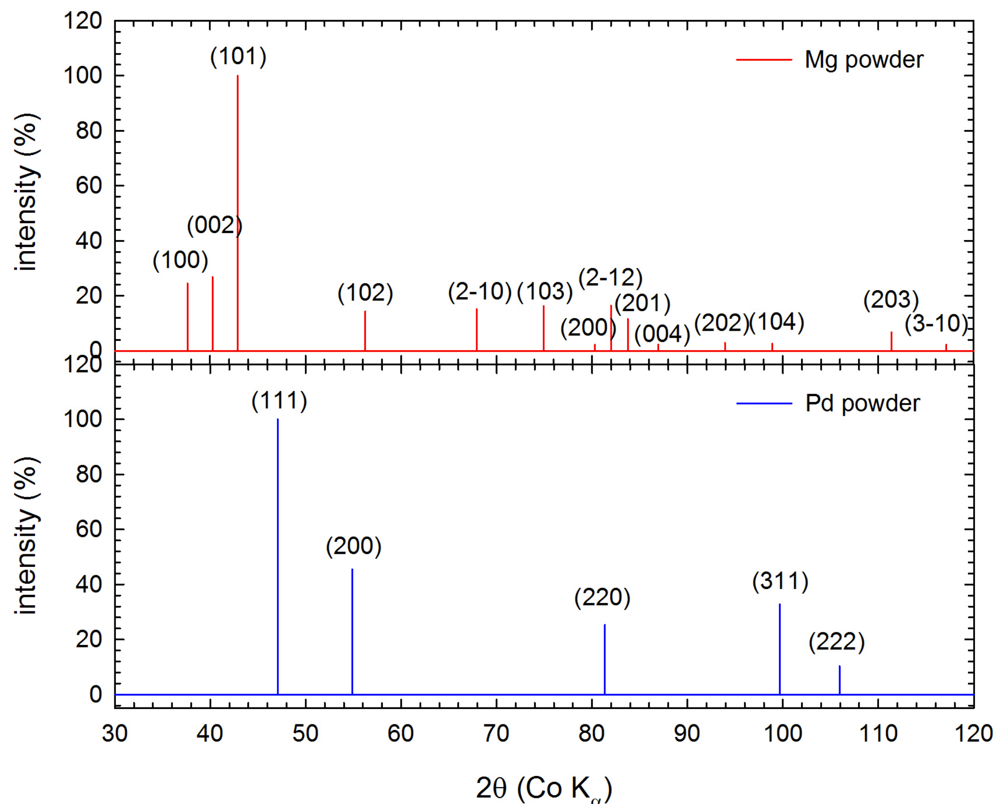

Figure 5.16: Theoretical powder diffractograms of hcp Mg and fcc Pd. All values were generated with program CaRIne Crystallography 3.1.

For some of films deposited at 300°C weak diffractions from Mg $(10\bar{1}1)$ [2] and Pd (100) planes were observed. In the theoretical powder diffractogram for Mg the intensity of the Mg(101) peak (the strongest reflection) is approximately 4 times

[2] In this text we denote the hexagonal crystallographic planes using the 4 Miller indexes notation (hkil), where i is not an independent index and and obeys the relation $i = -h - k$. On the contrary the diffraction peaks are labeled using the Laue 3 index notation (hkl) which is commonly used for indexing of XRD diffraction patterns.

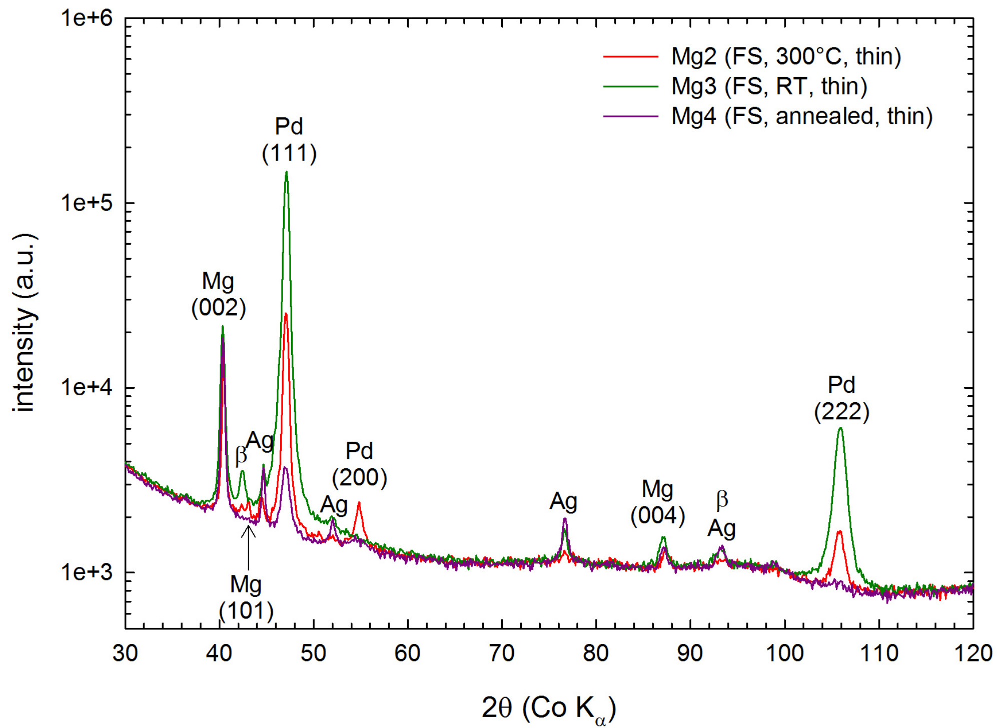

Figure 5.17: X-ray diffractograms of thin Mg films (see tab. 5.3) deposited on FS substrate measured in the Bragg-Brentano symmetric geometry.

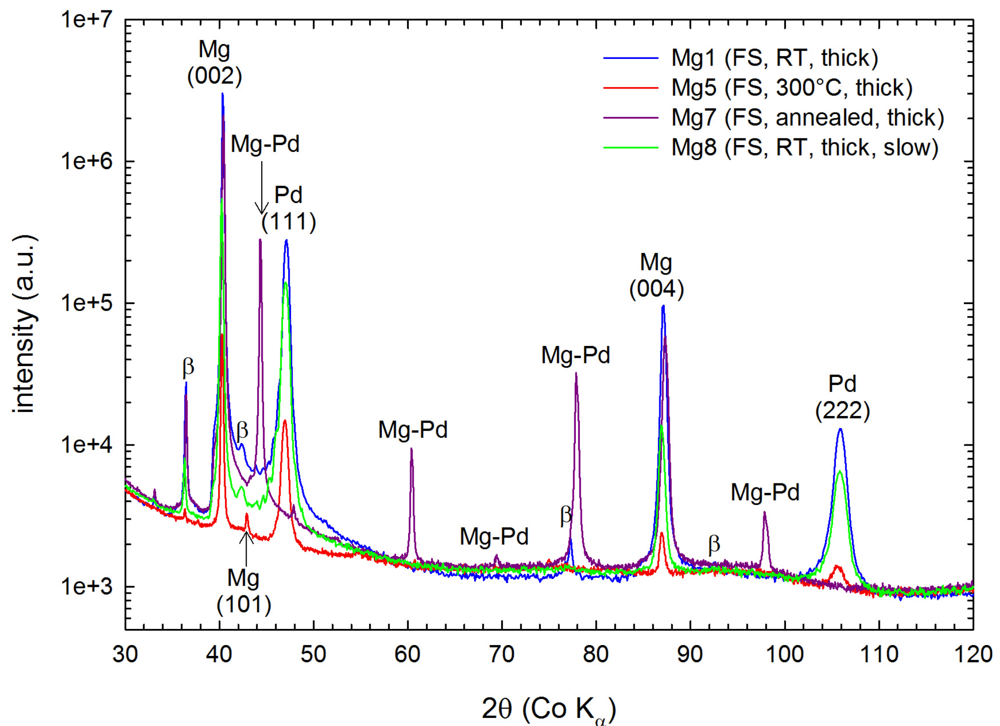

Figure 5.18: X-ray diffractograms of thick Mg films (see tab. 5.3) deposited on FS substrate measured in the Bragg-Brentano symmetric geometry. A violet curve represents Mg7 film deposited at RT and annealed for 1 hour with Pd cap leading to the formation of Mg-Pd phase.

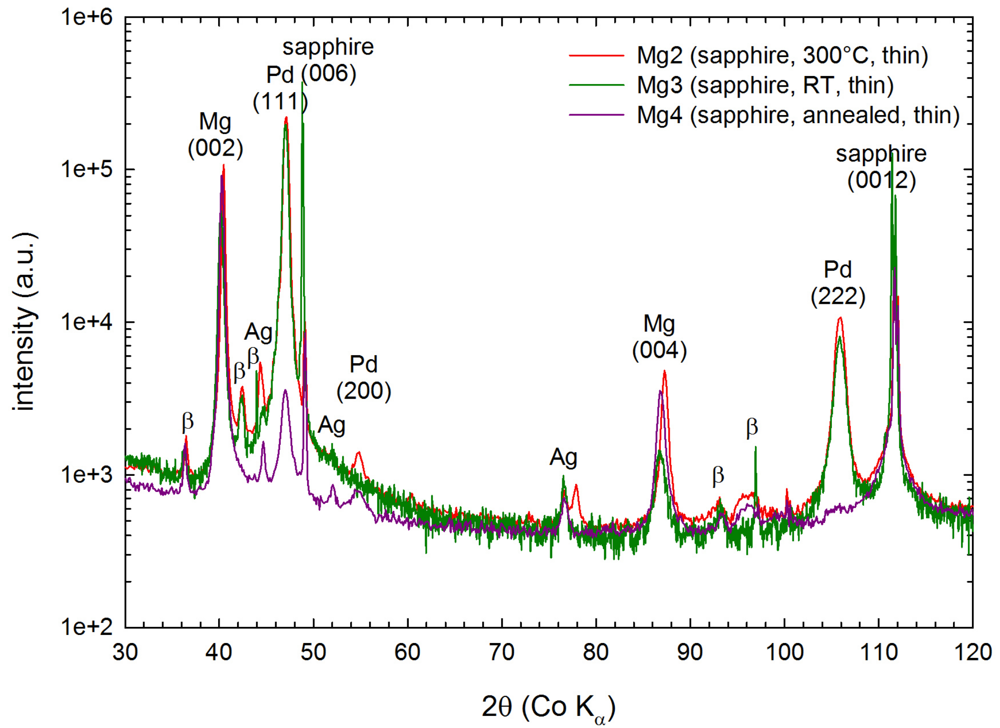

Figure 5.19: X-ray diffractograms of thin Mg films (see tab. 5.3) deposited on sapphire (0001) substrate measured in the Bragg-Brentano symmetric geometry.

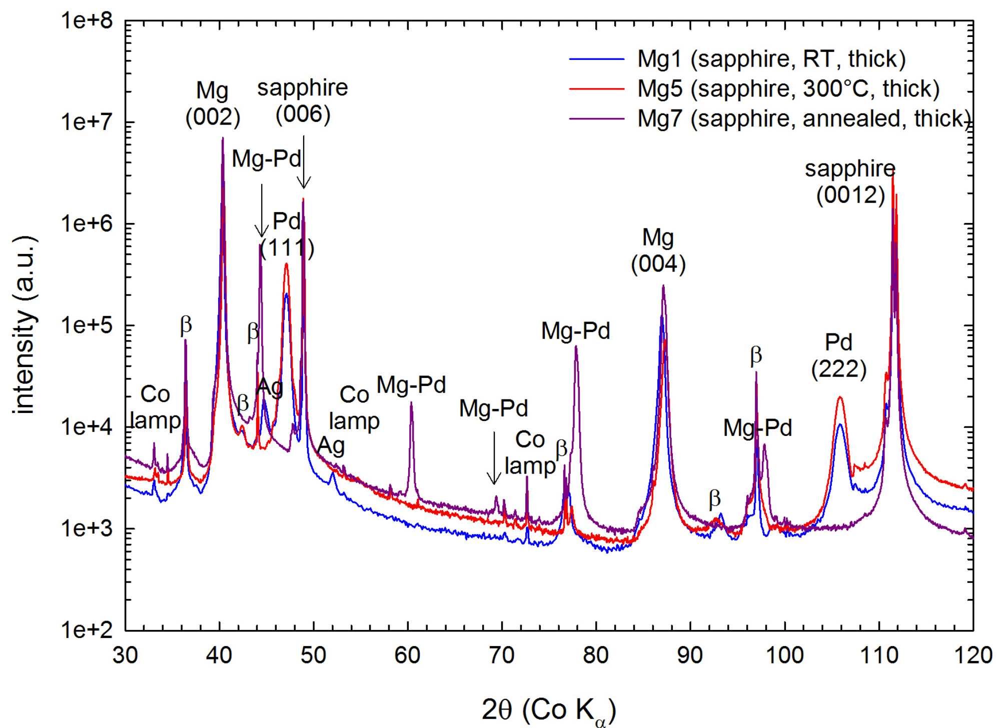

Figure 5.20: X-ray diffractograms of thick Mg films (see tab. 5.3) deposited on sapphire (0001) substrate measured in the Bragg-Brentano symmetric geometry. A violet curve represents Mg7 film deposited at RT and annealed for 1 hour with Pd cap leading to the formation of Mg-Pd phase.

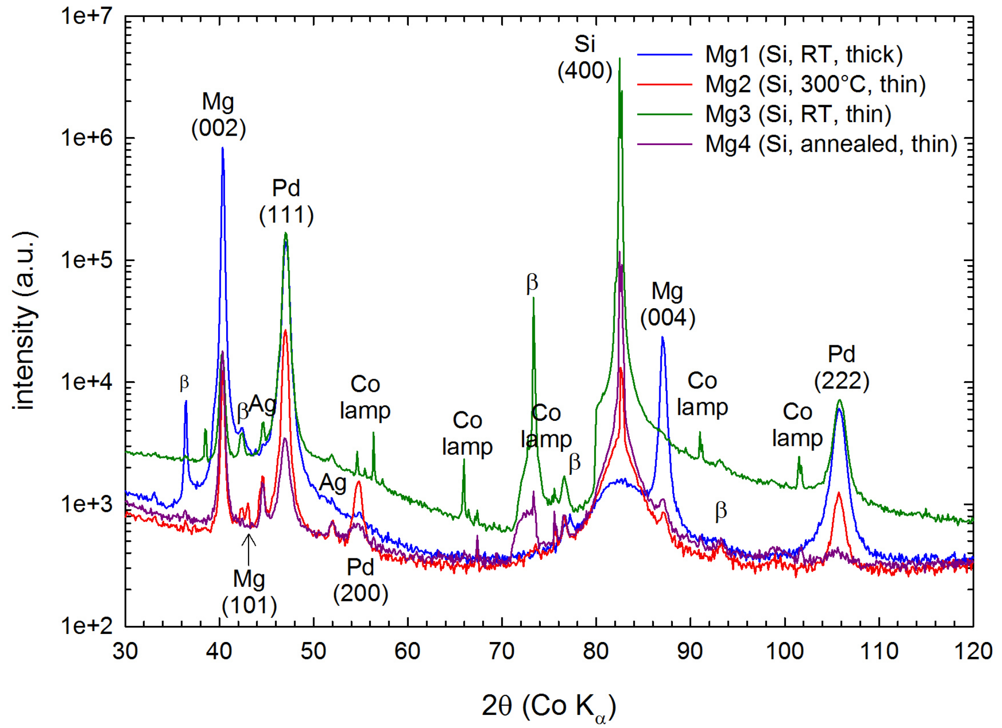

Figure 5.21: X-ray diffractograms of Mg films deposited on Si (100) substrate measured in the Bragg-Brentano symmetric geometry. The XRD patterns for the thick Mg1 film as well as the thin Mg2-4 films are plotted in the figure (see tab. 5.3).

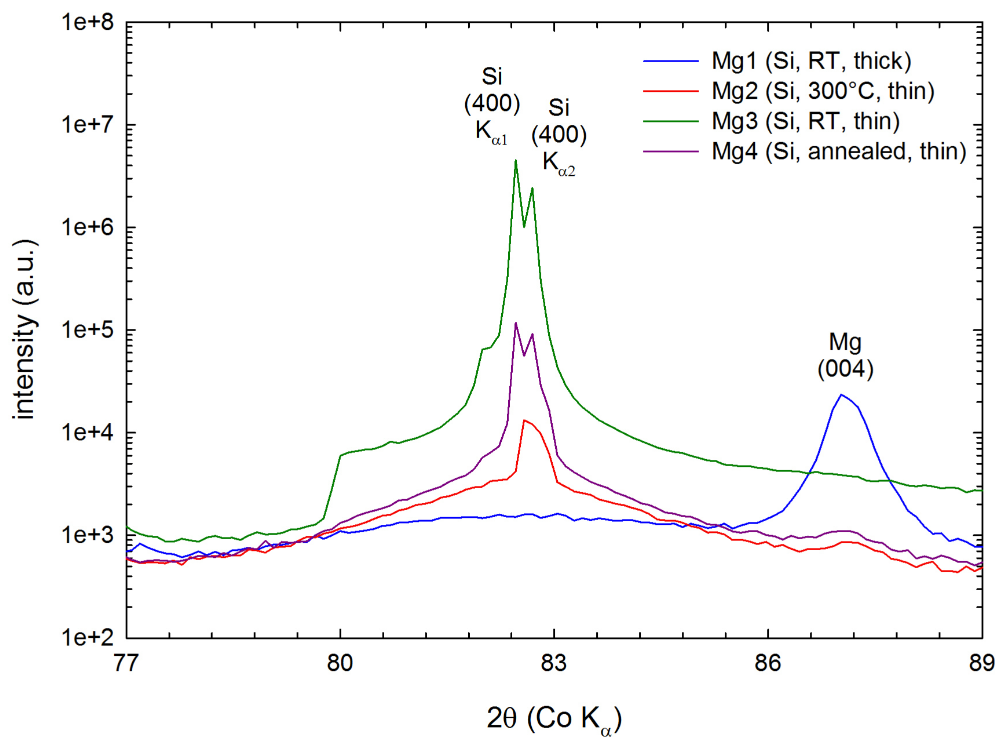

Figure 5.22: Detail view of the X-ray diffractograms of Mg films deposited on Si (100) substrate showing the Si (400) peak in detail.

higher than the intensity of the Mg(002) peak, but in the Mg films the intensity of the Mg (002) reflection is by 2-3 orders of magnitude higher than the intensity of the Mg (101) peak. The theoretical intensity of Pd (111) peak (strongest reflection) is approximately 2 times higher than the intensity of the Pd (200) peak (the second most intense reflection), but in the measured diffractograms the Pd (111) peak is by 1-2 orders of magnitude higher than the Pd (200) reflection. The theoretical powder diffractograms for Mg and Pd are shown in fig. 5.16

The presence of other reflections than those corresponding to diffraction at (0001) and (111) planes for Mg and Pd, respectively, indicates that in the films deposited at 300°C some crystallites grew in the orientation which differs from the dominant growing mode and additional texture components appeared. It would be appropriate to perform an ω-scan measurement, where the angle between the X-ray beam and the detector is fixed at 2θ corresponding to the Bragg diffraction condition for given reflection (e.g. for peak Mg (002)) and the sample is tilted by angle ω. Hence the diffraction signal comes from planes tilted by various angle with respect to the surface and from the width of the ω-scan (the dependence of the intensity on the ω angle) we obtain more detailed picture of the sharpness of texture of the film.

We suggest that the growth of Mg and Pd film with most densely occupied planes parallel with the surface is a consequence of the high deposition rate of Mg films and is in a very good agreement with SEM observations (dominating grain nucleation, columnar growth).

One can see that the XRD patterns in figs. 5.17 - 5.21 contain many small peak artifacts. Although the iron β-filter was employed, for strong reflections (Mg(002), Pd(111) and the diffraction peaks from the substrate) the diffraction of the K_β radiation is visible. Since K_β line has shorter wavelength than K_α, the K_β satellites are located before the mean K_α reflections, i.e. at lower diffraction angles. The presence of silver diffraction peaks in the Mg1-4 samples was caused by silver paint conductive layer at the edges of the films applied during previous SEM measurements. Since the films were deposited on a dielectric substrates their edges were covered by silver emulsion paste in order to prevent charging of the film during the SEM observations. Si and sapphire single crystalline substrates obviously contributed to the diffractogram by very narrow peaks with very high intensity. Moreover due to the suitable orientation of these crystals (large crystal fulfilling the diffraction conditions) besides the $K_{\alpha 1}$, $K_{\alpha 2}$ and K_β reflections the diffraction of other wavelengths coming from the Co X-ray lamp (see its spectrum in 4.5) are visible. The presence of the Fe absorption edge is visible for the most intense peaks too. These additional reflections produced by Co X-ray lamp are best visible for the Mg3 film deposited on Si in fig. 5.21.

Finally one can see in fig. 5.22 that the Si(400) peak consists in fact of two peaks both with the same 2θ angle. The narrow one comes from the diffraction on the Si(100) planes of Si monocrystal. The broad peak comes most probably from a sub-surface region containing high density of dislocations introduced by mechanical polishing of the substrate.

The absence of the narrow peak for the Mg1 film is by the slight tilting of the sample. This led to disappearing of the Si(400) peak since it was not anymore in the position determined by the diffraction condition.

Thick Mg7 films were deposited at RT, subsequently the Pd cap was deposit-

ed and the whole Mg-Pd film was annealed for 1 hour at 300°C. This lead to a mixing of the Pd over-layer with Mg and the formation of Mg-Pd phase on the surface. One can see in figs. 5.18 and 5.20 that for the Mg7 films the Pd peaks completely disappeared and 5 new peaks belonging to the Mg-Pd phase appeared. According to the equilibrium phase diagram for Mg-Pd system, shown in fig. 5.23, the formation of various Mg-Pd phases is possible. However comparing the positions of Mg-Pd peaks in our diffractograms (shown in tab. 5.5) with XRD records available in databases we were not able to find a Mg-Pd phase which gives reflections matching all the peaks observed in the Mg7 films.

From inspection of figs. 5.18 and 5.20 it is clear the Mg-Pd peaks are narrower than Pd peaks of other films, their width is more similar to the width of Mg peaks. This indicates that crystallites of the Mg-Pd phase is relatively large and Pd atoms thereby diffuse deep into the Mg film, where they form the Mg-Pd phase. However due the relatively low annealing temperature and the short annealing time the formation of equilibrium Mg-Pd phase may not be completed.

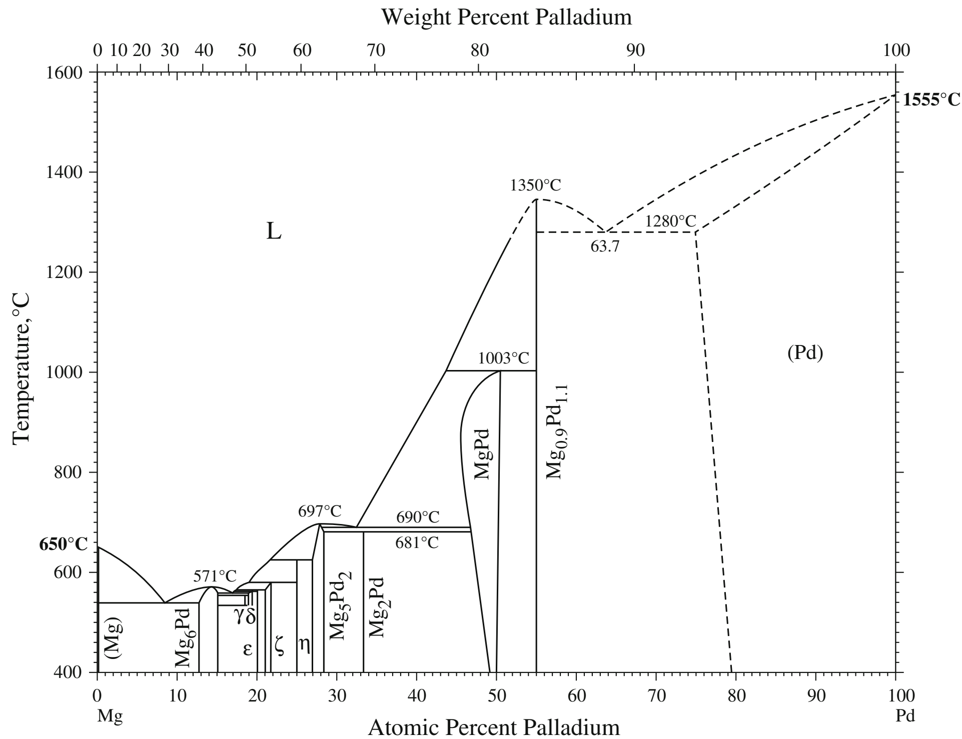

Figure 5.23: Equilibrium phase diagram for Mg-Pd system by Okamoto [47].

We performed a very rough simulation of a modified hcp Mg cell, where we replaced one Mg atom with Pd, see fig. 5.24. Since the distance between the (111) planes in a fcc Pd crystal ($a/\sqrt{3}$ = 0.225 nm) [48] is smaller than the distance between the (0002) planes in a hcp Mg crystal ($c/2 = 0.261$ nm) [48], it is expected that substitution of Mg atoms the (0001) planes in a hcp Mg crystal by Pd atoms leads to a contraction of the c-lattice parameter. Indeed the peak positions labeled in tab. 5.5 can be well reproduced by assuming the hcp structure depicted in fig. 5.24 with the lattice parameter $c = 0.475$ nm, i.e. the distance between the Mg and Pd sublattice $c/2 = 0.237$ nm is close to the average of the inter planar distances for (111) planes in fcc Pd and (0002) planes in hcp

Mg. Hence the Pd atoms diffuse into hcp Mg lattice and form Pd sublattice in alternating basal planes. The existence of two other reflections at 60.4°and 77.9°indicates that in addition to the structure in fig. 5.24 another yet unknown configuration of Mg-Pd compound exists in the sample.

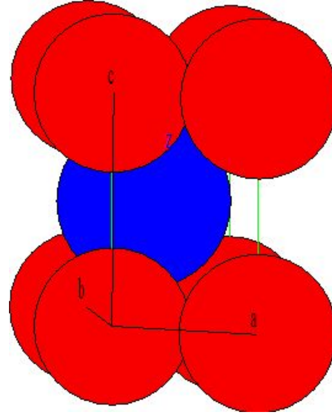

Figure 5.24: Modified hcp Mg cell. One Mg atom was replaced with Pd.

FS	Sapphire	Reflection	Simulation
44.3363(1)°	44.3222(3)°	(002)	44.6°
60.3765(4)°	60.3553(4)°	–	–
69.38(1)°	69.357(6)°	(003)	68.8°
77.8583(3)°	77.8314(7)°	–	–
97.864(2)°	97.82(1)°	(004)	97.8°

Table 5.5: Positions 2θ of the Mg-Pd reflections belonging to the Mg-Pd formed in the Mg7 films deposited on FS and sapphire substrates and position 2θ of the reflections belonging to the simulation of modified hcp Mg cell.

Fig. 5.25 shows X-Ray diffractograms obtained using the Bragg-Brentano symmetric scan for Mg films deposited on the well annealed Mg substrates. Unlike the films deposited on Si, FS and sapphire, the diffractogram in fig. 5.25 contains besides Pd(111), Pd(222) and K_β reflections several peaks originating from the Mg substrate itself. Unfortunately the contribution from the Mg substrate and the Mg film cannot be separated, so in this case it is difficult to draw some conclusion about the texture of the Mg film from the diffraction pattern measured in the Bragg-Brentano symmetric geometry.

In the grazing incidence (parallel beam) geometry with the angle of incidence fixed at 1°the situation is different since the penetration depth of X-rays is approximately 1 μm and the contribution of the film is thus substantially enhanced. Fig. 5.26 shows the diffractograms obtained using the grazing incidence geometry. One can see in the figure that the Mg(002) peak is strongly enhanced comparing to the Mg(100) peak (with similar theoretical intensity) as well as to the Mg(101) peak (with 4 times higher theoretical intensity for randomly oriented crystallites). This enhancement is more evident for the Mg6 film since its thickness is $\sim$ 1.1 μm, while the thickness of Mg5 film is $\sim$ 0.56 μm only and the diffractogram, therefore, contains also a significant signal from the substrate. The measurement in the grazing incidence indicates that the Mg films deposited

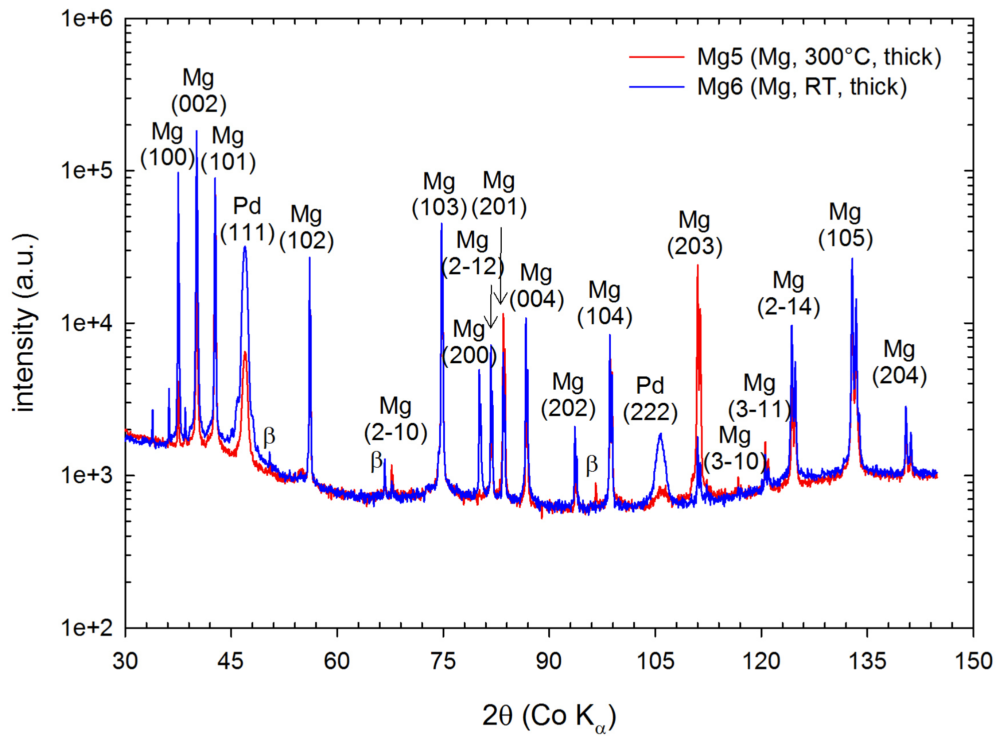

Figure 5.25: X-ray diffractograms for the thick Mg films deposited on the well annealed Mg substrate measured in the Bragg-Brentano symmetric geometry.

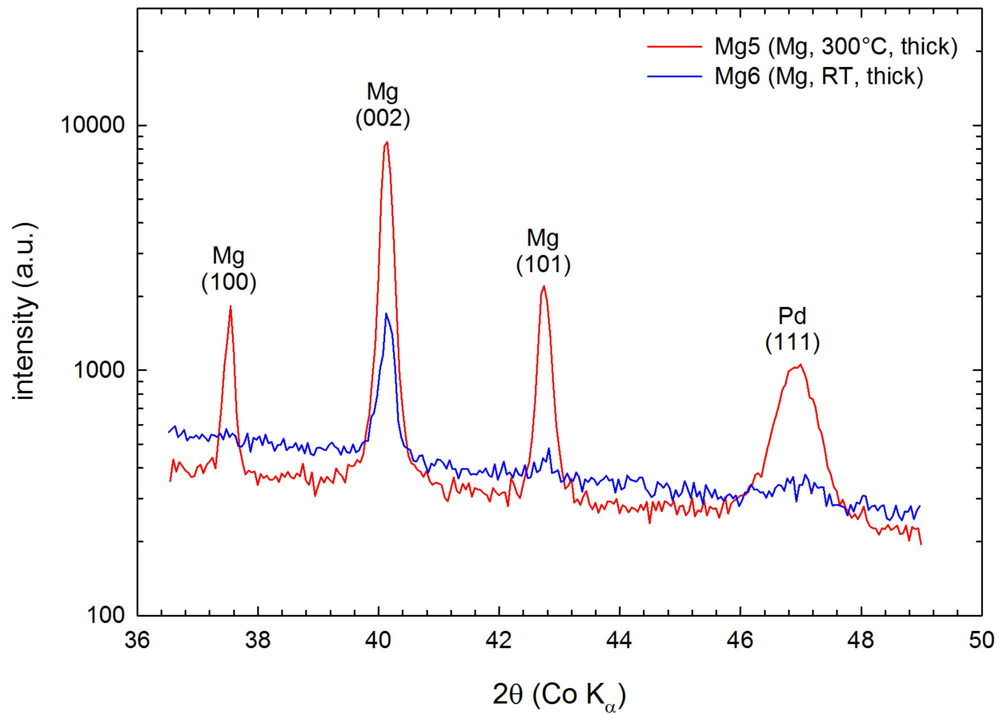

Figure 5.26: X-ray diffractograms for the thick Mg films deposited on the well annealed Mg substrate measured in the grazing incidence geometry with the constant angle of incidence fixed at 1°.

on the well annealed Mg substrate have a similar texture as those deposited on Si, FS and sapphire substrates. This is supported also by the fact that Pd (111) and Mg (002) reflections are present with high intensity also in the spectra measured in the Bragg-Brentano geometry. Moreover SEM observations reveled that the films deposited on Mg substrate have similar morphology as those deposited on the other substrates. However we need to remember that the diffraction signal from grazing incidence geometry measurement did not came from the planes parallel with the surface as it was in the Bragg-Brentano scans, but it comes from the planes tilted at angle of $\sim 20°$with respect to the surface.

5.3.2 Cohen-Wagner analysis

The diffractograms in figs. 5.17 - 5.21 were fitted peak-by-peak by the Pseudo-Voight functions and the background below the peaks was approximated by 5th order polynomial. From positions 2θ obtained by fitting of peaks Mg(002), Mg(004), Pd(111) and Pd(222) the inter planar distances d_{hkl} were was calculated using the Bragg equation 4.10. Then the lattice parameters c for the hcp Mg lattice and a for the fcc Pd lattice were calculated and the true lattice parameters c_0 and a_0 corrected for possible misalignment of the sample in the goniometer were obtained using the Cohen-Wagner plot.

The results of the Cohen-Wagner analysis calculated from eq. (4.11) are shown in figs. 5.27 and 5.28. One can see that the values of the Mg lattice parameter c_0 are very close to the literature value for bulk Mg (0.52108 nm) [48], the deviations are only in order of 0.001 nm and smaller. However although the deviations from the literature value are very weak there are apparently some common features for films deposited at same thermal conditions: (i) Thin Mg films deposited at RT or annealed exhibit very similar c_0 values independently on the substrate and these values are higher than the literature value. This testifies to the presence of bi-axial compression stress at the interface of the substrate and the film. (ii) Thin Mg films deposited at 300°C exhibit lower c_0 parameter than the literature value, which indicates bi-axial tensile stress at the film-substrate interface.

This can be explained by different thermal expansion coefficients of the film and the substrate. The film deposited at elevated temperature grow on a substrate with higher inter atomic distances, but when its cooled down to the RT the film as well as the substrate shrink. Since that the linear thermal expansion coefficient of Mg (8.2×10^{-6} K^{-1}) [48] is higher than those for Si (2.6×10^{-6} K^{-1}) [48], FS ($0.54 - 0.59 \times 10^{-6}$ K^{-1}) [49, 50] and sapphire ($5 - 6.6 \times 10^{-6}$ K^{-1}) [49] substrates the substrate shrinks less than bulk Mg would do. As a consequence the film suffers from a tensile stress. Deposition of the film at RT and subsequent annealing for 1 hour does not change the compression stress state, the film simply just expand and shrink.

Similar behavior as that for the thin films an be observed for the thick films as well. Since the thick films consist of generations of grains with different mean grain size as was discussed in section 5.2 and the stress situated in a vicinity of the film-substrate interface, the similarity of the films deposited at RT and the annealed films is weaker. This is most pronounced for films deposited on sapphire for which the misfit stress between the film and the substrate is strongest among the samples studied. The only sample exhibiting opposite behavior is the thick

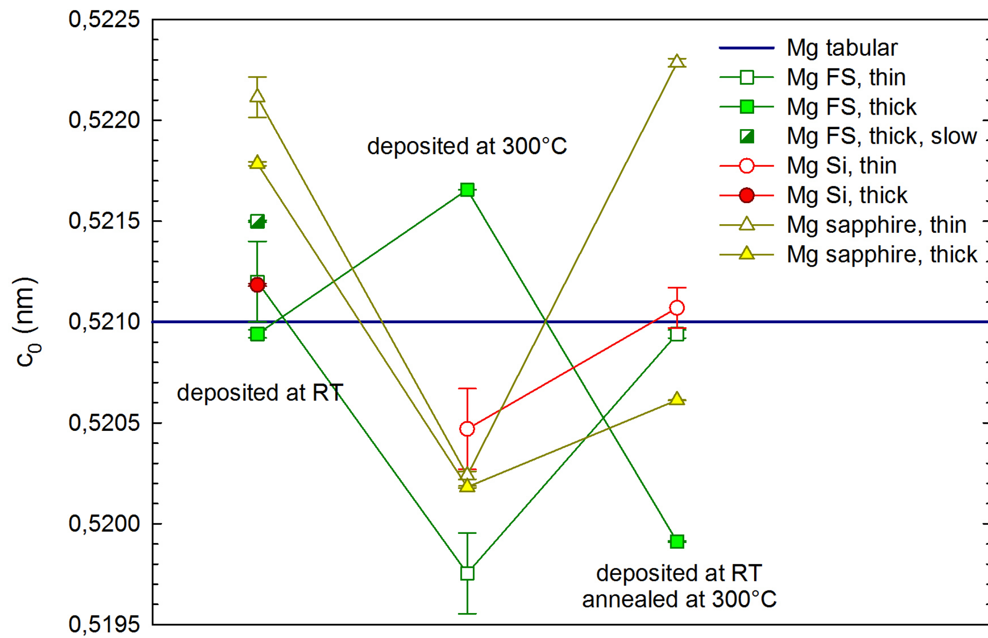

Figure 5.27: Lattice parameter c_0 for Mg films determined from the Cohen-Wagner plot.

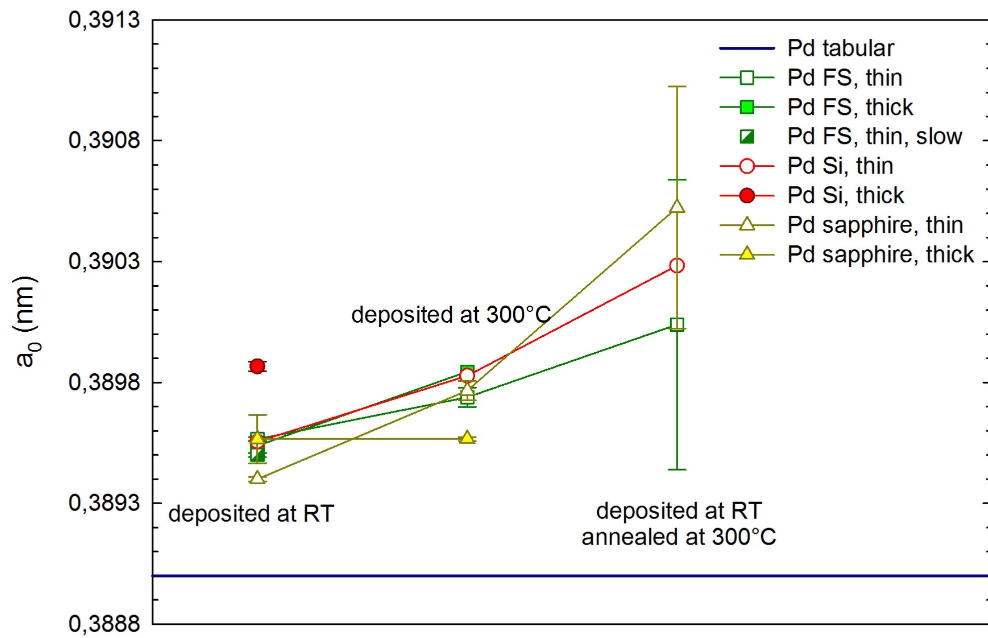

Figure 5.28: Lattice parameter a_0 for Pd over-layer determined from the Cohen-Wagner plot.

Mg film deposited at 300°C. We suppose this difference is caused by the fact that the thick film growing on the previous generation does not "sense" the substrate and the stress anymore, which allows it to have largest grains among the films studied (as was revealed by SEM) and thus it behaves more like films deposited at RT or annealed. However the thick film deposited at elevated temperature on sapphire exhibit "classical" tension stress since the stress for films on sapphire is more pronounced and does not vanish by thickness as easily as for film on amorphous FS.

Note that the Mg(004) peak cannot be resolved in the thin film deposited at RT on Si because of a very intensive Si(400) peak in its vicinity and therefore the lattice parameter c_0 could not be calculated for this film.

The values of lattice parameter a_0 for the Pd over-layer are practically the same, the differences among them are as low as 0.0005 nm or lower. However all Pd layers exhibit slightly higher parameter a_0 than the literature value (0.38907 nm) [48]. If we consider that the parameter a_0 was calculated from the Pd(111) planes parallel to the surface, the Pd layers are under compressive stress, which is the same for each Pd layer independently on the thermal treatment or the surface. Let us note the high error the of parameter a_0 for thin films deposited at RT and subsequently annealed is caused by a very weak Pd(222) reflection, so the error in determination of position of the peak was higher. In thick films deposited at RT and subsequently annealed the Mg-Pd phase was formed and both Pd(111) and Pd (222) reflections disappeared, so the Cohen-Wagner analysis of Pd layer cannot be performed.

5.3.3 Williamson-Hall analysis

From the position of 2θ and the fwhm of the Mg(002) and the Mg(004) peaks obtained from the peak-by-peak fitting of diffractograms in figs. 5.17 - 5.21 the Williamson-Hall plots were constructed.

CaF_2 powder was used as a standard for the estimation of the instrumental broadening. The obtained dependence of the fwhm of the CaF_2 peaks on the 2θ peak position was fitted by a 5th order polynomial. The Mg(002) and the Mg(004) peaks were then fitted as a convolution of a Pseudo-Voight diffraction profile and a Gaussian with fwhm given by interpolation of the instrumental broadening at the 2θ position of the Mg peaks.

However the Williamson-Hall analysis led to negative values of crystallite sizes. We supposed that this obviously wrong result is likely caused by using an inappropriate standard for instrumental broadening determination, i.e. the broadening of the peaks measured for CaF_2 powder was most probably higher than the instrumental broadening due to non-negligible microstrains in the CaF_2 powder. As a consequence the instrumental broadening determined using the CaF_2 powder was overestimated. Therefore the Williamson-Hall analysis was performed without instrumental broadening corrections and its results must be considered as qualitative only..

The inverse values of the final mean crystallite sizes D calculated from the Williamson-Hall analysis are plotted in fig. 5.29. One can see in the figure that the results can be divided into two groups. The crystallite size for the majority of thin films is around ~ 25 nm, however the statistical errors of $1/D$ are very

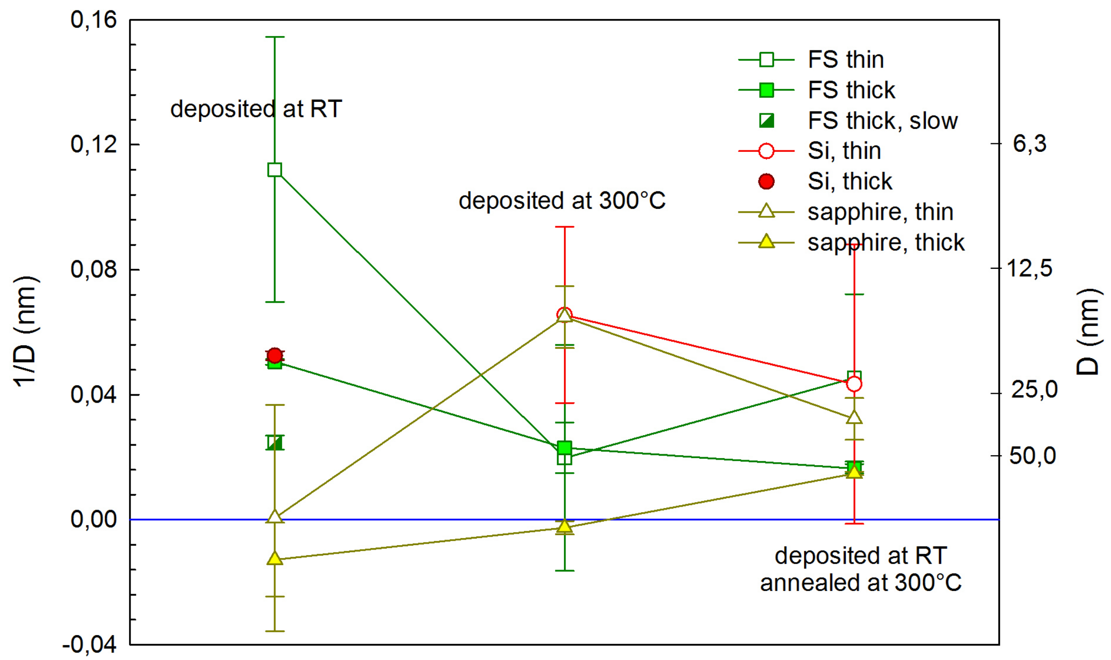

Figure 5.29: Inverse values of the mean crystallite sizes for the Mg films calculated from the Williamson-Hall plot, eq. (4.12).

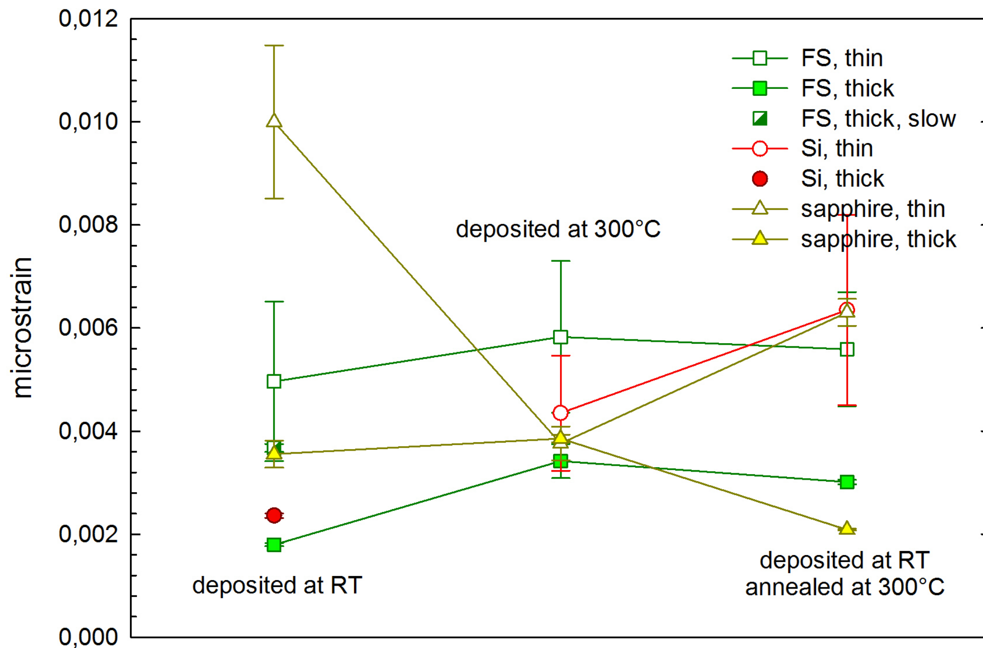

Figure 5.30: Values of microstrains present in the Mg films calculated from the Williamson-Hall plot, eq. (4.12).

large and significantly lowers the reliability of such results. The statistical errors of $1/D$ are caused by the uncertainty in the determination of the 2θ position and the fwhm because of limited statistics for the diffraction profiles measured on the thin films. The statistical errors of $1/D$ for the thick films are smaller since the thick films provide large signal and thus the intensity of diffraction peaks is higher. Hence the determination of the 2θ position and the fwhm of the diffraction peak is more precise. Unfortunately for the thick films the broadening of the diffraction profile due to the crystallite size is almost negligible, the values of $1/D$ are close to zero and thus the crystallites sizes are too large to be reliably determined. We emphasize that the results of Williamson-Hall plot were calculated from linear regression of two experimental points only.

Unlike the mean crystallite sizes the values of microstrains calculated from the slope of the Williamson-Hall plot provide more reliable information. From inspection of fig. 5.30 one can realize that the microstrain in the films deposited on FS and Si substrate practically does not depend on the thermal treatment. This fact agrees well with our picture that the Mg films on FS and Si substrate experience a very low misfit stress. The effect of thickness is visible in fig. 5.30 as well. Since the value of microstrain is determined by the average defect density (e.g. the density of misfit dislocations), the lower value of microstrain for the thick films proves that misfit dislocations are located close to the interface between the film and substrate.

The Mg films deposited on the sapphire substrate experience higher misfit stress due to the crystalline structure of the sapphire substrate which has large misfit with the Mg lattice. This is well pronounced in the fig. 5.30. The effect of the thickness of the Mg films deposited on sapphire is of the same nature as for the films deposited on FS and Si substrate. However one can see that the effect of different thermal treatment for the films deposited on the sapphire substrate is significantly more pronounced than for the films deposited on other substrates. The films deposited at RT exhibit higher values of microstrain than the films deposited on the substrate heated at 300°C. The annealing for 1 hour at 300°C lowers the microstrain however its value is still larger compared to the film deposited at 300°C. This behavior is agrees well with the SEM observations.

Note that the value of microstrain for the thick film deposited at 300°C is higher than expected. We suppose this is caused by the lower thickness of the film deposited at 300°C (~ 0.5 μm) than the thickness of the film deposited at RT and the annealed film (~ 1.5 μm). Since most of defects causing the microstrain are localized at the interface between the substrate and the film, their contribution to the thinner film (~ 0.5 μm) microstrain is higher than for the thicker films (~ 1.5 μm) which results in the higher total value of microstrain.

5.4 VEPAS results

The VEPAS measurements were performed on the thin Mg films deposited on FS and sapphire substrate and on the thick films deposited on sapphire and Mg substrate. From each DB annihilation profile measured by the single HPGe detector the S and W parameters were calculated using a bulk Mg reference. The values of the S and the W parameter were measured for the incident positron energies falling varied in the range from 0.27 eV to 35 keV.

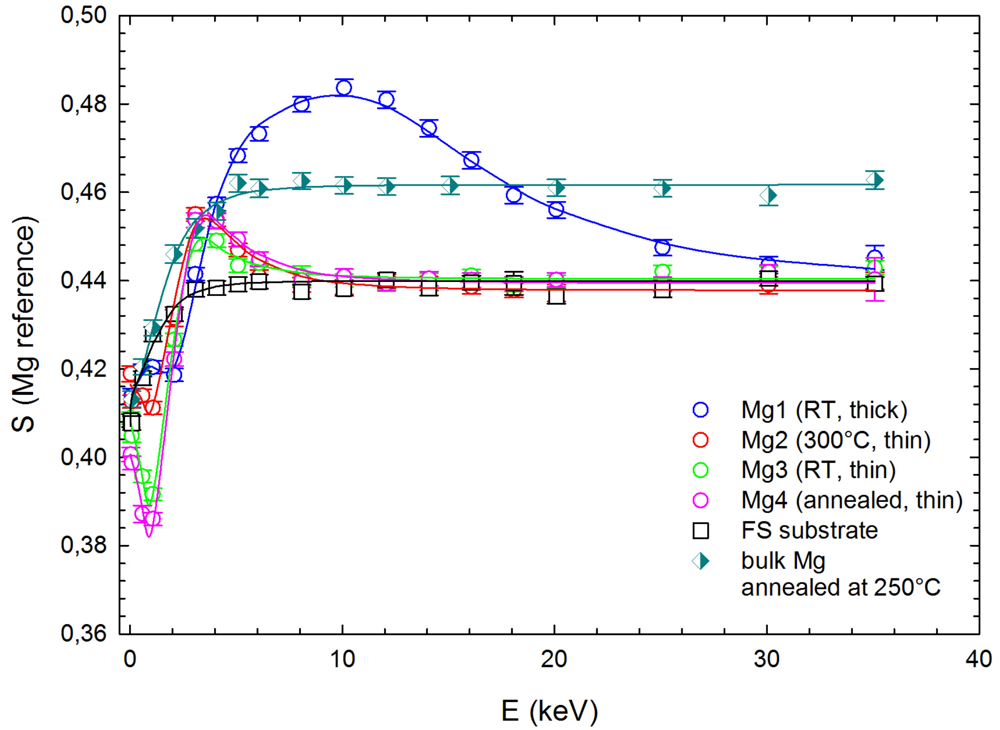

Figure 5.31: Dependence of the S parameter (points) for the thick Mg1 film and the thin Mg2-4 films deposited on FS substrate. $S(E)$ curves for the bare FS substrate and the bulk Mg annealed at 250°C are plotted in the figure as well. Solid lines are model functions calculated by the VEPFIT code.

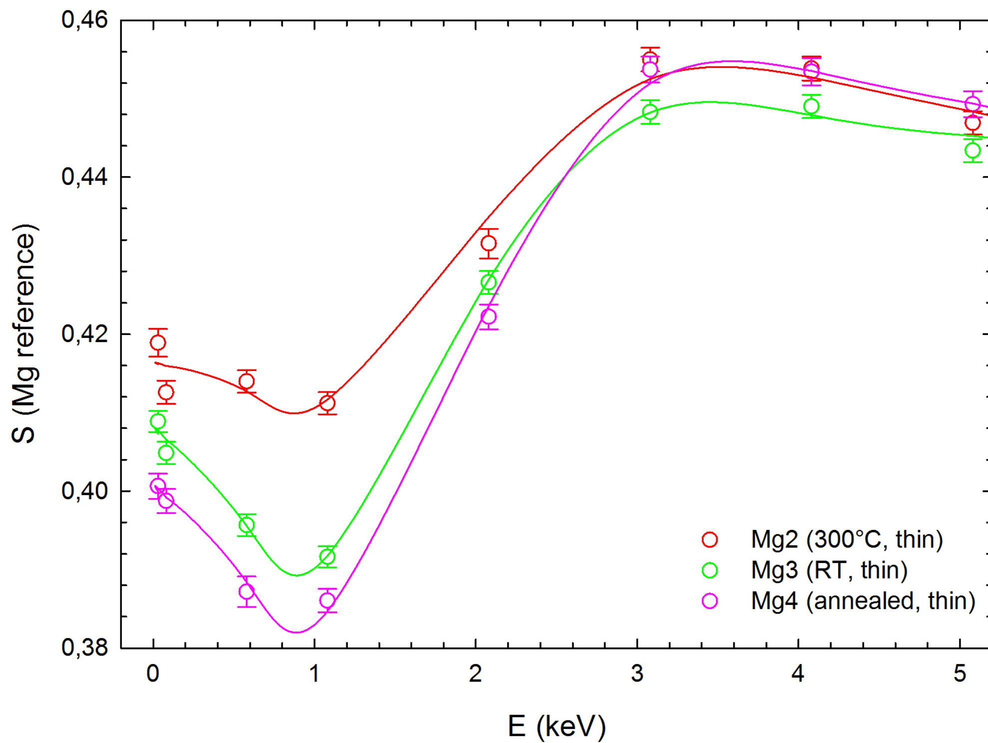

Figure 5.32: A detailed view of the dependence of the S parameter (points) for the low positron energies for the thin Mg2-4 films deposited on FS substrate. Solid lines are model functions calculated by the VEPFIT code.

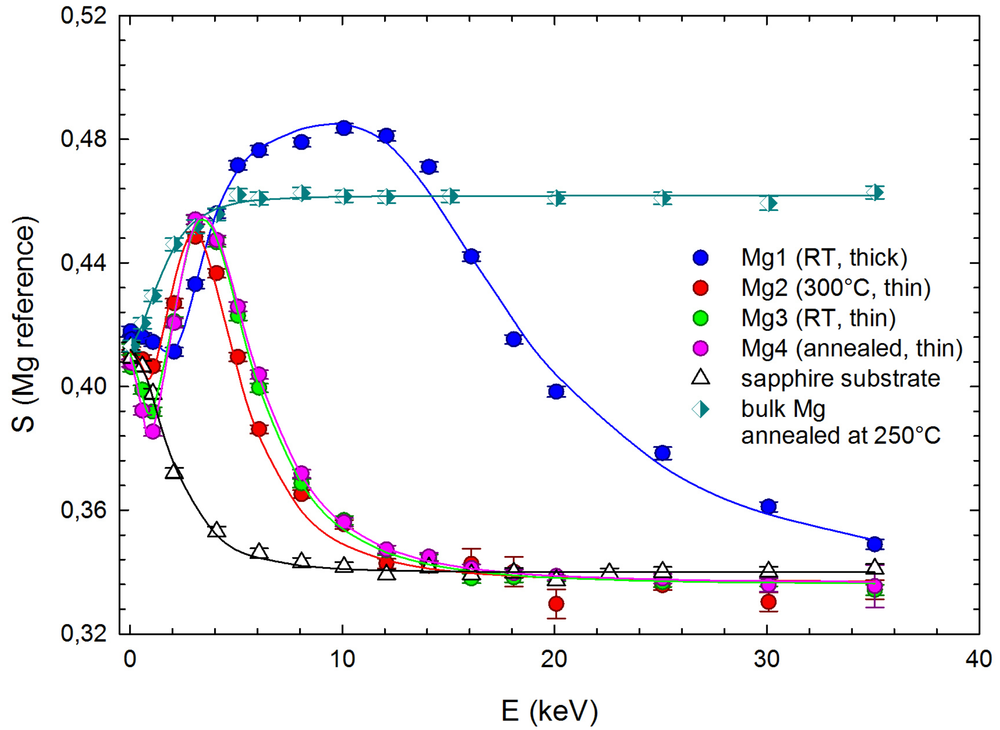

Figure 5.33: Dependence of the S parameter (points) for the thick Mg1 film and the thin Mg2-4 films deposited on sapphire substrate. $S(E)$ curves for the bare sapphire substrate and the bulk Mg annealed at 250°C are plotted in the figure as well. Solid lines are model functions calculated by the VEPFIT code.

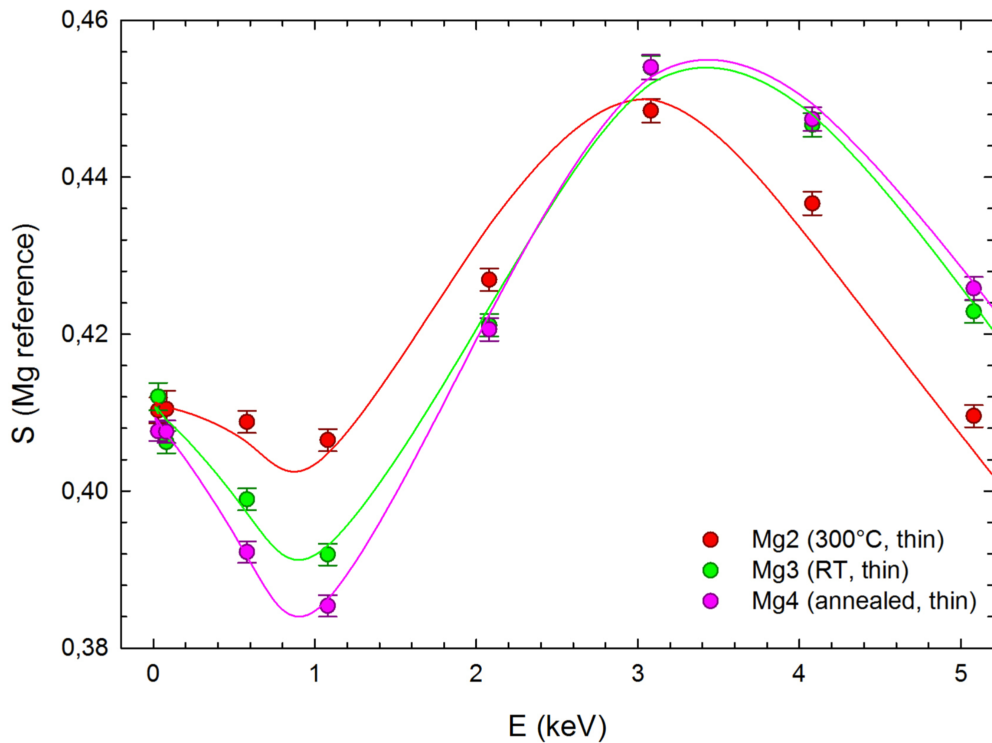

Figure 5.34: A detailed view of the dependence of the S parameter (points) for the low positron energies for the thin Mg2-4 films deposited on sapphire substrate. Solid lines are model functions calculated by the VEPFIT code.

5.4.1 S(E) curves and S-W plots

The dependences of the S parameter on the energy of incident positrons for the thick Mg1 and the thin Mg2-4 films deposited on FS and sapphire substrate are plotted in fig. 5.31 and 5.33 respectively. The $S(E)$ curves for the bare FS and sapphire substrate are plotted as well. In addition figs. 5.31 and 5.33 show also the $S(E)$ curve for a bulk Mg sample which was annealed at 250°C in an UHV chamber and covered by 20 nm Pd covering layer prior to its removal from the chamber in order to prevent oxidation of the Mg surface. The mean positron diffusion length $L_+ = 195(8)$ nm obtained from fitting of the $S(E)$ curve for the annealed bulk Mg agrees well with the value reported in [14].

Figs. 5.32 and 5.34 show a detailed view of the $S(E)$ curves for the low positron energies. For the lowest energies trapping and annihilation of positrons in the surface state dominates. Then for the energies up to 1 keV the $S(E)$ curves exhibit a drop of the S parameter due to positron annihilations in Pd cap. With increasing energy positrons penetrate into the Mg layer and thus the S parameter increases.

In the thick Mg1 films the S parameter becomes approximately constant in the range 8 - 12 keV, which indicates that practically all positrons annihilate inside the Mg film. One can see in figs. 5.31 and 5.33 that the S parameter for the thick film is higher than the S parameter measured in the reference annealed bulk Mg with a low concentration of defects. It indicates that the film contains defects which trap positrons. For the higher energies ($E > 12$ keV) positrons implanted into the Mg film become to penetrate into the substrate and annihilate either in the Mg layer or in the substrate. Since the bulk S parameter for the FS and the sapphire substrate is lower than the S parameter for the bulk Mg, the S parameter of the film decreases with the increasing energy and gradually approaches the bulk S parameter for the bare substrate.

In the thin Mg2-4 films the S parameter exhibits similar behaviour as the thick Mg1 films. However because of the lower thickness the S parameter for the thin films does not approach the constant value, corresponding to the situation when almost all positrons are annihilated in the Mg film, and instead becomes to drop and converges to the bulk S parameter for the bare substrate. At the positron energies 1 - 3 keV a positron implanted into the sample annihilates either inside the Pd cap or inside the Mg layer. For higher positron energies 4 - 10 keV positrons become to penetrate the substrate and thus annihilate in the Mg layer or in the substrate.

One can see in the detailed view of the $S(E)$ curves for the thin films in figs. 5.32 and 5.34 that the slope of the $S(E)$ curve for the film deposited at 300°C is significantly lower than the slope for the film deposited at RT and for the annealed film. This indicates that the positron diffusion length in the thin film deposited at 300°C is higher, i.e. the density of defects is lower compared to the thin films deposited at RT and the annealed thin films.

The dependences of the W parameter on the energy of incident positrons for the Mg1-4 films deposited on FS and sapphire substrate are shown in figs. 5.35 and 5.36. One can see that the W parameters behave oppositely compared to the S parameters and thus provide similar information. According to the $W(E)$ curve positrons implanted into the Mg films annihilate trapped in the surface state, then with increasing energy in the Pd layer, in the Mg film and finally in

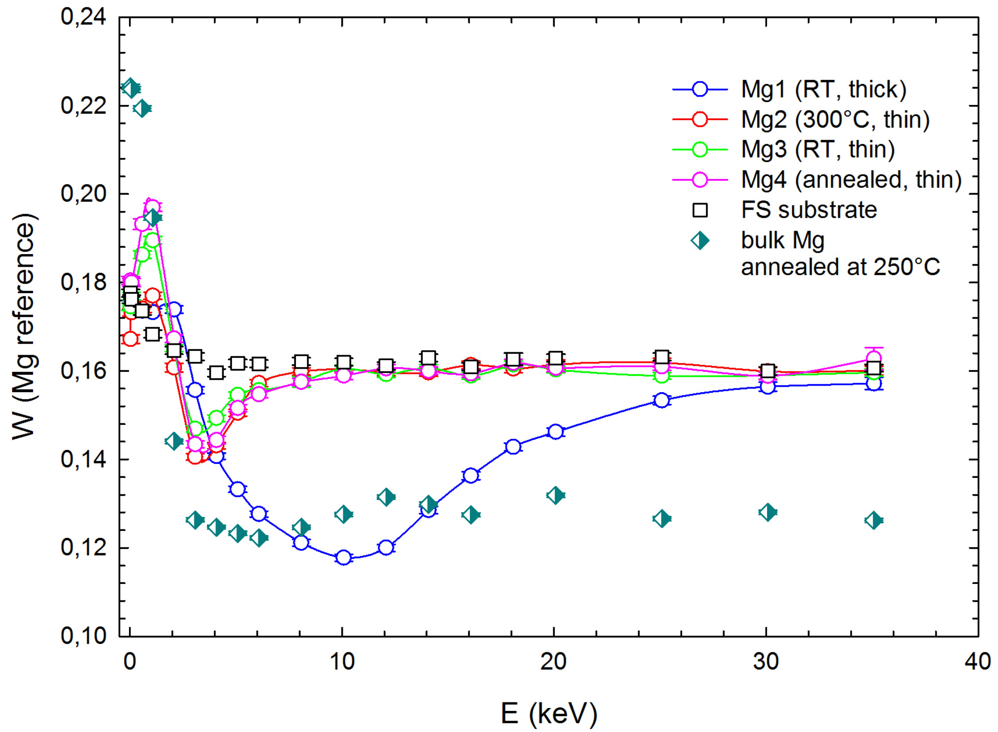

Figure 5.35: Dependence of the W parameter for the thick Mg1 film and the thin Mg2-4 films deposited on FS substrate. $W(E)$ curves for the bare FS substrate and the bulk Mg annealed at 250°C are plotted in the figure as well.

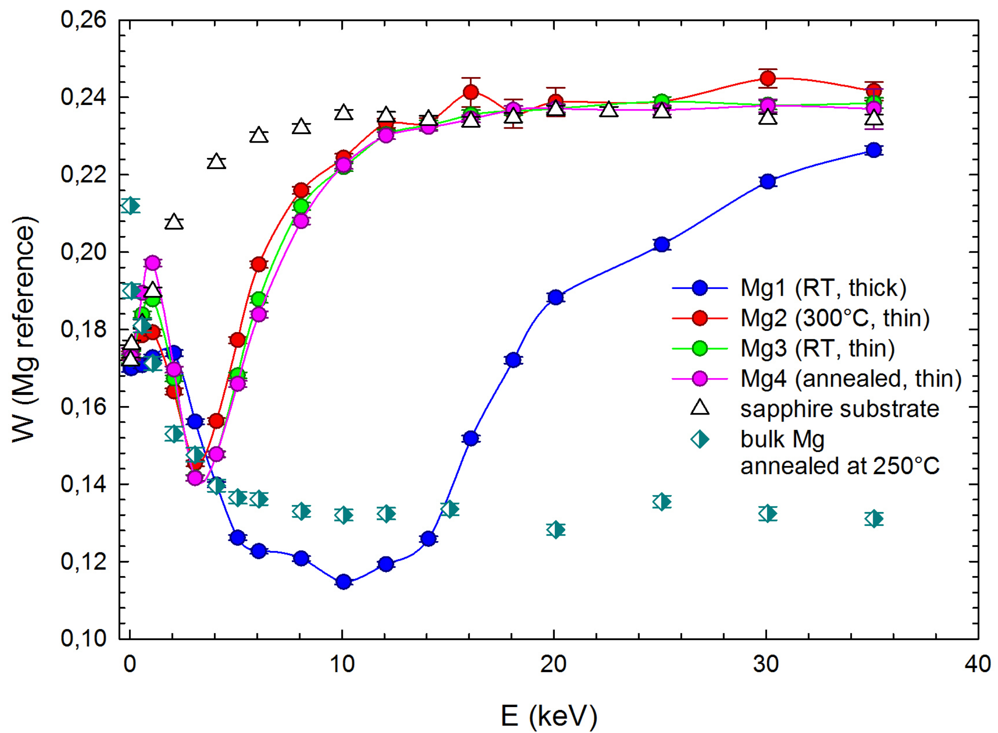

Figure 5.36: Dependence of the W parameter for the thick Mg1 film and the thin Mg2-4 films deposited on sapphire substrate. $W(E)$ curves for the bare sapphire substrate and the bulk Mg annealed at 250°C are plotted in the figure as well.

the substrate. Also the W parameters for the thick films are lower than the W parameter for the annealed bulk Mg, which indicates higher density of defects in the film. The positron diffusion lengths for the thin films can be estimated from the slopes of the $W(E)$ curves as well. The thin film deposited at the elevated temperature exhibits higher diffusion length and thus lower density of defects. As was mentioned the $W(E)$ curves carry out similar information as the $S(E)$ curves. However the statistical uncertainty of the W parameter values is higher since the W parameter is determined from the high momentum part of DB spectrum which exhibits lower signal to background ratio than the low momentum part characterized by the S parameter. Hence it is more reasonable to characterize the studied film with the S values rather than using the W parameter.

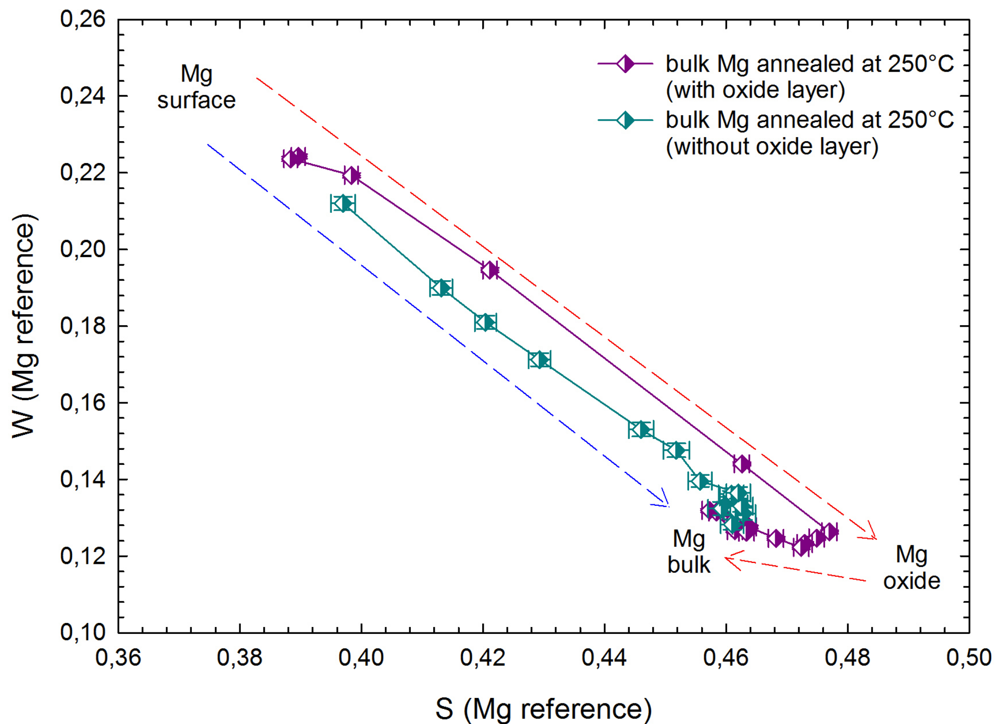

Figure 5.37: S-W plot for the two reference bulk Mg samples annealed at 250°C with and without a native oxide layer on their surface.

The fact the S and the W parameters are not independent can be well illustrated by the so-called S-W plot. The information it provides is illustrated by an example in fig. 5.37 which shows S-W plots for the reference bulk Mg annealed at 250°C. One sample contains a thin oxide layer formed at the surface on air. Surface of the second sample was etched in 3% HNO3 directly before insertion into chamber and the native oxide layer was not formed. One can see that for the sample without the oxide layer the S-W data lie on a straight line connecting the point for the surface state with the point for bulk Mg. At low energies almost all positrons are annihilated in the surface state. With increasing energy positrons penetrate deeper and deeper into the sample and the fraction of positrons diffusing back to the surface decreases. Finally for $E > 10$ keV virtually all positrons annihilate in Mg bulk. The decreasing fraction of positrons diffusing back to the surface is reflected by increase of S and decrease of W from the point corresponding to the surface to the point for Mg bulk. Similarly for

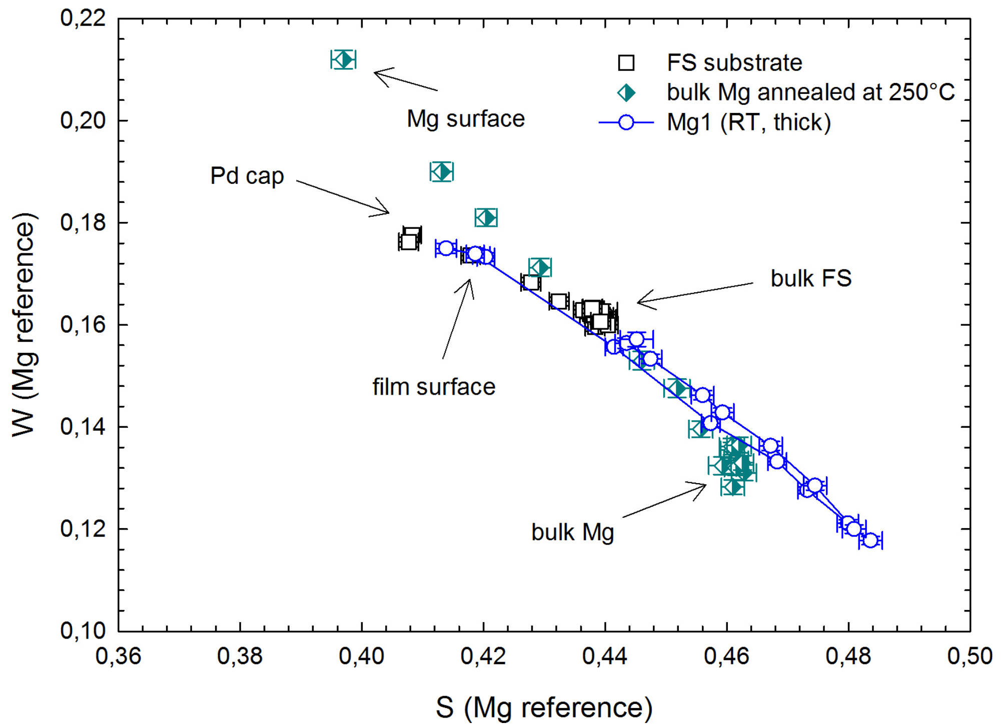

Figure 5.38: S-W plot for the thick Mg1 film deposited on FS substrate. The S-W data a the bare FS substrate and the bulk Mg annealed at 250°C are plotted in the figure as well.

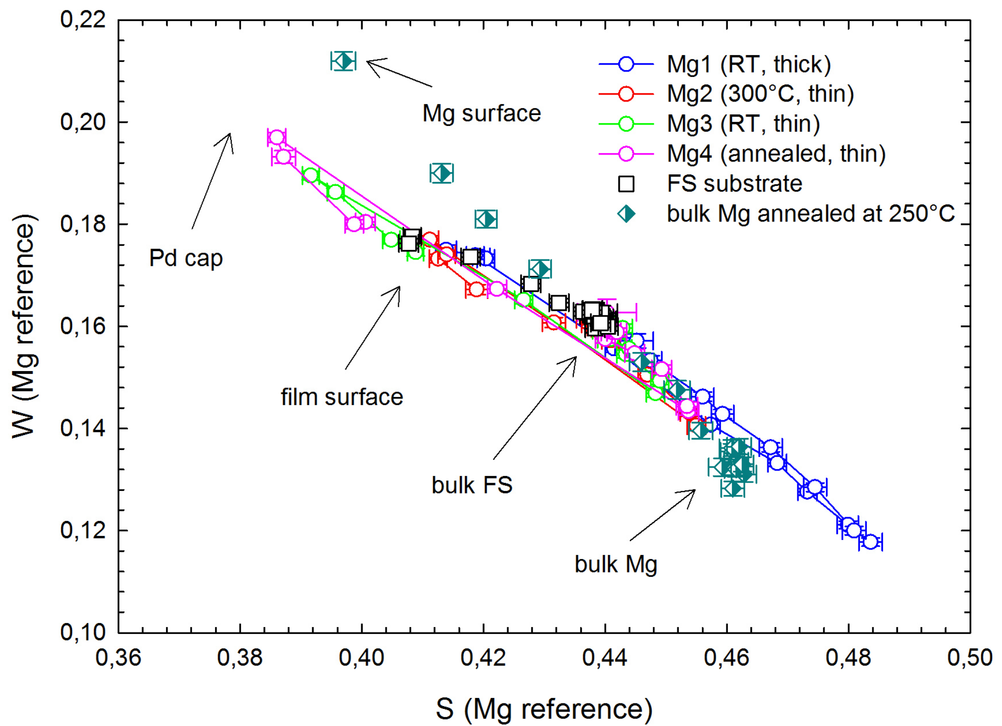

Figure 5.39: S-W plot for the Mg1-4 films deposited on FS substrate. The S-W data for a bare FS substrate and the bulk Mg annealed at 250°C are plotted in the figure as well.

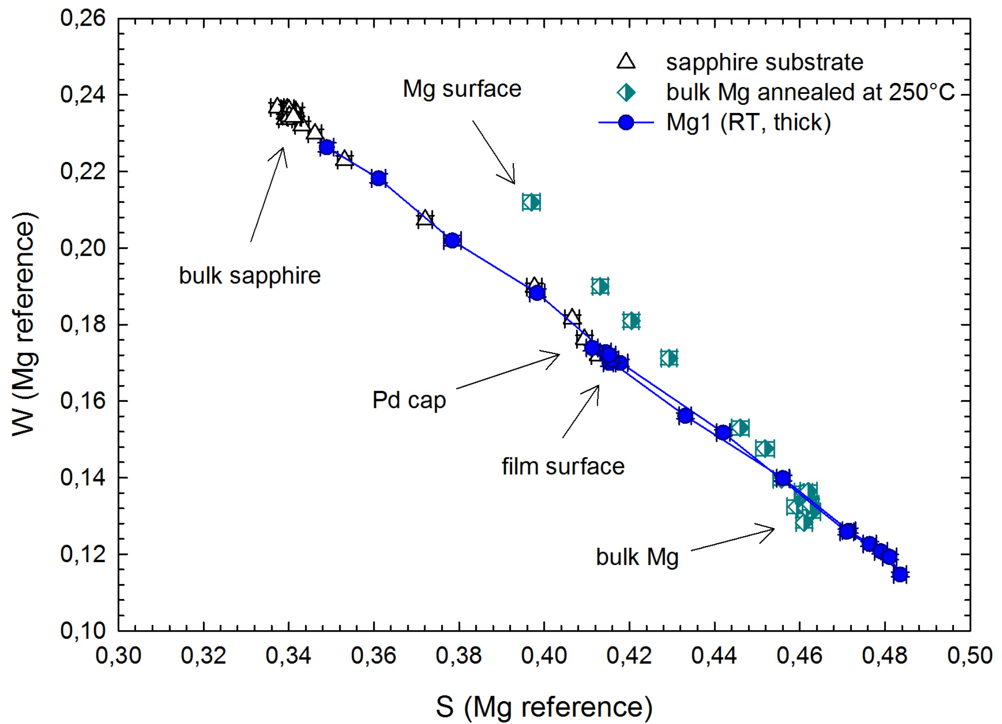

Figure 5.40: S-W plot for the thick Mg1 film deposited on sapphire substrate. The S-W data for a bare sapphire substrate and the bulk Mg annealed at 250°C are plotted in the figure as well.

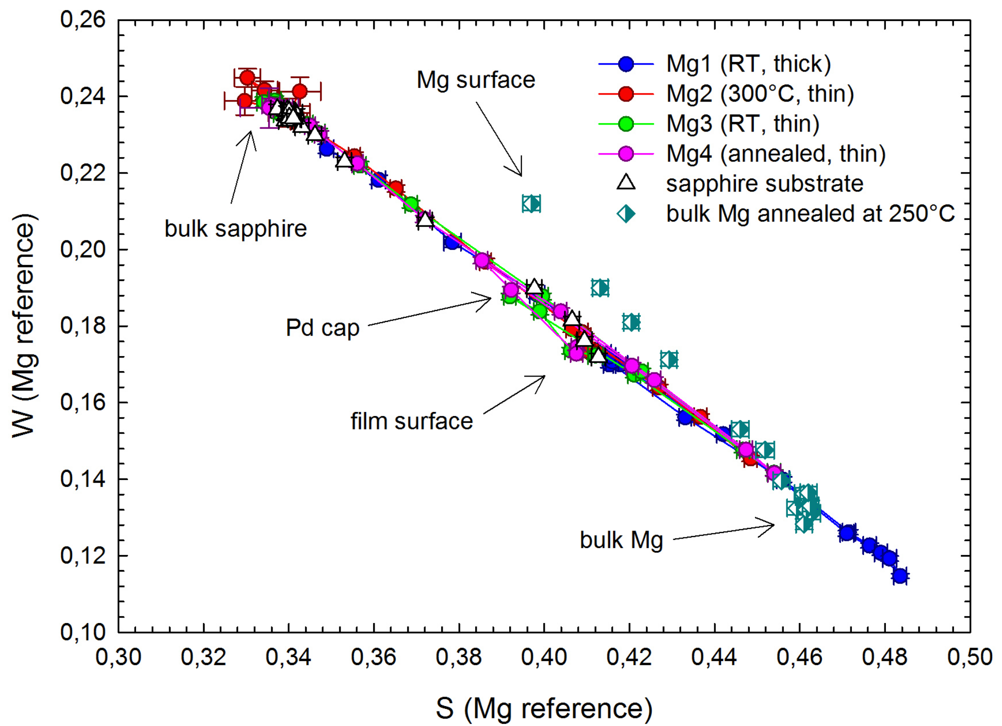

Figure 5.41: S-W plot for the Mg1-4 films deposited on sapphire substrate. The S-W data for a bare sapphire substrate and the bulk Mg annealed at 250°C are plotted in the figure as well.

the sample with the oxide layer positrons with very low energies annihilate at the surface. With increasing energy positrons start to penetrate into the oxide and finally into the Mg bulk when the positron energy is further increased. Note that since the oxide layer is very thin there is always inter-diffusion of positron between the oxide layer and the surface as well as between the oxide layer and the Mg bulk and positrons are never annihilated exclusively in the oxide layer.

Similarly the S-W plots for the Mg1-4 films can be created. Figs. 5.39 and 5.41 present S-W plots for the thick Mg1 film deposited on FS and sapphire substrate, respectively. One can that with increasing energy see positrons gradually annihilate in the surface state, in the Pd cap, in the Mg film and in the substrate as has been described in the previous text. Here all data fall approximately on a straight line.

The S-W plots for the all Mg1-4 film deposited on the FS and the sapphire substrate are plotted in figs. 5.39 and 5.41. One can see the behavior of the S-W data for the thin Mg2-4 films is very similar to that for the thick Mg1 film both for the FS and the sapphire substrate.

The dependences of the S parameter on the energy of incident positrons were measured for the thick films as well. Figs. 5.42 and 5.43 show the $S(E)$ curves for the thick films deposited on Mg (Mg5 and Mg6 film) and sapphire substrate (Mg1, Mg5, Mg7 and Mg8). The $S(E)$ curves for the annealed bulk Mg and the bare sapphire substrate are included in the figures as well.

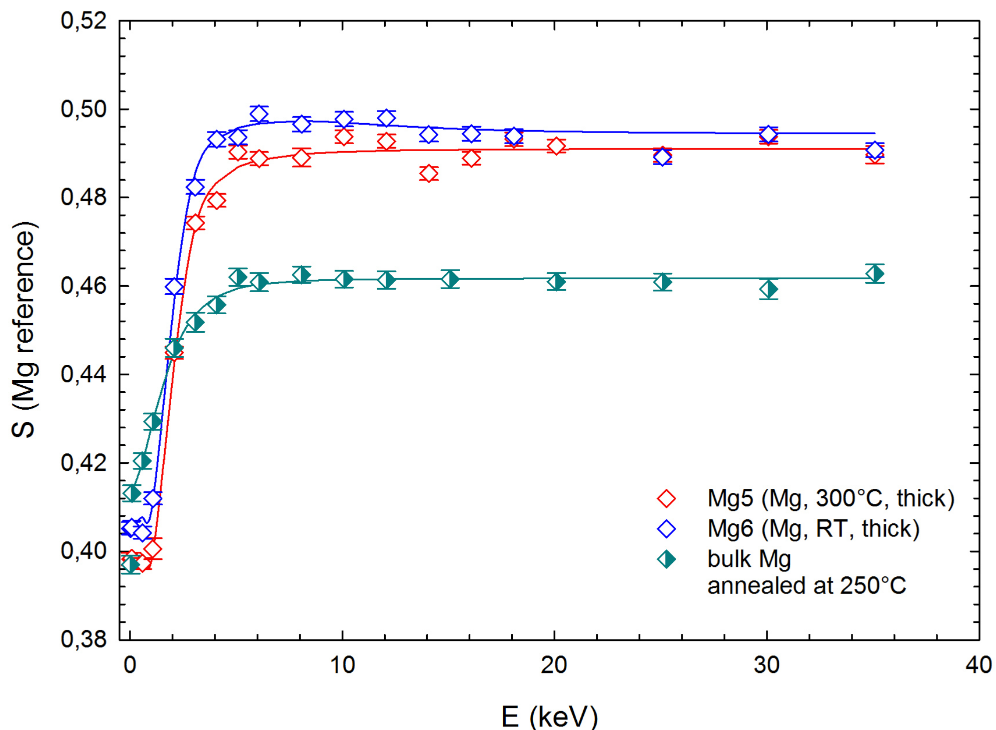

Figure 5.42: Dependence of the S parameter (points) for the thick Mg5 and Mg6 films deposited on Mg substrate. $S(E)$ curve for the bulk Mg annealed at 250°C is plotted in the figure as well. Solid lines are model functions calculated by the VEPFIT code.

One can see in fig. 5.44 that for the low energies the $S(E)$ curves for the thick films (except of Mg7 film) exhibit the same behavior as the thin films since

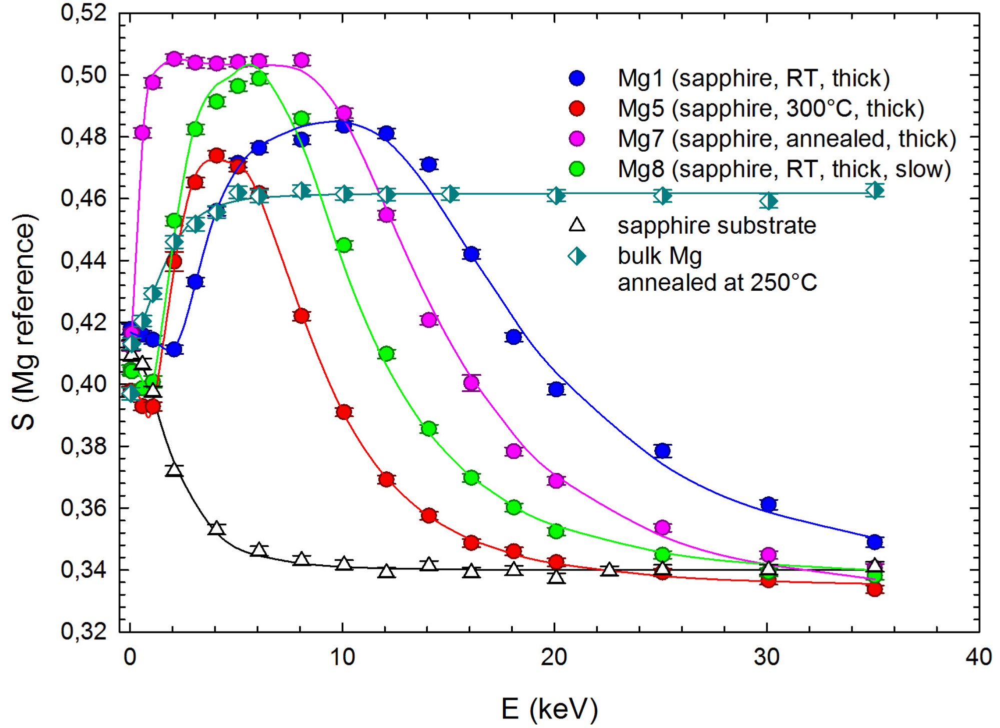

Figure 5.43: Dependence of the S parameter (points) for the thick Mg1, Mg5, Mg7 and Mg8 films deposited on sapphire substrate. $S(E)$ curves for the bare sapphire substrate and the bulk Mg annealed at 250°C are plotted in the figure as well. Solid lines are model functions calculated by the VEPFIT code.

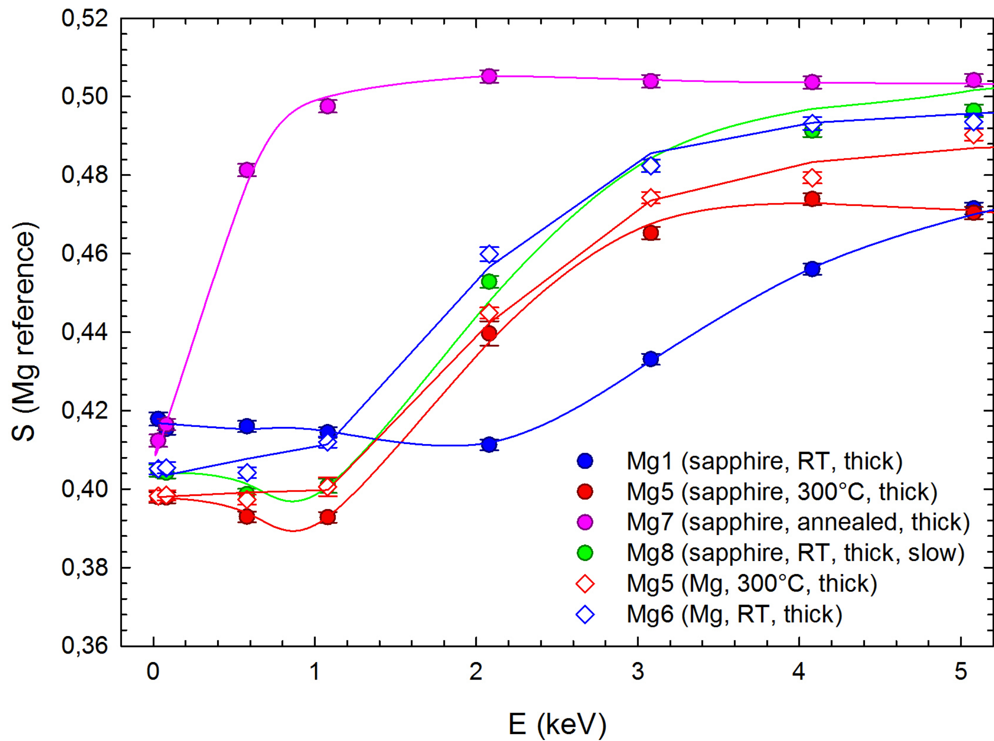

Figure 5.44: A detailed view of the dependence of the S parameter (points) at low positron energies for the thick Mg films deposited on Mg and sapphire substrate. Solid lines are model functions calculated by the VEPFIT code.

positrons annihilate either at the surface or in the Pd cap, which was deposited at the same conditions for each Mg film. The annihilation in the Pd cap obviously does not occur for the Mg7 film since Pd was mixed with Mg and the Mg-Pd phase was formed in a sub-surface region. At the low positron energies the $S(E)$ curve for the thick Mg1 film seems to be different from the other thick films (Mg5 and Mg8). The local minimum of the S parameter occurs at the positron energy of 2 keV instead of 1 keV typical for the thick Mg5 and Mg8 as well as for the thin films Mg2-4 (see figs. 5.32 and 5.34). This indicates that the Pd cap was in case of the Mg1 film thicker than expected. Therefore for the positron energy of 2 keV the annihilation in Pd cap still dominates and positrons become to penetrate into Mg layer at higher energies. This irregularity in the Pd cap thickness might be caused by the fluctuation of the plasma discharge during the magnetron sputtering when more Pd atoms from the target could have been sputtered out and deposited on the Mg film.

For the films deposited on Mg substrate it is hard to resolve the S parameter for the Mg film and for the Mg substrate. However one can see in fig. 5.42 that the $S(E)$ curves are enhanced at the positron energies in the range 4 - 14 keV compared to the S parameter values at the high energies ($E > 14$ keV), where positrons penetrate into the Mg substrate. S parameters for the film deposited at RT are higher than those for the film deposited at 300°C. This indicates that the film deposited at 300°C exhibits lower density of defects than the film deposited at RT.

The S parameter for the Mg substrate is higher than that for the reference defect-free bulk Mg. Although both samples were annealed at similar conditions the Mg that we used as a substrate exhibits apparently higher defect density. The annealing at 300°C for 1 hour may not completely remove all defects present from the material. Moreover the bombardment by the Ar ions during pre-sputtering of the Mg substrate and by the Mg atoms during deposition (impacting energy ~ 100 eV) could introduce defects into the Mg substrate as well.

One can see in fig. 5.43 the effect of different thicknesses of the thick films deposited on sapphire. Positrons implanted into the Mg5 (thickness of 0.56 μm) and Mg8 film (thickness of 0.85 μm) become to penetrate into sapphire substrate for the lower energies than for the thicker Mg1 and Mg7 films (both 1.5 μm thick). Despite the same thickness the annihilation of positrons implanted into Mg1 film still occurs at higher positron energies than for the Mg7 film. This is obviously caused by the lower positron diffusion length in Mg7 film. Moreover the diffusion length of the sapphire substrate for the Mg1 films appears to be higher than for the other thick films. This phenomenon will be discussed later.

The film deposited at 300°C exhibits the lowest S parameter among the films studied indicating the lowest density of defects. The film deposited at RT with the high deposition rate exhibits lower S parameter that the film deposited with slow deposition rate and thus the slow deposition rate leads to higher density of defects than the fast deposition rate. The film deposited at RT and subsequently annealed at 300°C exhibits the highest S parameter among the films studied.

In fig. 5.44 one can see a detailed view of the slopes of the $S(E)$ curves which define the positron diffusion lengths in the Mg films. The $S(E)$ curve for the film Mg8 deposited at RT (slow deposition rate) exhibits the lowest positron diffusion length. The highest positron diffusion length exhibit the film Mg5 deposited at

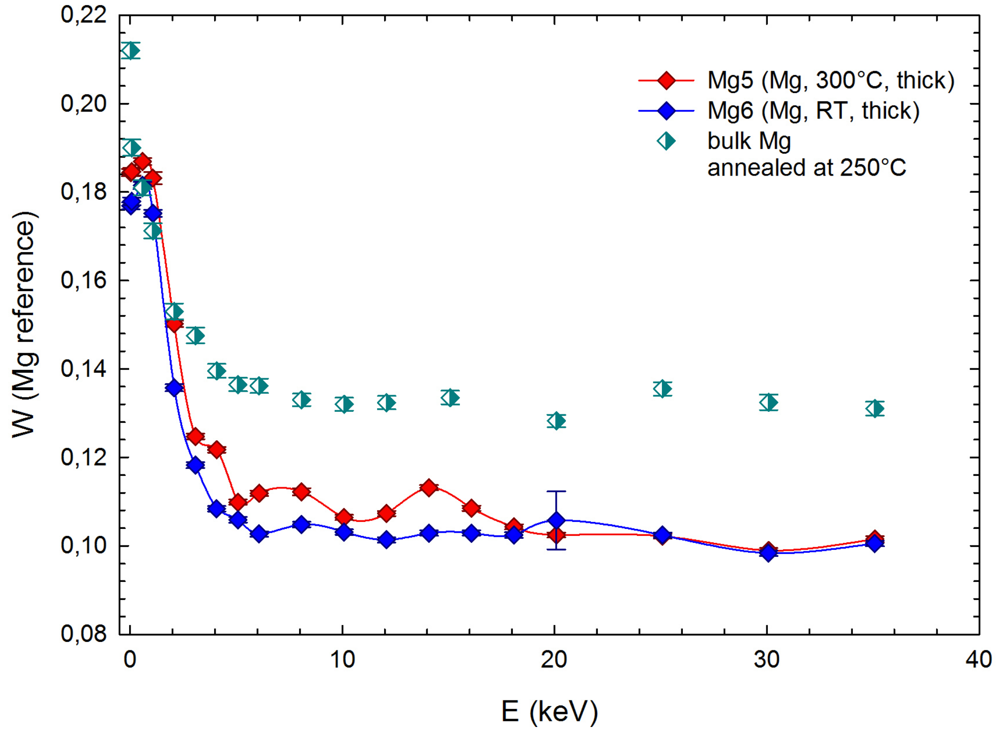

Figure 5.45: Dependence of the W parameter for the thick Mg5 and Mg6 film deposited on Mg substrate. $W(E)$ curve for the bulk Mg annealed at 250°C is plotted in the figure as well.

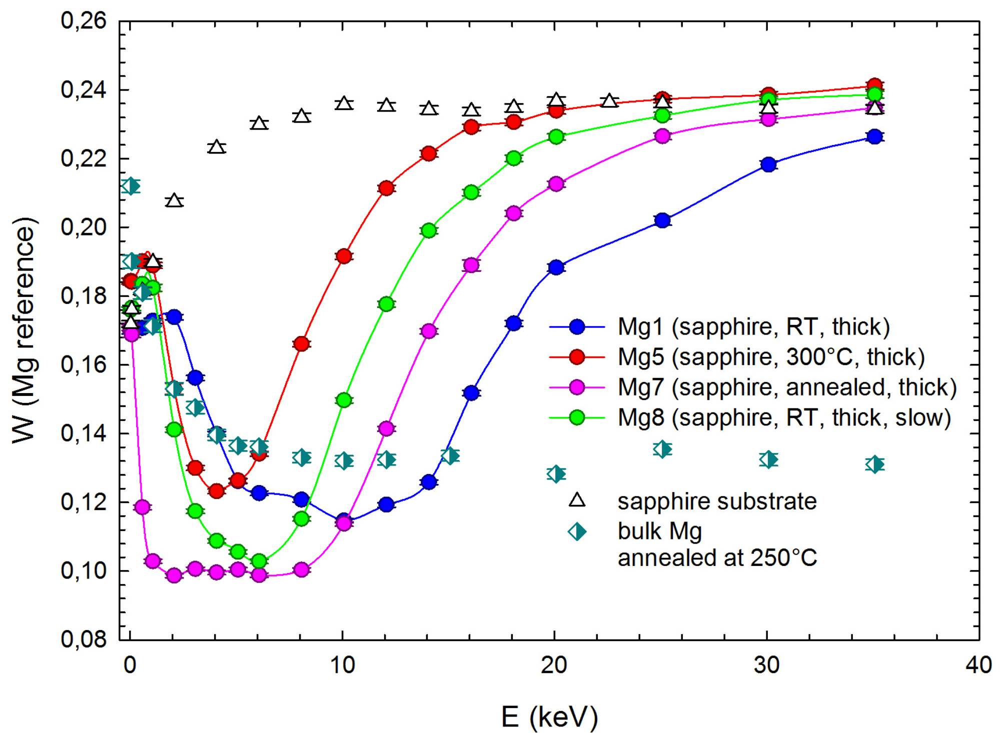

Figure 5.46: Dependence of the W parameter (points) for the thick Mg1, Mg5, Mg7 and Mg8 films deposited on sapphire substrate. $W(E)$ curves for the bare sapphire substrate and the bulk Mg annealed at 250°C are plotted in the figure as well.

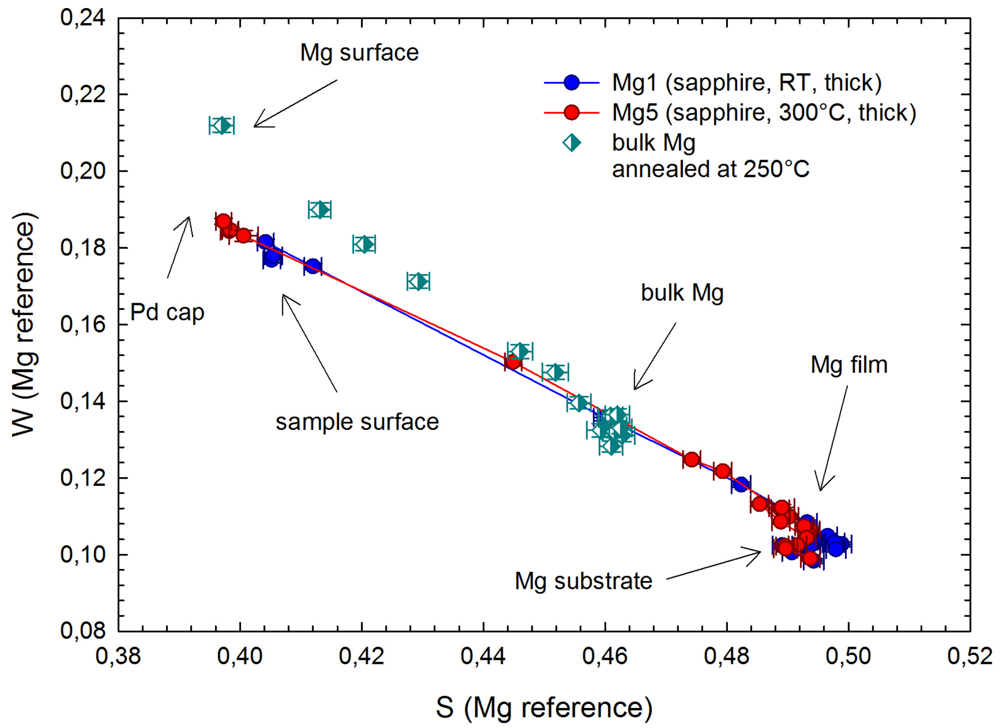

Figure 5.47: S-W plot for the thick films deposited on Mg substrate. The S-W data for the bulk Mg annealed at 250°C are plotted in the figure as well.

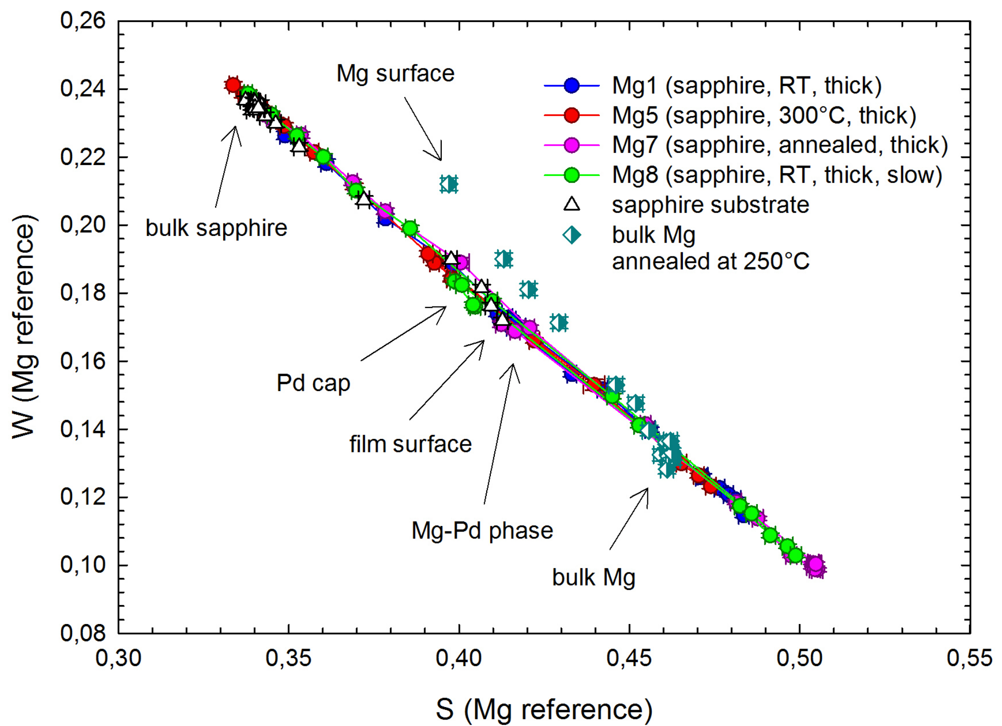

Figure 5.48: S-W plot for the thick films deposited on and sapphire substrate. The S-W data for the bare sapphire substrate and the bulk Mg annealed at 250°C are plotted in the figure as well.

300°C. These observations agrees with the observation of the S parameters for the Mg films.

The dependences of the W parameter on the energy of incident positron for the thick films deposited on Mg and sapphire substrate are shown in figs. 5.45 and 5.46. The $W(E)$ curves exhibit opposite behavior than the $S(E)$ curves. The annihilation in the Pd cap and in the Mg-Pd phase respectively, the effect of thickness, different thermal treatment is the same as was reported for the $S(E)$ curves, but into the opposite direction. One can see that the W parameters and the positron diffusion lengths for the Mg films agrees well with the results for the $S(E)$ curves.

The S-W plot for the films deposited on Mg exhibit similar behavior as was described for the thin films. With increasing energy positrons annihilate at the surface, then in the Pd cap, subsequently in the Mg film and finally at the Mg substrate. The higher S parameter for the Mg film compared to the S parameter of the Mg substrate is clearly visible. However the S parameter for the Mg film as well as for the Mg substrate is significantly higher than the S parameter for the defect-free Mg sample.

Both in the S-W plots for the thick and the thin Mg films deposited on sapphire, shown in figs. 5.48 and 5.41, include S-W data for the thick Mg1 film deposited at RT (single S-W plot of the Mg1 film is shown in fig. 5.40). One can see that the S-W plots for the thick and the thin films are practically the same. Again with increasing energy of incident positrons the annihilation occurs gradually at the surface, inside the Pd cap (for Mg7 film inside the Mg-Pd phase), inside the Mg film and eventually inside the sapphire substrate.

5.4.2 Results of VEPFIT analysis

The $S(E)$ curves for Mg films were fitted by the VEPFIT code assuming three layers: (i) Pd cap with thickness of 22 nm, (ii) Mg film with with thickness t_{PROFIL} determined by profilometry (see tab. 5.3) and (iii) semi-infinite substrate. Besides the density and the thickness each layer is characterized by its S parameter and the positron diffusion length L_+. In order to reduce the number of fitted parameters S and L_+ for the substrates were fixed at the values obtained for the bare substrates. The thickness and the positron diffusion length for the Pd over-layer was fixed at 22 nm and 10 nm respectively.

The S(E) curves for Mg films, bare substrates and the bulk Mg reference calculated by the VEPFIT code are plotted in figs. 5.31 - 5.34 and 5.42 - 5.44 by solid lines and are obviously in a good agreement with the experimental points. The positron diffusion length L_+ and the S parameter for the Mg films which were obtained from the fitting are listed in tab. 5.6 and graphically shown in figs. 5.49 and 5.50. Tab. 5.6 shows also Mg film thicknesses t_{VEPAS} used in the fitting procedure. The S and L_+ for the bare sapphire and the FS substrate and for the bulk Mg reference are listed in tab. 5.6 as well.

All Mg films studied exhibit shorter L_+ and higher S than the well annealed bulk Mg reference. This testifies that all Mg films contain open volume defects which trap positrons. These defects are misfit dislocations necessary for accommodation of the lattice mismatch between the film and the substrate and open volume point defects localized in the vicinity of grain boundaries, which were

identified by LT measurement on a pulsed low-energy positron beam [17].

sample	t_{PROFIL} (nm)	t_{VEPAS} (nm)	Substrate	S (Mg ref.)	L_+ (nm)
Mg1	1540(20)	2420(10)	sapphire	0.4878(4)	45(2)
		2210(30)	FS	0.4843(4)	46(1)
Mg2	156(8)	177(F)	sapphire	0.483(2)	60(5)
		177(F)	FS	0.480(2)	77(7)
Mg3	121(1)	142(F)	sapphire	0.485(2)	35(4)
		142(F)	FS	0.478(2)	39(5)
Mg4	125(3)	144(F)	sapphire	0.483(2)	50(5)
		144(F)	FS	0.482(2)	52(6)
Mg5	557(7)	557(F)	sapphire	0.4718(7)	50(5)
		557(F)	w.a. Mg	0.4903(6)	13(5)
Mg6	1100(20)	1100(F)	w.a. Mg	0.4979(4)	3(2)
Mg7	1500(30)	1500(F)	sapphire	0.5030(4)	1.0(5)
Mg8	848(8)	848(F)	sapphire	0.5067(5)	0.5(3)
substrate		semi-inf.	bulk Mg	0.4634(5)	196(9)
substrate		semi-inf.	sapphire	0.3400(2)	46(5)
substrate		semi-inf.	FS	0.4367(3)	24(1)

Table 5.6: Results of the fitting by VEPFIT code for the Mg films, the reference well annealed bulk Mg and the bare FS and sapphire substrates. The S and L_+ for the semi-infinite substrates were fixed during the fitting procedure. The thickness and the positron diffusion length of the Pd layer was fixed at 22 nm and 10 nm respectively. The values of the Mg film thicknesses t_{VEPAS} used in the fitting procedures are included (F = fixed parameter).

From inspection of figs. 5.49 and 5.50 one can realize that the films deposited at 300°C exhibit always higher positron diffusion length and lower S parameter than the films deposited at RT. This is caused by the lower density of misfit dislocations and increased mean grain size leading to a drop of the volume fraction of grain boundaries containing open volume defects. Taking into the account the statistical uncertainties the annealing of the thin films slightly increases the positron diffusion length while the S parameter remains unchanged.

This testifies that the annealing slightly lowers the density of defects presented in material more likely due the grain coarsening, as was showed by SEM. On the other hand annealing has only very small impact on the misfit dislocations, as the Williamson-Hall results indicated. However one can see in figs. 5.49 and 5.50 that the film Mg7 exhibits significantly increased density of defects. This is likely caused by the formation of the Mg-Pd phase in the sub-surface region. As was revealed by the XRD measurement the Pd atoms diffuse into the Mg grains and form Mg-Pd phase. The Mg-Pd phase formed in this sample may contain structural vacancies which leads to a significant enhancement of defect density.

The deposition at RT with the slow deposition rate introduces large amount of open volume defects into the film, which leads to the highest value of S and the lowest value of L_+ among all the Mg films studied. We suppose that this effect is caused by finer grain structure and also higher density of misfit dislocations. Because of the slow deposition rate the Mg atoms have longer time to take over the equilibrium lattice site which results in more pronounced interaction between

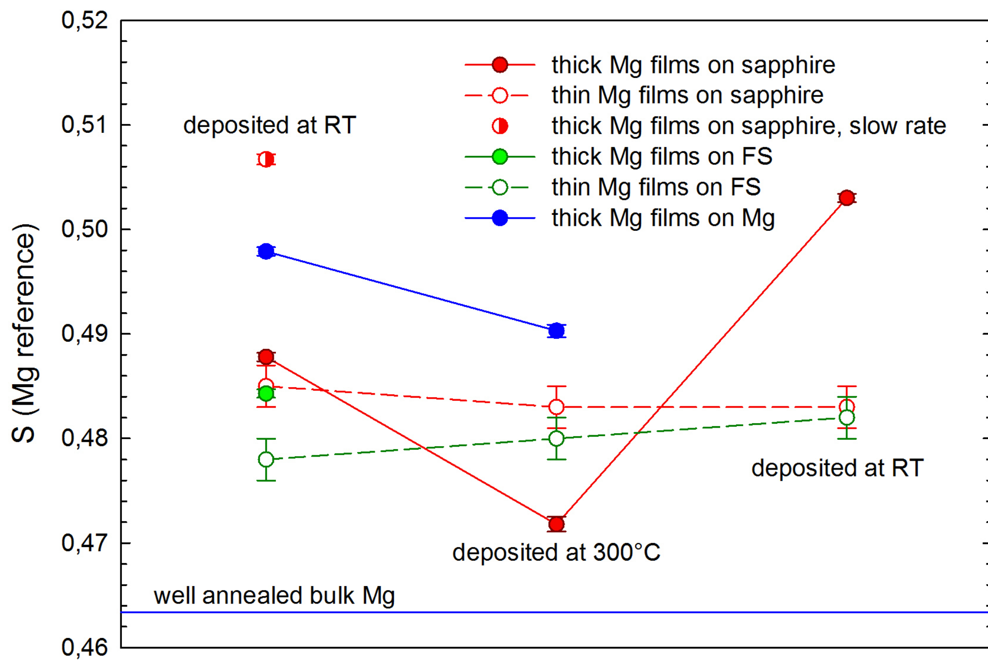

Figure 5.49: S parameters of the Mg films obtained by fitting of the $S(E)$ curves by the VEPFIT code.

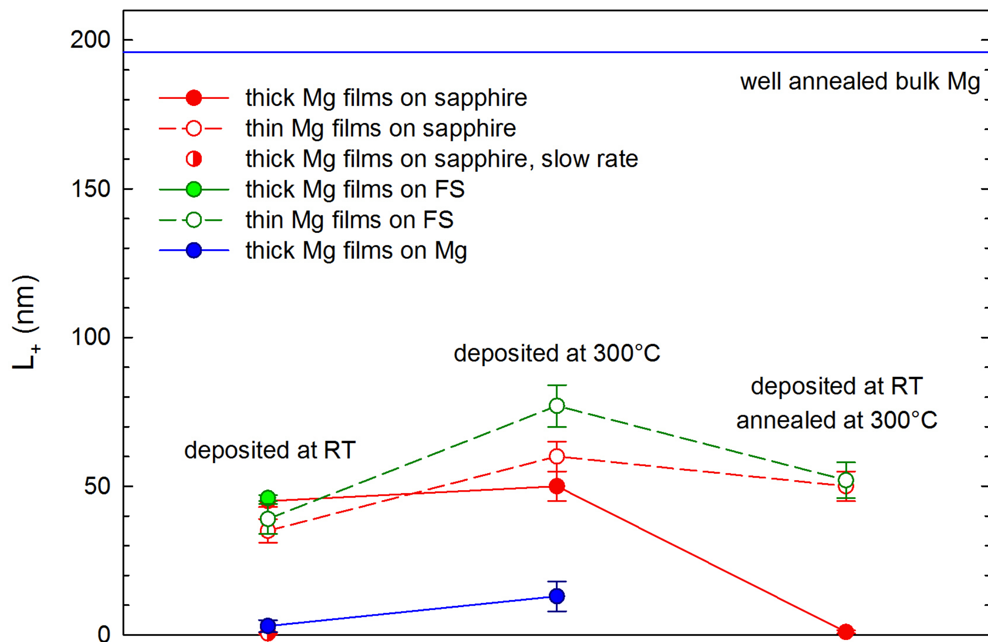

Figure 5.50: Positron diffusion lengths L_+ of the Mg films obtained by fitting of the $S(E)$ curves by the VEPFIT code.

the film and the substrate atoms. The Mg film literally "feel" the substrate structure beneath, i.e. the high density of misfit dislocations must be created to release the stress between the film and the substrate. Moreover since the mobility of Mg atoms is higher, more open volume defects in a vicinity of grain boundaries can be formed.

As was determined by the SEM observations and the XRD measurement the stress between the Mg film and the sapphire substrate is larger than for the films deposited on the FS substrate. The Mg films deposited on sapphire exhibit also smaller grains compared to the Mg films deposited on the FS substrate and therefore the volume fraction of grain boundaries is higher for the films deposited on the sapphire substrate. This feature is well documented by the S and L_+ values.

The Mg films deposited on the well annealed Mg substrate exhibit surprisingly high values of S and low values of L_+ testifying to the high defect density in the film. This may be caused by the presence of the native oxide layer on the surface or by the presence of the layer on the substrate surface containing large amount of defects introduced by pre-sputtering of the substrate. Nevertheless the high defect density in the Mg films deposited on Mg supports our picture that the structure of growing Mg films differs from that of the Mg substrate beneath.

One can see in tab. 5.6 the thicknesses for the Mg2-8 films determined by variation of the film thickness and looking for the minimal χ^2 value. The thicknesses obtained from VEPAS data agree well with the thicknesses determined by the profilometry measurement. Note that for the thin Mg2-4 films the dependence on the film thickness was very weak and the values listed in tab. 5.6 were obtained by step-by-step χ^2 minimization. The problem occurred for the thickness of Mg1 film deposited at RT. The thickness determined by the profilometry and by VEPFIT fitting differ by 1 μm, which is more than 50% deviation. We are actually not sure about the explanation of this phenomenon and it will be the subject of our further studies, but this result may be caused by the higher diffusion length for the particular sapphire and FS substrate used for deposition of these films. The increase of the diffusion length could be caused by annealing of the sapphire and FS substrate for $\sim$ 12 hours at 200°C before the deposition of the Mg1 film. Substrates for the other films were not annealed..

Fig. 5.51 shows a monotonic dependence of the S parameter for the Mg film on the positron diffusion length L_+. One can see in the figure that there is monotonic relationship between S and L_+, the S parameter decreases with increasing L_+ and vice versa. Moreover it can be seen that the values of the S parameter follows a linear dependence on the logarithm of L_+, which is the common feature of VEPAS measurements.

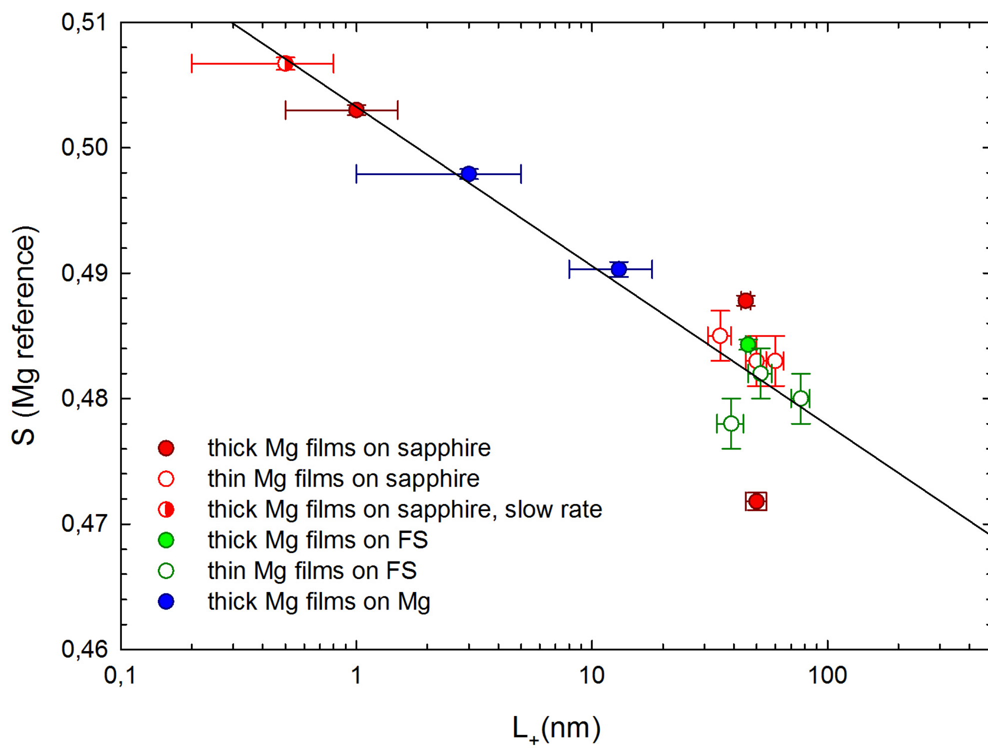

Figure 5.51: Monotonic dependence of the S parameter and the positron diffusion length L_+ for all the Mg film studied.

Conclusions

The main results obtained in this work can be summarized into the following points.

1. A set of Mg films was prepared by RF magnetron sputtering using various thermal treatments, deposition rates, thicknesses and various substrates.

2. The mean grain size increases with the increasing thickness of the film. Crystallites attached directly to the substrate are smaller in size than the next generation growing on the top of the previous generation. A columnar structure reported in the literature was observed.

3. The Mg films deposited at 300°C exhibit always larger grains than Mg films deposited at RT. Subsequent annealing of the films deposited at RT causes slight coarsening of Mg grains.

4. The Mg films deposited on the crystalline sapphire substrate exhibit always smaller grains than the Mg films deposited on amorphous FS substrate and Si and Mg substrates with a thin native oxide layer on their surfaces.

5. All Mg films studied crystallize in a hexagonal close packed lattice, i.e. they have the same structure as bulk Mg.

6. All Mg films studied grew predominantly with the most densely populated Mg(0001) plane parallel with the surface. A strong fiber texture was observed independently on the thermal treatment, the thickness nor the substrate and is caused most likely due to high deposition rate.

7. Subsequent annealing at 300°C for 1 hour of the thick Mg film (1.5 μm) deposited at RT with 20 nm thick Pd over-layer led to formation of Mg-Pd phase. According to our rough simulations the elemental cell of this Mg-Pd phase may be similar to the hcp cell of Mg where one Mg atom is substituted with Pd.

8. Misfit dislocations are present at the interface between the Mg film and the substrate in order to accommodate the misfit stress. The misfit stress is tensile for the films deposited at 300°C and compressive for the films deposited at RT. This is a result of different thermal expansion coefficients of the Mg and the substrates.

9. Positrons implanted into the Mg films are trapped at misfit dislocations at the film-substrate interface and in a vacancy-like open volume defects at grain boundaries.

10. Mg films deposited at 300°C exhibit always lower concentration of defects than the films deposited at RT. Subsequent annealing of the films deposited at RT slightly decreases the defect density.
11. The films deposited on the Mg substrate exhibit higher density of defects that the films deposited under the same conditions on other substrates most likely due to the presence of the native oxide layer on the surface or by the presence of the surface layer containing large amount of defects introduced by pre-sputtering of the Mg substrate.
12. The slow deposition rate at RT causes a significant increase of defect density and decrease of grain size since the interaction between the Mg and the substrate atoms is more pronounced.
13. The Mg-Pd phase may contain structural vacancies leading to a significant enhancement of the defect density.

Bibliography

[1] Sandrock, G. A panoramic overview of hydrogen storage alloys from a gas reaction point of view. *Journal of Alloys and Compounds*, 293-295, (1999), 877. doi:10.1016/S0925-8388(99)00384-9.

[2] Schlapbach, L. and Zuttel, A. Hydrogen-storage materials for mobile applications. *Nature*, 414, (2001), 353–358. doi:10.1038/35104634.

[3] Checchetto, R., Bazzanella, N., Miotello, A., Brusa, R. S., Zecca, A., and Mengucci, A. Deuterium storage in nanocrystalline magnesium thin films. *Journal of Applied Physics*, 95 (4), (2004), 1989–1995. doi:10.1063/1.1637953.

[4] Qu, J., Wang, Y., Xie, L., Zheng, J., Liu, Y., and Li, X. Hydrogen absorption–desorption, optical transmission properties and annealing effect of Mg thin films prepared by magnetron sputtering. *International Journal of Hydrogen Energy*, 34.

[5] Uchida, H. T., Kirchheim, R., and Pundt, A. Influence of hydrogen loading conditions on the blocking effect of nanocrystalline Mg films. *Scripta Materialia*, 64, (2011), 935–937. doi:10.1016/j.scriptamat.2011.01.036.

[6] Richardson, T. J., Farangis, B., Slack, J. L., Nachimuthu, P., Perera, R., Tamura, N., and Rubin, M. X -ray absorption spectroscopy of transition metal–magnesium hydride thin films. *Journal of Alloys and Compounds*.

[7] Gautam, Y. K., Chawla, A. K., Khan, S. A., Agrawal, R. D., and Chandra, R. Hydrogen absorption and optical properties of Pd/Mg thin films prepared by DC magnetron sputtering. *International Journal of Hydrogen Energy*, 37, (2012), 3772–3778. doi:10.1016/j.ijhydene.2011.04.041.

[8] Spatz, P., Aebischer, H. A., Krozer, A., and Schlapbach, L. The difusion of H in Mg and the nucleation and growth of MgH2 in thin-films. *International Journal of Research in Physical Chemistry and Chemical Physics*, 181, (1993), 393–397.

[9] Singh, S., Eijt, S. W. H., Zandbergen, M. W., Legerstee, W. J., and Svetchnikov, V. L. Nanoscale structure and the hydrogenation of Pd-capped magnesium thin films prepared by plasma sputter and pulsed laser deposition. *Journal of Alloys and Compounds*, 441, (2007), 344–351. doi:10.1016/j.jallcom.2006.09.108.

[10] Higuchi, K., Kajioka, H., Toiyama, K., Fujii, H., Orimo, S., and Kikuchi, Y. In situ study of hydriding–dehydriding properties in some Pd/Mg thin films with different degree of Mg crystallization. *Journal of Alloys and Compounds*, 293, (1999), 484–489. doi:10.1016/S0925-8388(99)00470-3.

[11] Higuchi, K., Yamamoto, K., Kajioka, H., Toiyama, K., Honda, M., Orimo, S., and Fujii, H. Remarkable hydrogen storage properties in three-layered Pd/Mg/Pd thin films. *Journal of Alloys and Compounds*, 43, (2002), 2721–2727. doi:10.2320/matertrans.43.2721.

[12] Ye, S. Y., Chan, S. L. I., Ouyang, L. Z., and Zhu, M. Hydrogen storage and structure variation in Mg/Pd multi-layer film.

[13] Léon, A., Knystautas, E. J., Huot, J., Russo, S. L., Koch, C. H., and Schulz, R. Hydrogen sorption properties of vanadium- and palladium-implanted magnesium films. *Journal of Alloys and Compounds*, 356, (2003), 530–535. doi:10.1016/S0925-8388(03)00366-9.

[14] Eijt, S. W. H., Kind, R., Singh, S., Schut, H., Legerstee, W. J., Hendrikx, R. W. A., Svetchnikov, V. L., Westerwaal, R. J., and Dam, B. Positron depth profiling of the structural and electronic structure transformations of hydrogenated Mg-based thin films. *Journal of Applied Physics*, 105, (2009), 043514. doi:10.1063/1.3075762.

[15] Leegwater, H., Schut, H., Egger, W., Baldi, A., Dam, B., and Eijt, S. W. H. Divacancies and the hydrogenation of Mg-Ti films with short range chemical order. *Applied Physics Letters*, 96, (2010), 121902. doi:10.1063/1.3368698.

[16] Eijt, S. W. H., Leegwater, H., Schut, H., Anastasopol, A., Egger, W., Ravelli, L., Hugenschmidt, C., and Dam, B. Layer-resolved study of the Mg to MgH2 transformation in Mg–Ti films with short-range chemical order. *Journal of Alloys and Compounds*, 509S, (2011), S567– S571. doi:10.1016/j.jallcom.2010.09.157.

[17] Checchetto, R., Bazzanella, N., Kale, A., Miotello, A., Mariazzi, S., Brusa, R. S., Mengucci, P., Macchi, C., Somoza, A., Egger, W., and Ravelli, L. Enhanced kinetics of hydride-metal phase transition in magnesium by vacancy clustering. *Physical Review B*, 84, (2011), 054115. doi:10.1103/PhysRevB.84.054115.

[18] Macchi, C., Maurizio, C., Checchetto, R., Mariazzi, S., Ravelli, L., Egger, W., Mengucci, P., Bazzanella, N., Miotello, A., Somoza, A., and Brusa, R. S. Niobium aggregation and vacancylike defect evolution in nanostructured Nb-doped Mg: Their role in the kinetics of the hydride-to-metal phase transformation.

[19] Mattox, D. M. *Handbook of Physical Vapour Deposition (PVD) Processing.* Noyes Publications (1998). ISBN 0-8155-1422-0.

[20] Martin, P. M. *Handbook of Deposition Technologies for Films and Coatings.* Elsevier (2009). ISBN 978-0-8155-2031-3.

[21] Eason, R. *Pulsed Laser Deposition of Thin Films.* Wiley-Interscience (2007). ISBN 978-0-471-44709-2.

[22] Pierson, H. O. *Handbook of Chemical Vapour Deposition (CVD).* Noyes Publications, 2nd edition (1999). ISBN 0-8155-1432-8.

[23] Bordes, J. M., Bordes, C., Ehret, E., Gschwind, R., and Bauer, P. Theoretical sputtering yields of Al and Mg targets in physical vapor deposition processes. *J. Vac. Sci. Technol. A*, 19, (2001), 805. doi:10.1116/1.1365139.

[24] Venugopalan, M. *Reactions under plasma conditions.* Wiley-Interscience (1971). ISBN 978-0-4719-0611-7.

[25] Novotný, M. *Hybrid laser depozition systems, master thesis.* Czech Technical University in Prague, Faculty of Nuclear Sciences and Physical Engineering (2002).

[26] Kendall, H. W. and Deutsch, M. Annihilation of positrons in flight. *Physical Review B*, 101, (1956), 20–26. doi:10.1103/PhysRev.101.20.

[27] Hautojärvi, P. and Vehanen, A. *Positrons in Solids.* Topics in Current Physics 12. Springer Berlin Heidelberg (1979). ISBN 978-3-642-81318-4,978-3-642-81316-0.

[28] Asoka-Kumar, P., Alatalo, M., Ghosh, V. J., Kruseman, A. C., Nielsen, B., and Lynn, K. G. Increased elemental specificity of positron annihilation spectra. *Physical Review Letters*, 77, (1996), 2097. doi:10.1103/PhysRevLett.77.2097.

[29] Asoka-Kumar, P., Lynn, K. G., and Welch, D. O. Characterization of defects in Si and SiO2/Si using positrons. *Journal of Applied Physics*, 76, (1994), 4935. doi:10.1063/1.357207.

[30] Valkealahti, S. and Nieminen, R. M. Monte Carlo calculations of keV electron and positron slowing down in solids. *Applied Physics A*, 32, (1983), 95–106. doi:10.1007/BF00617834.

[31] Vehanen, A., Saarinen, K., Hautojarvi, P., and Huomo, H. Profiling multilayer structures with monoenergetic positrons. *Physical Review B*, 35 (10), (1987), 4606. doi:10.1103/PhysRevB.35.4606.

[32] Reimer, L. *Scanning Electron Microscopy.* Springer (1998). ISBN 978-3-642-08372-3.

[33] *Handbook of Analythical Methods for Materials.* Materials Evaluation and Engineering, Inc. (2010).

[34] Cantafio, C. *Scanning Electron Microscope Usage and Analysis of Metal Fatigue in Mead Silver Paperclips* (1998).

[35] Shipley, R. J. and Stevenson, M. E. Interpreting the evidence: Elemental analysis in the SEM. *Journal of Failure Analysis and Prevention*, 11, (2011), 274–281. doi:10.1007/s11668-011-9451-2.

[36] Als-Nielsen, J. and McMorrow, D. *Elements of Modern X-Ray Physics*. Wiley, 2nd edition (2011). ISBN 978-1-119-99731-3.

[37] Ribárik, G. *Modeling of diffraction patterns based on microstructural properties, PhD. thesis*. Eötvös Loránd University, Institute of Physics, Department of Materials Physics (2008).

[38] Bearden, J. A. X-ray wavelengths. 39 (1). doi:10.1103/RevModPhys.39.78.

[39] Drahokoupil, J. *Interpretation of diffraction profiles, PhD. thesis*. Czech Technical University in Prague, Faculty of Nuclear Sciences and Physical Engineering, Department of solid state engeneering (2011).

[40] Anwand, W., Kissener, H. R., and Brauer, G. A magnetically guided slow positron beam for defect studies. *Acta Physica Polonica A*, 88, (1995), 7.

[41] Anwand, W., Brauer, G., Butterling, M., Kissener, H. R., and Wagner, A. Design and construction of a slow positron beam for solid and surface investigations. *Defects and Diffusion Forum*, 331, (2012), 25. doi:10.4028/www.scientific.net/DDF.331.25.

[42] van Veen, A., Schut, H., Clement, M., de Nijs, J. M. M., Kruseman, A., and Ijpma, M. R. VEPFIT applied to depth profiling problems. *Applied Surface Science*, 85, (1995), 216–224. doi:10.1016/0169-4332(94)00334-3.

[43] Bulíř, J., Novotný, M., Lančok, J., Fekete, L., Drahokoupil, J., and Musil, J. Nucleation of ultrathin silver layer by magnetron sputtering in Ar/N2 plasma. *Surface and Coatings Technology*, 228, (2013), S86–S90. doi:10.1016/j.surfcoat.2012.08.021.

[44] Bulíř, J., Novotný, M., Lynnykova, A., and Lančok, J. Preparation of nanostructured ultrathin silver layer. *Journal of Nanophotonics*, 5, (2011), 051511. doi:10.1117/1.3562568.

[45] Smith, J. F. and Smythe, R. L. Vapor pressure measurements over calcium, magnesium, and their alloys and the thermodynamics of formation of CaMg2. *Acta Metallurgica*, 7, (1959), 261–267. doi:10.1016/0001-6160(59) 90019-7.

[46] Kirchheim, R. Hydrogen solubility and diffusivity in defective and amorphous metals. *Progress in Materials Science*, 32, (1988), 261–325. doi: 10.1016/0079-6425(88)90010-2.

[47] Okamoto, H. Mg-Pd magnesium-palladium. *Journal of Phase Equlibria and Diffusion*, 31 (4), (2010), 407–408. doi:10.1007/s11669-010/9732-6.

[48] `http://www.webelements.com/`. April 11, 2014.

[49] http://www.mt-berlin.com/. April 11, 2014.

[50] http://en.wikipedia.org/. April 11, 2014.

List of Tables

4.1 X-ray wavelengths of Co according to Bearden [38]. 29

5.1 Composition of the Mg magnetron target. 32
5.2 Deposition conditions for Mg films deposition. 32
5.3 Thicknesses, substrates and deposition rates for Mg films. We assume that the thickness measured by profilometry on film on a glass substrate is the same for films deposited on all substrates. From known deposition times the deposition rates were calculated. 35
5.4 Mean grain sizes estimated by SEM. n.a. = not analyzed 37
5.5 Positions 2θ of the Mg-Pd reflections belonging to the Mg-Pd formed in the Mg7 films deposited on FS and sapphire substrates and position 2θ of the reflections belonging to the simulation of modified hcp Mg cell. 52
5.6 Results of the fitting by VEPFIT code for the Mg films, the reference well annealed bulk Mg and the bare FS and sapphire substrates. The S and L_+ for the semi-infinite substrates were fixed during the fitting procedure. The thickness and the positron diffusion length of the Pd layer was fixed at 22 nm and 10 nm respectively. The values of the Mg film thicknesses t_{VEPAS} used in the fitting procedures are included (F = fixed parameter). 72

List of Abbreviations

AC - alternating current
AFM - atomic force microscopy
BSE - back-scattered electrons
CDB - coincidence Doppler broadening DB - Doppler broadening
DC - direct current
fcc - face centered cubic
FS - fused silica
fwhm - full width at half maximum
hcp - hexagonal close packed
HPGe - high purity germanium
HZDR - Helmholtz-Zentrum Dresden-Rossendorf
LT - positron lifetime spectroscopy
n.a. - not analyzed
PAS - positron annihilation spectroscopy
RF - radio frequency
RT - room temperature
SE - secondary electrons
SEM - scanning electron microscopy
SPONSOR - slow positron system of Rossendorf
UHV - ultra high vacuum
VEPAS - variable energy positron annihilation spectroscopy
w.a. - well annealed
XRD - X-ray diffraction